



**Politecnico
di Torino**

Master's Degree in Automotive Engineering

1st December 2023

**Energy optimization based on ADAS
sensors and Connectivity in electric vehicles**

Supervisor:

Angelo Bonfitto

Ali Emadi

Co-Supervisor:

Vittorio Ravello

Atriya Biswas

Candidate:

Fiorillo Carlo

Matricola: 302173

A.Y. 2022/2023

Thesis developed at



In collaboration with



Abstract

The global automotive landscape is evolving rapidly, driven by increasingly stringent regulations aimed at reducing emissions and mitigating the impact of climate change. As a result, Battery Electric Vehicles (BEVs) are gaining prominence considered a cleaner and more efficient mode of transportation. However, several challenges, including limited range, energy consumption, and battery degradation, continue to hinder the widespread adoption of BEVs.

This thesis addresses these challenges by focusing on the development of an optimization strategy based on Model Predictive Control (MPC) for BEVs. The primary objective is to enhance energy efficiency and extend battery life. It accomplishes this by optimizing the vehicle speed profile to minimize energy consumption and reduce battery degradation. To achieve this, multiple simulations employing different approaches has been implemented so that to ensure with the highest probability, real-time implementation capability without compromising performances.

A comprehensive BEV baseline model is developed, incorporating state-of-the-art battery State of Health (SOH) estimation methods, longitudinal vehicle dynamics models, and HVAC model. Notably, the HVAC system serves as the foundation for a parallel developed strategy, known as Integrated Energy and Thermal Management (IETM), which aims to reduce HVAC power demand during peak traction power commands, ensuring cabin comfort without compromising vehicle performance.

The MPC strategy employs a Connected Adaptive Cruise Control (CACC) system capable of optimizing the speed trajectory based on data from a leading vehicle. By predicting the leading vehicle's speed and regulating the distance from preceding vehicle, energy consumption and battery degradation are effectively reduced. Simulations conducted under various driving conditions and noise levels demonstrate the robustness and efficacy of the proposed strategy, resulting in up to 3.7% improvement in energy consumption and 9.7% increase in battery life extent. Furthermore, the implementation of this strategy requires only software updates, making it cost-effective and easily adaptable to existing BEVs. The combination of this MPC-based strategy with the IETM strategy offers the potential for even greater benefits, as both approaches complement each other, optimizing both traction power and auxiliaries loads.

In summary, this research contributes to the advancement of sustainable transportation and addresses critical issues surrounding BEVs. By alleviating range anxiety, reducing energy consumption, and promoting the longevity of battery systems, this strategy lays the foundation for a more sustainable and environmentally conscious future of mobility.

Table of contents

Abstract.....	II
List of Figures.....	V
List of Tables.....	VIII
Nomenclature.....	IX
1. Introduction.....	1
1.1 Emissions and Their Impact: A Catalyst for Change in the Automotive Landscape	1
1.2 Challenges in the Adoption of Battery Electric Vehicles (BEVs).....	6
1.3 Enhancing Vehicle Efficiency: Challenges and Strategies for Battery Electric Vehicles	9
2. BEV Baseline Model	13
3. State of Health model	17
3.1 A brief overview of battery State of Health (SOH) estimation models and the motivation driving their development.....	17
3.2 Equivalent Circuit Battery Model	19
3.3 SOH Estimation Model	21
3.4 Simulation Set-up	23
4. Vehicle speed trajectory optimization strategy	26
4.1 How Autonomous and Connected vehicle technology can improve energy consumption and reduce battery fading in a BEV.....	26
4.1.1 Autonomous vehicle technology.....	26
4.1.2 Connected vehicle technology	28
4.2 Connected Adaptive Cruise Control (CACC).....	29
4.2.1 CACC model implementation	30
4.2.2 Vehicles environment set-up	31
4.3 Leading vehicle data	32
4.4 Constant time gap (CTG) method.....	32
4.4.1 Model description	32
4.4.2 CTG results	34
4.5 Model Predictive Control (MPC)	38
4.5.1 NMPC architecture	38

4.5.2. NMPC Test	51
4.5.3 LMPC architecture	55
4.6.1 Delay in data Communication and Sensor data acquisition	67
4.6.2 Noise in Sensor data acquisition	69
4.7 MPC Results	72
4.7.1 WLTC based simulation Results	72
4.7.2 EPA based simulation Results	74
5. HVAC Model	77
5.1 Auxiliaries effect on battery life and energy consumption	77
5.2 Cabin Model	79
5.2.1 Interaction with external environment.....	79
5.2.2 Solar radiation contribution	81
5.2.3 Conduction – Convection thermal contribution	84
5.2.4 Passenger contribution	86
5.2.5 Cabin Control Volume model	87
5.3 HVAC system model and control.....	90
5.3 Lumped parameter model for cabin temperature evolution	96
6. Integration of Eco-Driving and Thermal Management Strategies for Improved Vehicle Efficiency	98
6.1 CACC and IETM combined Results	98
6.2.1 CACC results	99
6.2.2 Combined results	101
7. Future work	103
8. Conclusion	104
References.....	105

List of Figures

Figure 1: Road transport contribute to CO2 emissions [4]	2
Figure 2: Life Cycle Assessment of an NMC Battery for Application to Electric Light-Duty Commercial Vehicles [6].....	3
Figure 3: WTW CO2 emissions comparison [7]	3
Figure 4: Light Duty EV penetration for each county [10]	4
Figure 5: Annual electric vehicle sales globally by vehicle category (left), technology pathway (middle), and market (right) from 2018 to 2022 [10]	5
Figure 6: Battery characteristics comparison	6
Figure 7: BEV charging point chart [13]	8
Figure 8: LCA impact on CO2 equivalent emissions [14].....	8
Figure 9: BEV architecture.....	14
Figure 10: BEV baseline model.....	15
Figure 11: EPA and WLTC driving cycles.....	16
Figure 12: OCV and Internal Resistance as function of SOC and SOH [15]	18
Figure 13: Cell electric scheme.....	19
Figure 14: Simulink® Battery pack model.....	20
Figure 15: Simulink® battery model	21
Figure 16: Driving cycle reset/charging.....	23
Figure 17: WLTC vehicle speed charging.....	23
Figure 18: WLTC SOC charging	24
Figure 19: WLTC Battery Current charging.....	24
Figure 20: SAE level of driving automation [19].....	26
Figure 21: Following vehicle scheme	33
Figure 22: Simulink® CTG vehicle architecture	34
Figure 23: CTG(WLTC) Speed profile - Distance Error Plots	35
Figure 24: CTG(WLTC) SOC - SOH Plots	35
Figure 25: CTG(WLTC) Acceleration – Traction Power Plots.....	36
Figure 26: CTG(EPA) Speed profile - Distance error Plots	36
Figure 27: CTG(EPA) SOC -SOH Plots	37
Figure 28: CTG(EPA) Acceleration – Traction Power Plots.....	37

Figure 29: NMPC architecture	38
Figure 30: MPC iteration blocks	41
Figure 31: For iteration strategy	42
Figure 32: Prediction model implementation	43
Figure 33: Cost Function Simulink® Block	47
Figure 34: Cost Function Matlab® Script.....	48
Figure 35: Feasibility check	49
Figure 36: Minimum cost acceleration search	50
Figure 37: Longitudinal acceleration and Traction Power Plot NMPC PH = 2, CH = 1	52
Figure 38: Longitudinal Velocity and Vehicle Distance Plot NMPC PH = 2, CH = 1	52
Figure 39: Longitudinal acceleration and Jerk Plot NMPC PH = 10, CH = 1	54
Figure 40: Longitudinal speed and Vehicle distance Plot NMPC PH = 10, CH = 1.....	54
Figure 41: Commanded vs Chassis acceleration WLTC	56
Figure 42 Commanded vs Chassis speed WLTC	56
Figure 43: I/V linearized characteristic.....	57
Figure 44: Cell current comparison	58
Figure 45: Linearized model	58
Figure 46: NMPC simulated model	59
Figure 47: LMPC internal blocks structure	60
Figure 48: Multiple CH block scheme implementation.....	61
Figure 49: WLTC Longitudinal acceleration and Jerk Plots LMPC PH = 10, CH = 2	62
Figure 50: WLTC Longitudinal speed and Vehicle Distance Plots LMPC PH = 10, CH = 2	62
Figure 51: WLTC- [MPC vs CTG] longitudinal acceleration and Traction Power.....	63
Figure 52: WLTC – [MPC vs CTG] SOC and SOH	64
Figure 53: EPA Longitudinal speed Plot LMPC PH = 10, CH = 2.....	65
Figure 54: EPA Longitudinal acceleration Plot LMPC PH = 10, CH = 2	65
Figure 55: Noise and Delay implementation.....	66
Figure 56 WLTC - Delay effect on Relative distance and Speed.....	68
Figure 57: EPA-Delay effect on Relative distance and Speed	69
Figure 58: White Noise signal.....	70
Figure 59: WLTC - Acceleration and Jerk with added NOISE.....	71
Figure 60: Monthly change in specific energy consumption and ambient temperature [29].	78

Figure 61: Sensitivity analysis of battery current in the calculation of specific energy consumption and auxiliary specific energy consumption with varying ambient temperature [29].	78
Figure 62: Cabin C.V. thermodynamic contributions	80
Figure 63: Incident Solar Radiation Contributions	81
Figure 64: Simscape™ - Solar radiation absorbed roof	82
Figure 65: Simscape™ - Solar radiation absorbed glass	83
Figure 66: Simscape™ - Solar radiation transmitted glass	83
Figure 67: Simscape™ - Roof Conduction/Convection.....	84
Figure 68: Simscape™ - Conduction roof metal layer	85
Figure 69: Simscape™ - Conduction/Convection doors	85
Figure 70: Simscape™ - Conduction/Convection glass	85
Figure 71: Simscape™ - Conduction/Convection Floor	86
Figure 72: Simscape™ - Passenger heat contribution	86
Figure 73: Simscape™ complete cabin heat transfer blocks.....	87
Figure 74: Simscape™ mass equilibrium blocks	87
Figure 75: <i>mHVAC</i> boundary conditions.....	88
Figure 76: Free Cabin temperature evolution.....	89
Figure 77: HVAC system architecture	90
Figure 78: HVAC controlled architecture	92
Figure 79: PI controlled cabin temperature evolution with constant reference temperature	94
Figure 80: PI controlled HVAC power request compared to Traction Power with constant reference temperature	94
Figure 81: PI controlled cabin temperature evolution with variable reference temperature	95
Figure 82: PI controlled HVAC power request compared to Traction Power with variable reference temperature	95
Figure 83: Simscape™ model vs. Lumped parameter model free temperature evolution	97
Figure 84: CACC - SOC benefits	99
Figure 85: CACC - SOH benefits	100
Figure 86: CACC+IETM - SOC benefits	101
Figure 87: CACC+IETM – SOH benefits	102

List of Tables

Table 1: BEV specifications	14
Table 2: Pre-exponential factor values	21
Table 3: WLTC/EPA results	32
Table 4: CTG results for WLTC and EPA.....	37
Table 5: WLTC - Architecture Benefits compared to Leading vehicle.....	73
Table 6: WLTC - LMPC vs. NMPC performance reduction	73
Table 7: WLTC - Decrease In performance of LMPC PH = 10, CH = 2 adding Noise.....	73
Table 8: WLTC - Architecture Benefits compared to CTG controlled vehicle	74
Table 9: EPA- Architecture Benefits compared to Leading vehicle.....	74
Table 10: EPA - Architecture Benefits compared to CTG controlled vehicle	75
Table 11: EPA - Decrease in performance of LMPC PH = 10, CH = 2 adding Noise.....	75
Table 12: EPA - LMPC vs. NMPC performance reduction	76

Nomenclature

GHG Greenhouse gas

ICE Internal Combustion Engine

LDV Light duty vehicles

LCA Life cycle assessment

BEV Battery Electric Vehicle

TTW Tank to Wheel

CTG Cradle to Grave

EOL End of Life

EM Electric Motor

IOT Internet of Things

HVAC Heat, Ventilation and Air Conditioning

SOC State of Charge

SOH State of health

OCV Open Circuit Voltage

WLTC World Harmonized Light Vehicles Test Cycle

UDDS Urban Dynamometer Driving Schedule

HWFET Highway Fuel Economy Driving Schedule

BMS Battery Management Strategy

ACC Adaptive Cruise Control

CACC Connected Adaptive Cruise Control

DSRC Direct short-range communication

MPC Model Predictive Control

CTG Constant Time Gap

NMPC Non-Linear Model Predictive Control

LMPC Linear Model Predictive Control

PH Predictive Horizon

CH Controlled Horizon

GSM Golden Search Method

HVAC Heat and Ventilation Air Conditioning

PTC Positive Temperature Coefficient

RDE Real Driving Emission

C.V Control Volume

COP Coefficient of Performance

IETM Integrated Energy and Thermal Management

1. Introduction

1.1 Emissions and Their Impact: A Catalyst for Change in the Automotive Landscape

The global automotive industry is currently experiencing a significant transformation, driven by an increasing embrace of sustainable and eco-friendly transportation solutions. This shift is not merely a matter of choice but rather a necessity imposed by stringent regulations aimed at curbing air pollutant emissions and mitigating the rise in Greenhouse Gas (GHG) concentrations in the Earth's atmosphere. These environmental factors have gained prominence due to a surge in vehicle demand, particularly in nations such as China and India, as documented in [1].

Before delving into the intricacies of prevailing regulations and the challenges they pose to automobile manufacturers, it is crucial to highlight the distinction between GHGs and air pollutants, which underpins the reasons behind these legislative mandates.

The greenhouse gas effect, as elucidated in [2], is a phenomenon wherein certain gases, including CO₂, CH₄, water vapor, NO_x, and others, act as a thermal blanket around the Earth. They absorb heat energy emitted by the Earth's surface, preventing it from dissipating into space. This natural mechanism maintains the Earth's temperature at a level conducive to supporting human life. However, human activities such as the combustion of fossil fuels (coal, oil, and natural gas), deforestation, and industrial processes have substantially increased the concentration of these greenhouse gases in the atmosphere, contributing to the phenomenon known as global warming.

In contrast, pollutants encompass solid, liquid, or gaseous substances in the air that have detrimental effects on the environment and human health. These pollutants can be categorized into *primary pollutants*, emitted directly as a result of human activity or natural processes, and *secondary pollutants*, which are formed through complex reactions involving primary pollutants, sunlight, and atmospheric components [3]. Among the most significant pollutants resulting from incomplete or suboptimal combustion processes, especially in Internal Combustion Engines, are CO, HC, NO_x, PM.

As outlined in [3], the transportation sector (including exhaust emissions, brake and tire wear, road abrasion, and fuel evaporation) stands as a major contributor to Nitrogen oxides (NO_x) and hydrocarbons (HC) emissions, while carbon monoxide (CO) and particulate matter (PM)

primarily emanate from building-related activities such as cooking, heating, and lighting. In the context of GHGs, as depicted in Figure 1, the transport sector accounts for 23% of global anthropogenic emissions. Further scrutiny reveals that road transport constitutes a significant portion, representing 73.9% of the total CO₂ emissions attributed to the transportation sector. Among these, light-duty vehicles, which include low-weight vehicles designed for the transportation of passengers and light payloads, make up a substantial portion, accounting for 53.5%. Therefore, addressing emissions from these vehicles has the potential to yield substantial environmental benefits.

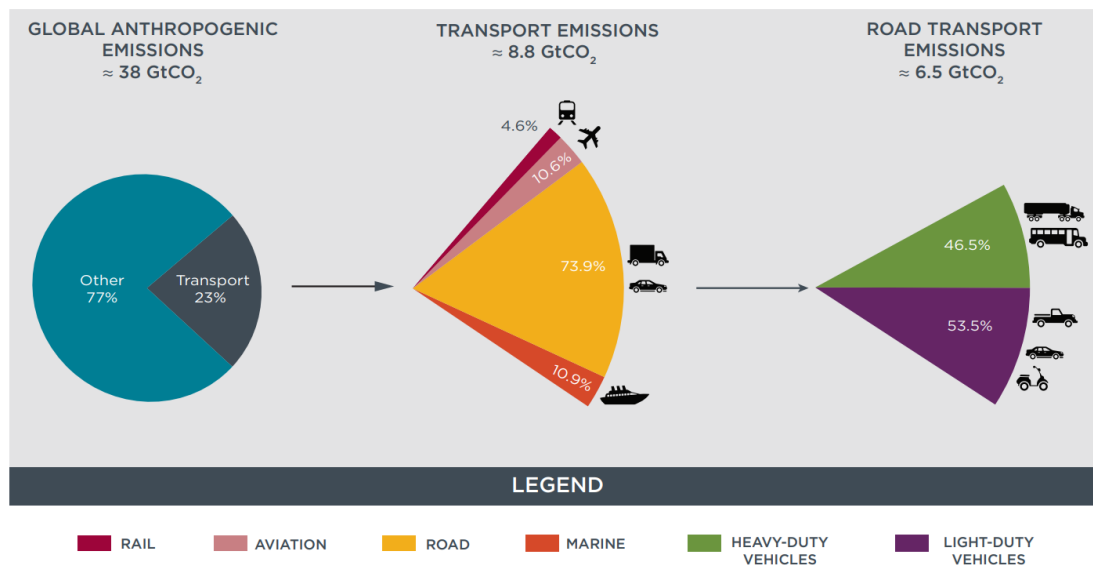


Figure 1: Road transport contribute to CO₂ emissions [4]

To address the issues outlined earlier, governments worldwide are implementing stringent regulations targeting both CO₂ emissions and pollutant emissions, exemplified by the European EURO 6 standards. These regulations establish comprehensive guidelines, ranging from vehicle homologation procedures to emission limits for various types of propulsion systems. Notably, while EURO 6 focuses on emissions generated during the vehicle's operation (commonly referred to as "Tank-to-Wheel" or TTW emissions), there are currently no restrictions on the production cycle of vehicles.

However, there is a growing trend toward more rigorous environmental considerations throughout the vehicle development and production process. This shift is characterized by an increasing emphasis on Life Cycle Assessment (LCA), a systematic methodology used to evaluate the environmental impact of a product, process, or activity throughout its entire life cycle, from raw material extraction to production, use, and disposal. In the context of the automotive industry, LCA assesses various environmental aspects, as illustrated in Figure 2,

which provides an overview of the environmental footprint of a Battery Electric Vehicle (BEV) light-duty commercial vehicle.

Figure 2 clearly demonstrates that global warming, a critical factor addressed by the current

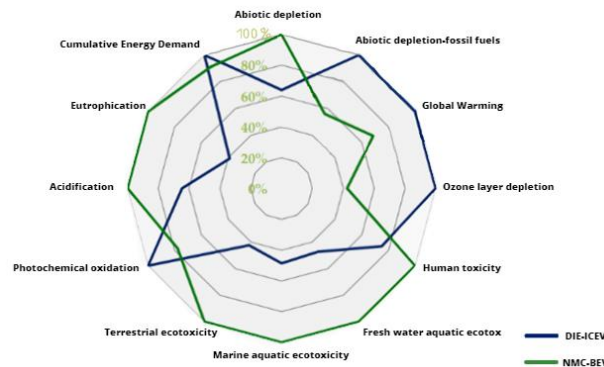


Figure 2: Life Cycle Assessment of an NMC Battery for Application to Electric Light-Duty Commercial Vehicles [6]

EURO 6 regulations, is significantly mitigated by BEVs when compared to Internal Combustion Engine (ICE) vehicles. It's important to note that EURO 6, as it stands, primarily considers TTW CO₂ emissions, focusing on emissions produced during a vehicle's operation, such as tailpipe emissions. This emphasis on TTW emissions has driven the choice of propulsion system, particularly for passenger vehicles, toward Battery Electric Vehicles (BEVs). Those are increasingly recognized as one of the most promising alternatives to conventional ICE vehicles due to their zero tailpipe emissions and enhanced energy efficiency.

Conventional mid-size car		
WTT	TTW	Total (WTW) CO ₂ emission
30	130	160
Battery electric vehicle		
Electricity mix		Total (WTW) CO ₂ emission
Italian mix 2010: 11% nuclear, 23% renewable, 66% fossils		72
EU-27 mix 2010: 27% nuclear, 23% renewable, 50% fossils		58
French mix 2010: 74% nuclear, 21% renewable, 5% fossils		22

Figure 3: WTW CO₂ emissions comparison [7]

Examining Figure 3, it becomes evident that conventional Internal Combustion Engine (ICE) vehicles exhibit a significantly higher total Well-to-Wheel (WTW) CO₂ emissions compared to Battery Electric Vehicles (BEVs). This difference holds true even when considering various countries, each with its distinct electricity generation sources. It's worth noting that in some instances, the Well-to-Tank (WTT) emissions, which pertain to the production and

transportation of the energy source up to the distribution point, are notably higher for BEVs. This, however, is counterbalanced by substantially higher Tank-to-Wheel (TTW) emissions for conventional vehicles.

As illustrated in Figure 4, a closer examination of the current landscape reveals a remarkable surge in the market penetration of Battery Electric Vehicles (BEVs), particularly over the last three years. This surge is primarily attributed to trends observed in China and Germany, exemplifying a global shift towards more environmentally friendly and sustainable transportation solutions. This technology is well-positioned for significant market expansion, with projections pointing towards a substantial increase in BEV adoption by 2040. These forecasts are bolstered by considerable investments, including the allocation of 150 billion funds through Sustainable Recovery Plans aimed at promoting efficient cars and electric vehicles (EVs), as reported in [5].

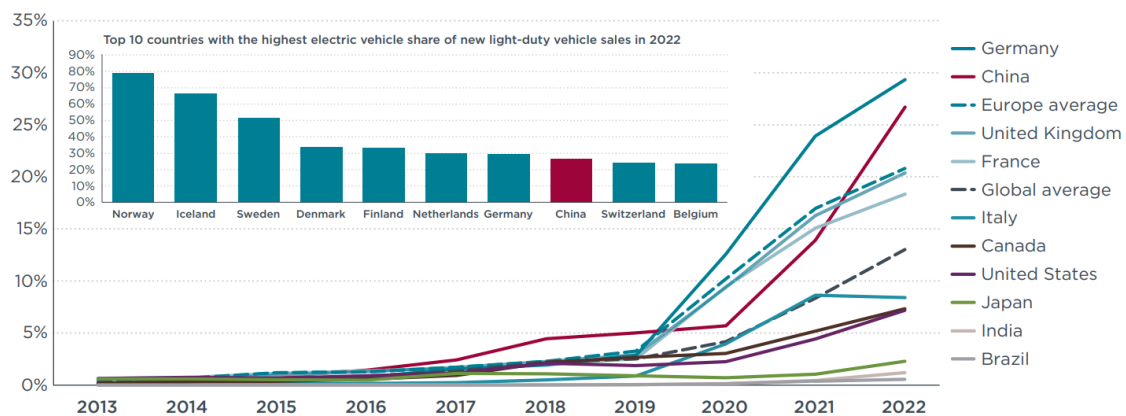


Figure 4: Light Duty EV penetration for each county [10]

Figure 5 further underscores this transformation by highlighting that for Light Duty Vehicles (LDVs) since 2018, annual sales have increased, exceeding five times their previous figures. This surge signifies a clear preference for Battery Electric Vehicles (BEVs) over other alternatives, such as plug-in vehicles or fuel cell-based vehicles, within the automotive market. Notably, the global BEV market is prominently led by China, which accounts for more than half of all BEVs sold worldwide. China's proactive approach in promoting and adopting BEVs aligns with the global trend towards sustainable and environmentally friendly transportation solutions.

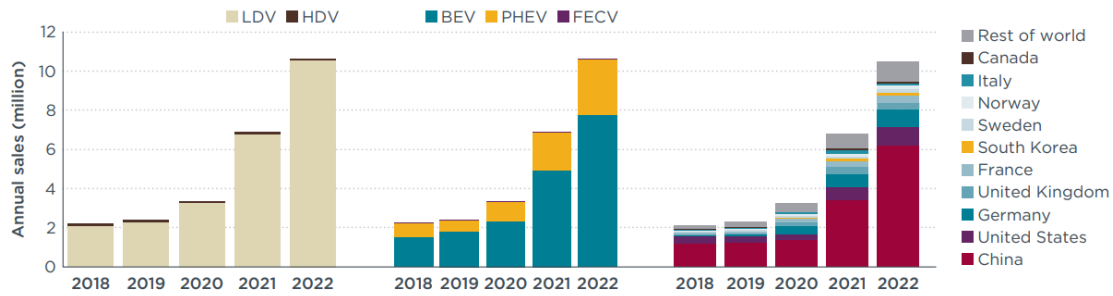


Figure 5: Annual electric vehicle sales globally by vehicle category (left), technology pathway (middle), and market (right) from 2018 to 2022 [10]

It is worth noting that, while EURO 6 represents a significant step toward addressing emissions concerns, future regulations, such as EURO 7, are expected to impose even more stringent constraints. As delineated in [8], EURO 7 norms are expected to come into effect in July 2025 for new light-duty vehicles and on July 1, 2027, for new heavy-duty vehicles. Notably, EURO 7 rules are described as technology- and fuel-neutral, applying the same emission limits across all vehicle categories regardless of their technology (e.g., conventional internal combustion engines, hybrids, or plug-ins) or the type of fuel used (gasoline, diesel, or others). These limits also extend to zero CO₂ emission vehicles, including electric and fuel cell vehicles. The EURO 7 proposal introduces several changes, encompassing updated limits for pollutant emissions, expanded boundary conditions for Real Driving Emissions (RDE) testing, prolonged emission durability periods, and the introduction of the first-ever limits for particulate emissions, with measurements lowered from 23 nm to 10 nm for brake emissions. Additionally, it includes regulations on microplastic emissions from tires, affecting not only vehicles with internal combustion engines but also Battery Electric Vehicles (BEVs).

Furthermore, the new regulation places increased emphasis on Life Cycle Assessment (LCA) for CO₂ emissions. The idea is to consider emissions throughout a vehicle's entire lifecycle, moving beyond Tank-to-Wheel (TTW) emissions and encompassing Cradle-to-Grave (CTG) emissions. This approach entails evaluating the CO₂ impact of a product from raw material acquisition through the manufacturing process, distribution, use, and end of life (EoL) treatments. This shift in regulations underscores the growing importance of comprehensive sustainability assessments in the automotive industry, prompting a reconsideration of what was once the obvious choice under the current regulations, namely BEVs.

According to the European Parliament and the Council [9], the regulation establishes targets for battery waste collection for light means of transport, mandating 51% by the end of 2028 and 61% by the end of 2031. It also sets a target for lithium recovery from waste batteries of 50% by the end of 2027 and 80% by the end of 2031. Furthermore, the regulation prescribes

mandatory minimum levels of recycled content for industrial EV batteries. It introduces labelling and information requirements, including details on the battery's components and recycled content, as well as an electronic "battery passport" and a QR code. To provide sufficient preparation time, labelling requirements will apply by 2026, and the QR code by 2027.

As a result of this regulation, the choice of future technology as the dominant one becomes uncertain. Automakers are grappling with the challenges posed by these rapidly evolving regulations, which necessitate adjustments not only in production but also in the future market landscape.

1.2 Challenges in the Adoption of Battery Electric Vehicles (BEVs)

Taking into account the previous paragraph, several challenges still exist for BEV technology. The most significant ones are outlined below:

1. **Range:** This remains one of the most significant issues for these vehicles. The current

technology limits battery energy storage, with Specific Energy values around $128 \frac{Wh}{kg}$ and Volumetric Energy Density around $230 \frac{Wh}{l}$ for lithium-ion batteries, the most prevalent solution on the market due to their high charging efficiency, high specific energy and high energy density [12]. These values indicate the energy a battery can store relative to its

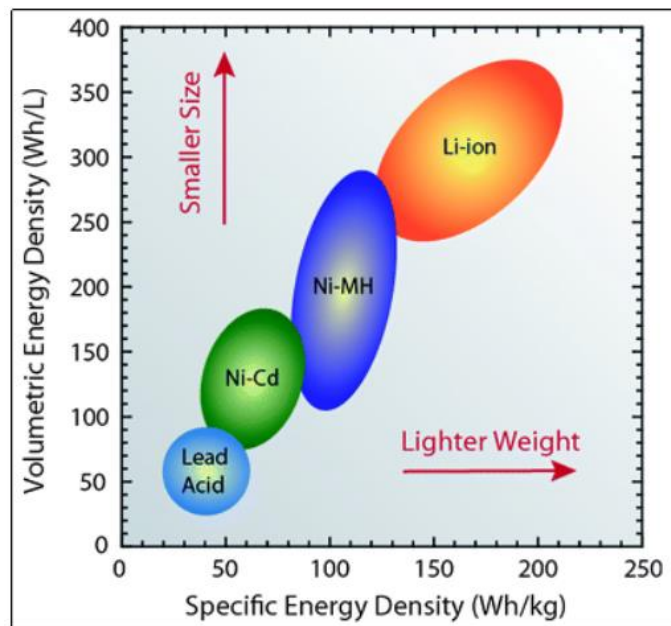


Figure 6: Battery characteristics comparison

weight and size. The larger these values, the smaller and lighter the battery. However, these values are still far from the properties of ICE fuels, trailing by approximately two orders of magnitude. Consequently, it remains challenging for automakers to compete with traditional vehicles.

2. Production Costs: Presently, due to factors such as insufficient infrastructure and the high cost and limited availability of raw materials, especially in Europe, the production costs of BEVs exceed those of conventional ICE-based vehicles. As noted in [11], this price gap is expected to narrow with technological advancements and improvements in production processes. Additionally, increases in battery capacity and electric range for BEVs in the coming years will mitigate the impact of reductions in cost per kWh on the overall additional costs associated with these powertrains.
3. Infrastructure: The charging time for Battery Electric Vehicles (BEVs) remains a pivotal concern in the adoption of electric mobility, presenting a complex trade-off between convenience and battery health.

On one hand, fast charging can significantly reduce the time required to charge a BEV, making it more practical for daily use. However, rapid charging at high current is detrimental to the battery accelerating its degradation over time, thus shortening the battery's lifespan.

On the other hand, slow or standard charging methods are gentler on the batteries extending the battery's life expectancy. However, these charging modes necessitate longer charging durations, which can be less convenient for users accustomed to very short charging time, especially during long journeys or for those without access to overnight charging at home.

Furthermore, the production of electricity for charging stations is another aspect that warrants consideration. As the sales of BEVs have surged, the demand for electricity to power these vehicles has also grown substantially. The need for substantial infrastructure investments and upgrades to electricity grids to support the higher demand for charging stations is a logistical challenge. It's essential to ensure that the electrical grid can handle the load while also minimizing the environmental impact.

Regarding charging infrastructure, the study presented in paper [13] sheds light on the relationship between the number of charging points and the number of BEVs in commerce. In 2015, the Netherlands stood out as the only country with a surplus of charging points compared to the number of BEVs in commerce. However, as highlighted above, the sales of BEVs have surged significantly in recent years. This increase in BEV adoption has led to a rapid decrease in the ratio of charging infrastructure to vehicles across various countries.

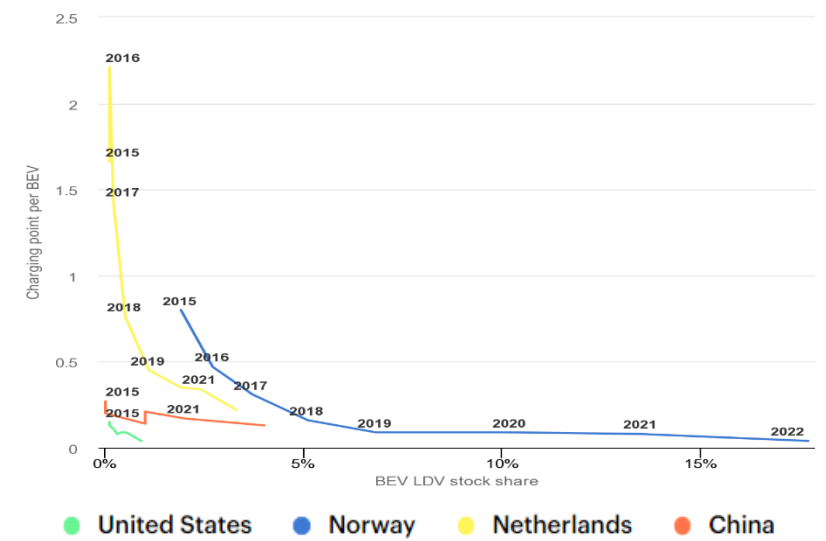


Figure 7: BEV charging point chart [13]

4. Battery life and recycling: In accordance with the European regulations scheduled to come into effect in 2025 for Light-Duty Vehicles (LDV) [8], the longevity of batteries will become a critical aspect to monitor. The new Battery Electric Vehicles (BEVs) will be expected to achieve a minimum mileage of 200,000 kilometres, setting a high standard for endurance. Furthermore, the recycling phase is a complex and sensitive topic. To comply with cradle-to-grave carbon footprint requirements, End-of-Life (EOL) treatments must be considered to reduce carbon dioxide (CO₂) equivalents, as depicted in the figure below:

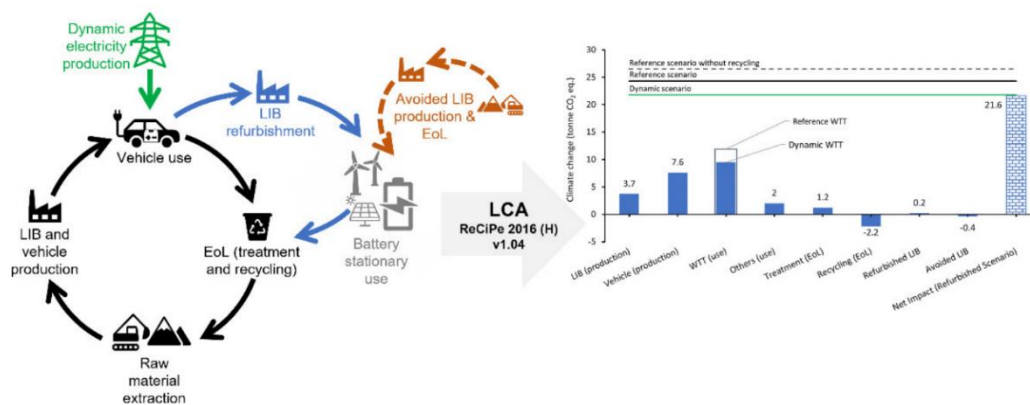


Figure 8: LCA impact on CO₂ equivalent emissions [14]

As outlined in the study [14], reusing batteries in different sectors to give them a second life before recycling can offer significant benefits. However, when utilizing Pyrometallurgical processes, as elucidated in [8], certain battery components can be

recovered, but others like lithium (Li) and manganese (Mn) are not efficiently reclaimed, and the recovery process can be energy intensive. Consequently, new technologies, such as Hydrometallurgical methods with high recovery rates and low energy consumption, are being explored. These approaches also face current challenges in minimizing wastewater generation and optimizing the overall process, further complicating their implementation.

1.3 Enhancing Vehicle Efficiency: Challenges and Strategies for Battery Electric Vehicles

These challenges underscore the complexity of the transition to sustainable mobility and the need for continued innovation and adaptation in the automotive industry. With a deeper understanding of why governments are strongly advocating for Battery Electric Vehicles (BEVs) and the primary challenges facing this technology, it becomes evident that significant improvements in vehicle performance, consumption, and battery life are necessary without significantly impacting the vehicle price. Within vehicles, the most substantial factors contributing to energy consumption include:

- Aerodynamics
- Tires Rolling Resistance
- Inertia
- Efficiency and Friction

In the case of BEVs, losses due to transmission and engine inefficiency are almost negligible. Typically, BEVs have a single transmission ratio between the wheels and the Electric Motor (EM), with EMs exhibiting high efficiency, often approaching 90% (more than double the one of ICE). Consequently, the contributions of transmission and engine inefficiencies can be disregarded for BEVs.

Considering BEVs, the sectors where engineers can make a substantial physical impact are Aerodynamics, Tire Rolling Resistance, and Weight Reduction. According to [8], a 10% reduction in each of these areas can yield significant improvements:

- Tire Rolling Resistance \rightarrow -1.5% Fuel consumption
- Aerodynamics ($C_x \cdot \text{Frontal Area}$) \rightarrow -2.7% Fuel consumption
- Weight Reduction \rightarrow -3.5% in Fuel consumption

While each of these areas can offer notable improvements, achieving 10% improvements presents challenges and may lead to costly development endeavours.

One potential solution includes powertrain-level enhancements through different levels of hybridization or more complex solutions, as well as vehicle body modifications aimed at reducing resistance forces or weight. However, all of these approaches entail significant time and cost, rendering them impractical for many passenger vehicles available in the market. Alternatively, engineers can focus on developing optimization strategies at the software level, leveraging existing vehicle sensors to minimize energy consumption and enhance battery life without significantly increasing vehicle complexity or cost. This approach aligns with the current trend of the Internet of Things (IoT) and can be further enhanced by utilizing communication between vehicles and infrastructure, allowing for rapid responses to unforeseen conditions and predictive actions to reduce energy consumption while extending battery life.

This study, instead, directs its focus towards optimal powertrain control in autonomous and connected environments. The overarching objective is to optimize future vehicle speed profiles with the dual purpose of minimizing energy consumption and extending battery life. This strategic choice aligns with the prevailing automotive trend, which emphasizes Autonomous and Connected vehicle technologies, specifically targeting enhanced energy efficiency and prolonged battery life [39,40,41,42,43].

Various strategies within the current scientific literature share analogous objectives but employ distinct implementation architectures compared to our research. These methods span from the rudimentary Constant Time Gap Adaptive Cruise Control architecture [44] to the utilization of manual Human-Machine Interface (HMI) [22], noted for its simplicity and cost-effectiveness. An alternative approach, converging on similar objectives yet adopting a divergent implementation and embracing a more intricate architecture, involves dynamic programming (DP). While DP is adept at discovering a global optimal solution, it lacks the capability for online applications. Recognizing the inherent limitations of DP, research has explored solutions such as extracting a set of rules for real-time implementation [45]. Similarly, Reinforcement Learning is presented as a valid alternative for that, achieving near-optimal results analogous to dynamic programming. Nevertheless, it contends with the intrinsic drawback of a substantial amount of data imperative for effective training [38]. An alternative solution, Data-Driven Predictive Control, obviates the necessity for intricate mathematical models by leveraging historical data to inform control decisions [37]. While similar to Reinforcement Learning in its adaptability to non-linear and intricate systems, it necessitates a significant volume of data for accurate predictions.

Transitioning toward methodologies more aligned with our research goals, adaptive cruise control systems for connected energy-saving electric vehicles are elucidated. These systems leverage connectivity and automation through a non-linear Model Predictive Control (MPC) framework, encompassing design considerations for stochastic communication delays [36,46]. Techniques oriented towards minimizing energy consumption, with a concurrent focus on battery degradation, are explored in an economic adaptive cruise controller (EACC). Founded on a Non-Linear model that accommodates battery aging characteristics based on adaptive model predictive control (AMPC) [47].

Expanding upon the established foundations in prior research, this paper identifies a critical research gap and endeavours to introduce an innovative solution. The approach adopted in this study capitalizes on the strengths of existing strategies while conscientiously addressing their limitations and criticalities. Accordingly, this paper introduces an Optimal Adaptive Cruise Control (OACC) system designed to bridge this identified gap.

The proposed system employs a Linear Model Predictive Control approach, which optimally determines the vehicle's speed profile for the short-term future through a multi objective cost function. The primary objectives are to enhance energy efficiency, reduce battery degradation, and maintain safe inter-vehicle distances simultaneously. This innovation serves to decrease computational costs compared to Nonlinear Model Predictive Control, eliminates the need for extensive training data typically required in reinforcement learning, and reduces the data dependency associated with data-based predictive control.

Furthermore, the implemented architecture is equipped to leverage information from sensors embedded in vehicles with an Automation level greater or equal than 1. This distinctive feature ensures the system functions seamlessly in a mixed environment without compromising performance, a characteristic observed in prior literature [37]. It can seamlessly adapt to sensor data or connected information.

In a notable departure from existing research, this work not only presents a new strategy that evaluates its impact solely on energy consumption, but also tests its influence on battery health. A dedicated battery state of health estimation model which influence battery energy storage will be employed to evaluate the system's influence on battery condition.

The model's robustness will be further validated through simulations conducted across various driving scenarios, including urban and extra-urban highways. These simulations will also factor in external disturbances such as noise and delay, closely replicating real-world conditions stemming from sensor acquisition and communication. Moreover, an estimation model for battery state of health is proposed to illustrate the benefits of the implemented strategy on

battery life. In addition to the research presented in this thesis, the broader project includes a strategy for minimizing peak power demand associated with Heat Ventilation (HVAC) and Air Conditioning while maintaining cabin comfort and reducing battery degradation. A comprehensive thermal model for the cabin and HVAC system was developed to simulate real-time temperature changes.

The following sections will delve into the details of the developed models and present the outcomes of the combined strategies. These sections will highlight their benefits and performance improvements across various scenarios, reinforcing the novel contributions identified in support of this thesis.

2. BEV Baseline Model

Before delving into the detailed description of the models developed in this project, let's begin with a brief overview of the baseline Battery Electric Vehicle (BEV) model provided by the McMaster Automotive Resource Centre (MARC). The baseline model used for this project represents a 2015 Chevy Spark city car powered by a battery. Key vehicle specifications are summarized in Table 1.

Electric Motor	
Torque _{max}	444 N·m
ω_{base}	1910 rpm
ω_{max}	5503 rpm

Battery	
Cell rated capacity	2.5 A·h
N° cells in parallel	22
N° cells in series	121
Columb efficiency	0.99
OCV ¹	400 V
Battery internal Resistance ¹	55 mΩ

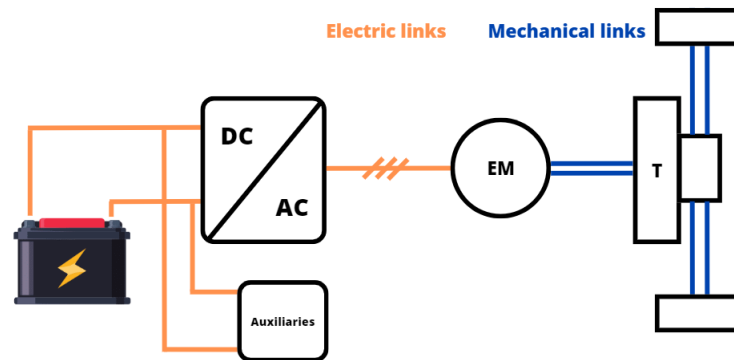
Vehicle data	
Mass	1300 kg
C _x	0.326 m
Wheelbase	2.375 m
Weight distribution	50/50
Single gear efficiency	0.95
Frontal Area	1.77 m ²
Rolling resistance coefficient μ_1	0.006
Rolling resistance coefficient μ_2	0.0001 s/m

¹ The following data varies according to the SOH of the battery; the one in the table are value referring to 100% SOH and 95% SOC

Wheel Radius	0.277 m
Final Drive ratio	3.87
Mot inertia	0.02 kg·m ²
Final drive inertia	0.1 kg·m ²
One wheel inertia	1 kg·m ²
Electric auxiliary power	200 W

Table 1: BEV specifications

The baseline model, constructed in Simulink® environment, represents a simplified Electric Vehicle (EV) architecture with a single battery providing power for traction and auxiliaries, one single Electric Motor (EM), one inverter and a single gear ratio transmission at wheel level. This architecture is illustrated in Figure 9.

**Figure 9:** BEV architecture

This model is of the forward type describing only the longitudinal vehicle dynamic, meaning it translates driver input into vehicle behaviour at the wheel level. The driver, in this context, receives a driving cycle speed profile as input and adjusts the requested torque to the EM accordingly. This process accounts for efficiency considerations and feasibility checks before transmitting the request to the wheels, propelling the vehicle. The battery model embedded in this setup allows monitoring of current requirements and estimation of the state of charge (SOC) for the vehicle at each time-step (with a simulation time-step of 0.1 seconds).

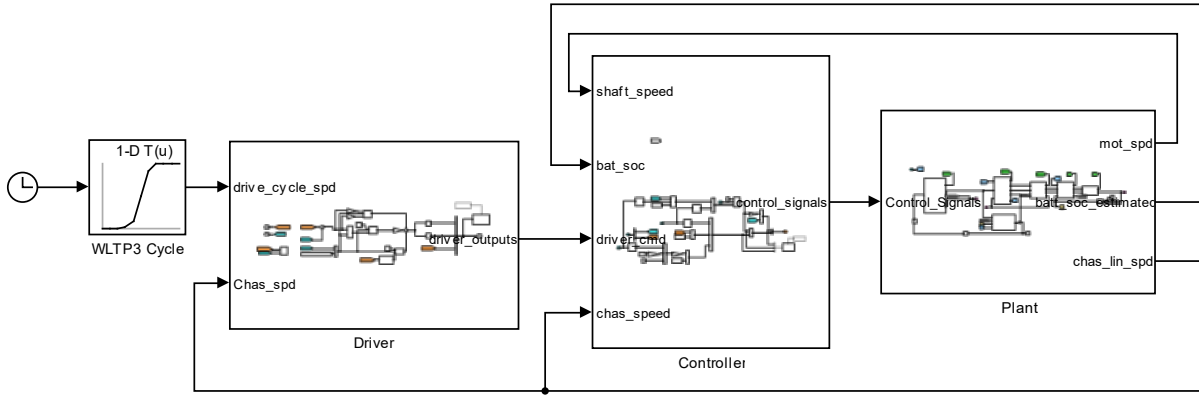


Figure 10: BEV baseline model

Figure 10 illustrates the BEV baseline model, where a specific driving cycle is provided as the primary input. In this thesis, two distinct driving cycles are employed to represent realistic scenarios: the Worldwide Harmonized Light Vehicles Test Cycle (WLTC), used in Europe, and the EPA cycle, utilized in the United States. [8]:

- **WLTC:** This cycle spans 25.25 km and is the current European standard for test procedures. It covers a range of driving scenarios, including urban, highway, and extra-urban conditions, featuring high average speeds, short stop durations, and intense acceleration, making it a closer approximation of real-world driving.
- **EPA:** This cycle combines two sub-cycles: the Urban Dynamometer Driving Schedule (UDDS), simulating city driving conditions for Light-Duty Vehicles (LDVs) testing, and the Highway Fuel Economy Test (HWFET), assessing fuel economy at highway speeds, with speeds approaching 100 km/h. The EPA cycle is less aggressive compared to WLTC. Considering the amount of SOC and SOH decrease for km driven, it is respectively 6.7% and 20.4% more for WLTC with respect to EPA. Anyway, it is currently employed in the United States and covers a longer distance of 28.5 km. consequently has been used as a further check on controller flexibility and adaptability.

These two cycles aim to encompass diverse driving scenarios, ensuring comprehensive testing and evaluation of the BEV model. Moving forward, the model incorporates the driver and controller blocks. The driver block receives the vehicle speed input and employs a Proportional-Integral (PI) controller to generate commands for driving and braking torque, based on the speed error between the actual chassis speed and the imposed driving cycle. These commands are then passed to the controller block, which, considering the EM characteristic curves (such as Torque/shaft speed), friction limits, and maximum regenerative braking, determines the feasible braking or driving torque. Within the plant, the commanded torque is translated into

current requests to the battery, accounting for battery capacity decrease over time. Simultaneously, the torque is transmitted through the final drive to the wheels, and converted into chassis speed. This information is then fed back into the driver to initiate the process once more.

This brief introduction provides an overview of the baseline model used as the foundation for this project. In subsequent sections, we will delve into the details of the developed models, explaining the implementation process and presenting the obtained results.

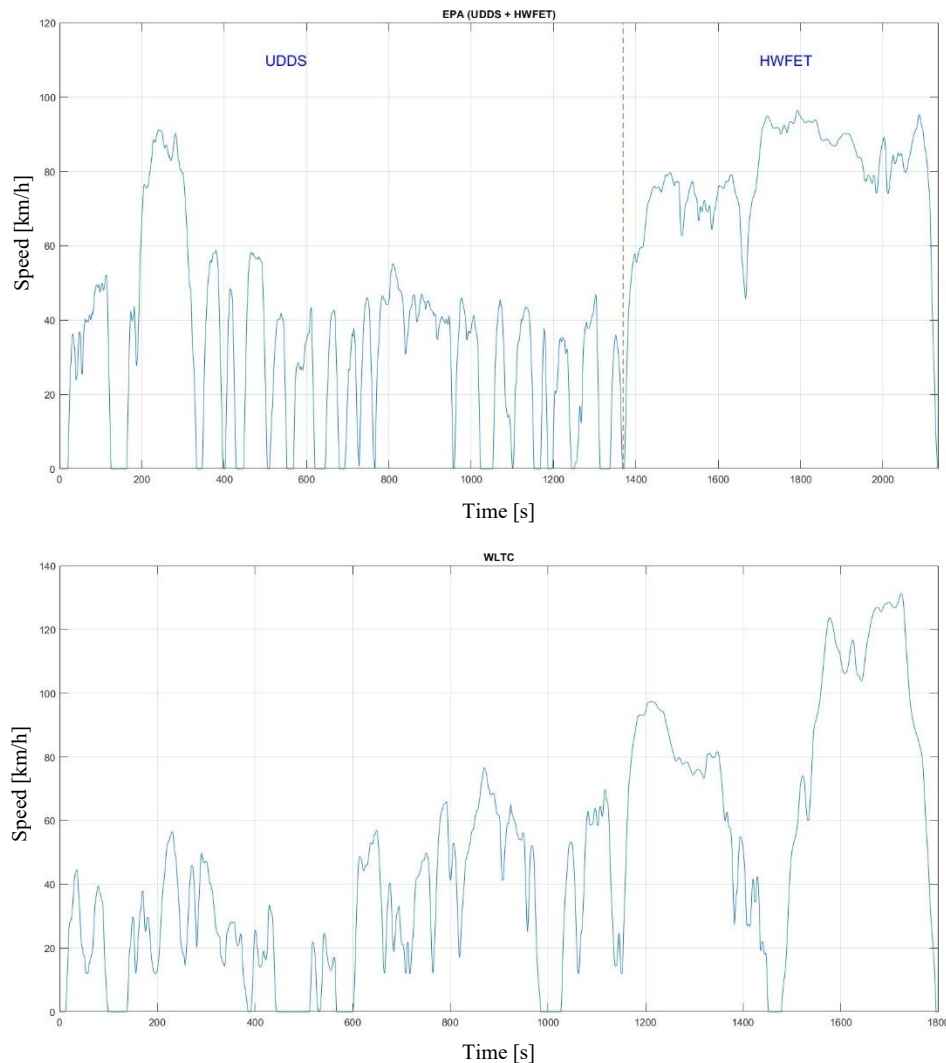


Figure 11: EPA and WLTC driving cycles

3. State of Health model

3.1 A brief overview of battery State of Health (SOH) estimation models and the motivation driving their development

Ensuring the longevity and reliable performance of batteries for automotive applications is fundamental, aligning with the regulatory guidelines in Europe. Working on peak current demands and optimizing secondary components, such as auxiliary systems is a way to maximise the battery extent, enhancing not only safety but also contributing to maintaining consistent vehicle performance for an extended period.

As elaborated in [16], the State of Charge (SOC) represents a critical parameter, offering a real-time snapshot of a battery's energy storage capacity as a percentage relative to its last full charge. The formula for SOC is as follows:

$$SOC = \frac{C_{actual}}{C_{max actual}} \cdot 100 \quad (I)$$

However, relying solely on SOC does not provide a precise estimate of the remaining time until complete battery discharge without considering the battery's history. This is where State of Health (SOH) comes into play, offering insights into a battery's dynamic status relative to its initial condition, typically designated as $SOH = 100\%$ at the time of manufacture. Over time and with usage, SOH gradually diminishes due to irreversible chemical and physical processes, collectively referred to as battery aging. When the battery's ability to store and deliver energy falls below a predefined threshold, it is considered depleted, although it may still be used for less demanding applications, necessitating eventual replacement. SOH considers various parameters, including internal resistance, open-circuit voltage (OCV) variation, and actual maximum capacity degradation. The most common approach gauges battery health by evaluating its maximum capacity, denoted as $C_{max actual}$ in the SOH formula, which represents the current battery capacity when the SOC is at its maximum level. The denominator of the SOH formula represents the capacity of the battery when it was new and at maximum SOC level, denoted as $C_{max initial}$. The SOH formula, consequently, is given by:

$$SOH = \frac{C_{max actual}}{C_{max initial}} \cdot 100 \quad (II)$$

The significance of monitoring SOH lies in determining the battery's End of Life (EoL). Typically, a battery is considered to have reached EoL when its actual maximum capacity reaches 80% of its initial capacity [18]. This decline in capacity adversely impacts various performance aspects, including range, power output, and operational temperature. Consequently, the battery necessitates replacement.

As outlined in [15], as the battery undergoes degradation, its attainable maximum capacity progressively diminishes. Looking at equation (I) in fact, reducing the denominator multiplying the capacity for the SOH factor, it is possible to reach 100% SOC with a smaller battery actual capacity, indicating that the total amount of energy that the battery can store has been reduced. This, in turn, translates into a diminished range for the battery's operation. Furthermore, the Open Circuit Voltage (OCV) declines and internal resistance increases due to the natural wear and aging of internal components (SOH decrease), as shown in the following figures where experimental data from battery fading test illustrated in [15] are considered. Consequently, the greater demand for current leads also to increased thermal losses.

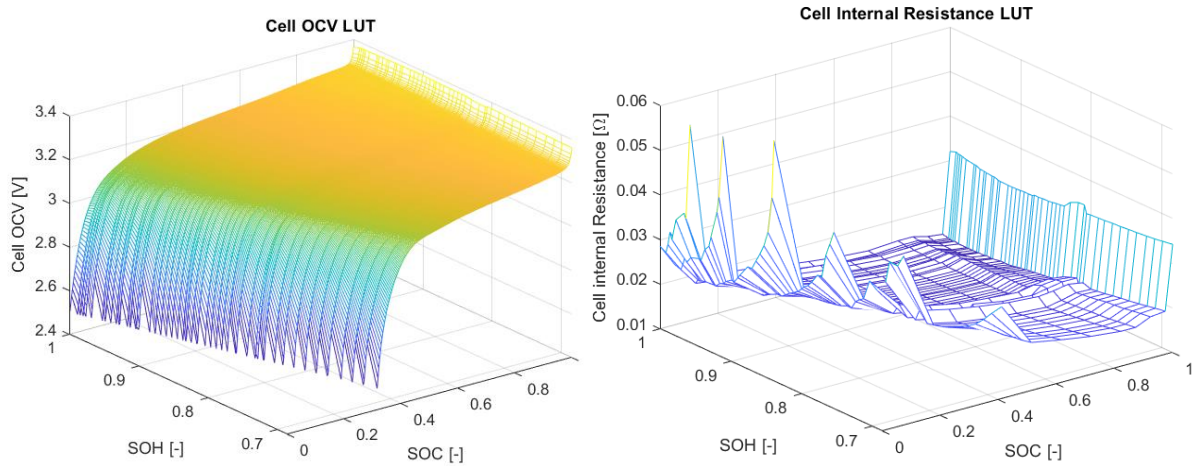


Figure 12: OCV and Internal Resistance as function of SOC and SOH [15]

To counteract these rising operating temperatures, the adoption of power reduction or an intensified Battery Management System (BMS) proves indispensable. These systems, as elaborated in [16], enable the battery to operate within the confines of the safe operating area (SOA), preventing the occurrence of overcharging or over discharging by continually monitoring key battery parameters.

Since directly measuring the State of Health (SOH) of a battery is not feasible [18], it's necessary to employ a method that estimates these states based on measurable variables.

Among the current strategies for assessing battery health, five primary models have been identified based on existing research [16]:

1. Algorithms based on electrochemical principles.
2. Algorithms utilizing equivalent circuit models.
3. Performance-based models.
4. Analytical methods incorporating empirical fitting.
5. Statistical Methods.

For this project, the chosen model falls under the category of analytical methods with empirical fitting. This approach involves using a mathematical model exploiting the Arrhenius relation and a coulomb counting method to estimate the current SOH of the battery. Experiments conducted by [15] were utilized to include characteristics such as Open Circuit Voltage (OCV) and internal resistance. The model's parameters were then fine-tuned to align with the experimental results, consequently the method falls under that category. Further detailed insights into this model will be provided in subsequent sections, where its comprehensive analysis will be presented.

3.2 Equivalent Circuit Battery Model

To ensure reliable and consistent result, a model based on paper [15] data has been implemented in the previously presented BEV architecture. This model simplifies the battery as a series and parallel connection of elementary cells, depicted in figure 13. This representation includes a voltage generator representing the cell's Open Circuit Voltage (OCV) in series with a resistance representing the cell's internal resistance.

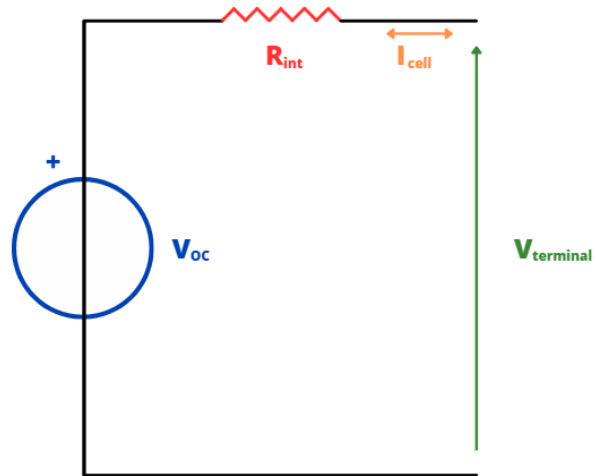


Figure 13: Cell electric scheme

To match the energy storage performance of the actual Chevy Spark BEV, the cells from the paper were configured in 121 series and 22 parallel. These cells are A123 26650 LiFePO4 lithium-ion cylindrical cells with a nominal voltage of 3.3 V and a rated capacity of 2.5 Ah. This configuration produces a battery with the characteristics expressed in the following equations:

$$R_{int \text{ batt}} = R_{cell} \cdot \frac{N_{series}}{N_{parallel}} \quad (\text{III})$$

$$V_{OCV\ cell} = V_{cell\ 1C\ disch} + 2.5 \cdot R_{cell} \quad (IV)$$

$$V_{batt} = V_{OCV\ cell} \cdot N_{series} \quad (V)$$

$$I_{batt} = I_{cell} \cdot N_{parallel} \quad (VI)$$

These equations were implemented in the Simulink® environment as follows:

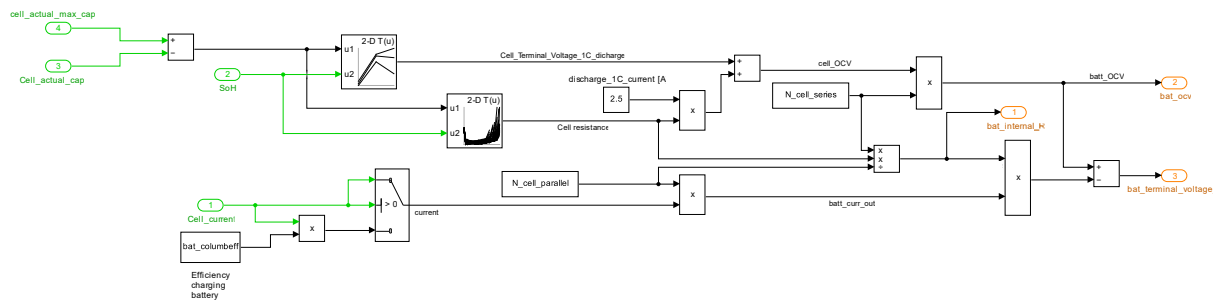


Figure 14: Simulink® Battery pack model

Within this model, *Cell actual max capacity* and *Cell actual capacity* serve as inputs. The difference between these values indicates the State of Charge (SOC) of the battery. This information is used to access lookup tables, based on experimental results from [15], which are dependent on the actual State of Health (SOH) and SOC. These tables, depicted in Figure 12, reveal the influence of SOC and SOH on OCV and Internal Resistance curves. The first lookup table yields the cell terminal voltage experimentally evaluated at a 1C discharge current (2.5 amperes). Knowing the cell capacity and the cell resistance from the second lookup table, it has been possible to determine the cell OCV and subsequently the battery OCV. The remaining components of this block calculate the battery pack internal resistance and output current. In this case it is important to notice that some preliminary assumptions were made before creating the model:

- A straightforward voltage generator in series with internal resistance is adequate for assessing battery dynamics in our study. Developing a comprehensive battery model would have required access to experimental data that was unavailable for this specific cell and would have exceeded the scope of our project.
- Has been assumed that the BMS is able to maintain the temperature of the pack constant at 25°C regardless external temperature and load conditions.

- The internal resistance is considered equal in both charging and discharging conditions.
- Uniform cell discharge/charge levels across the battery pack.

3.3 SOH Estimation Model

Having defined the equivalent circuit of the battery, has been possible to go through the SOH estimator block, illustrated in the following scheme:

This structure encompasses the three primary blocks: the SOC estimator (already present in the model and modified to consider SOH), the Battery Voltage output block (converting cell variables to

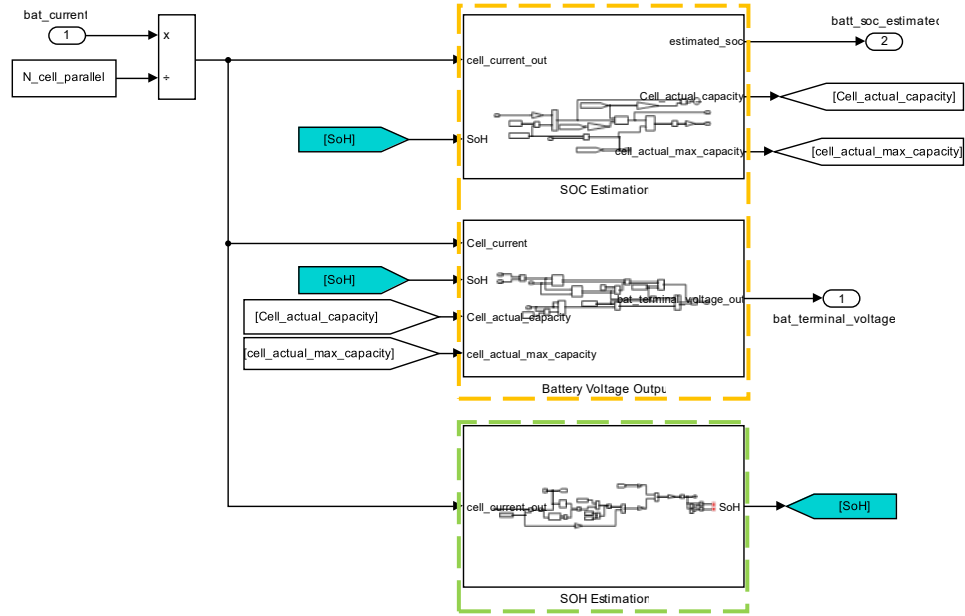


Figure 15: Simulink® battery model

equivalent battery pack values, discussed earlier), and the battery SOH estimator, which we will detail. The block takes cell current output as input and employs Arrhenius formulation to estimate the battery's State of Health (SOH) through the following equation:

$$Ah_{batt\%} = B(c) \cdot e^{-\frac{Af}{T}} \cdot Ah_{tp}^z \quad (VII)$$

In this equation $Ah_{batt\%}$ represents the cell capacity loss as percentage, B is a pre-exponential factor determined through experimental fitting of real data in [15]. Its values vary with the current C-rate, considering both calendar aging and wear due to battery usage. The pre-exponential factor values are tabulated below:

Empirical pre-exponential factor, B(c)	[21681; 12934; 15512; 15512]
Current C-rate, c	[2; 6; 10; 20]

Table 2: Pre-exponential factor values

c is the current C-rate (the ratio of current to nominal cell capacity $I/C_{nominal}$), A_f is the aging factor defined as follows:

$$A_f = 3814.7 - 44 \cdot c \quad (\text{VIII})$$

and T represent the cell temperature (considered fixed at 25 °C). $Ah_{tp}(c, T)$ denotes the total amper-hours throughput considered for a specific c -rate and cell temperature, and z is an exponential factor set experimentally equal to 0.55.

To ascertain the battery's cycle life, we assume End of Life (EoL) occurs when 20% of battery capacity is lost. By setting $Ah_batt\%$ to 20% and inverting equation (VII), we can calculate the number of cycles the battery can withstand up to EoL for a given c -rate and cell temperature:

$$N(c, T) = \frac{Ah_{tp}(c, T)}{2 \cdot Ah_{batt}} \quad (\text{IX})$$

Here Ah_{batt} is the rated battery capacity evaluated in ampere-hours, which for an A123 cell is 2.5 Ah.

Once this variable has been evaluated it is possible to evaluate the SOH(t) at a specific instant 't' integrating equation over time (X) providing the output of the estimator block:

$$SOH(c, T) = \frac{0.2 \cdot c}{3600 \cdot N(c, T)} \quad (\text{X})$$

$$SOH(t) = SOH_0 - \int_0^t SOH \cdot d\tau \quad (\text{XI})$$

In this case, the state of health for the initial condition (SOH_0) is set to 1, indicating a new battery cell. After this block outputs the current SOH, it enters the two remaining blocks in the battery model, modifying the cell OCV and internal resistance. Subsequently, it enters the SOC estimator, adjusting the actual max cell capacity to account for reduced energy storage capabilities due to degradation.

3.4 Simulation Set-up

With the model now complete, a method to evaluate battery degradation through a complete discharge cycle, ranging from 95% to 5% SOC is required. A cycle iteration and battery recharging process has been implemented. When the battery's SOC is considered insufficient to start a new cycle or when the driving cycle ended, the external input imposing the driving cycle was either set to zero to charge the battery or the cycle time was reset to initiate a new cycle. This procedure is illustrated in the following figure depicting the external architecture governing the vehicle plant:

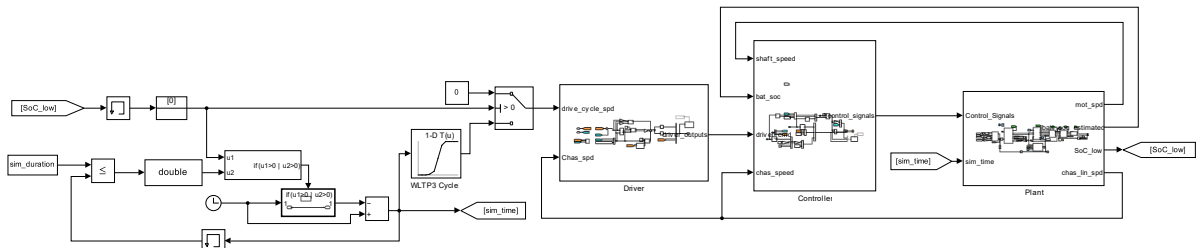


Figure 16: Driving cycle reset/charging

The *SoC low* variable is triggered when the cycle ends with a SOC too low to commence a new one. When this occurs, the vehicle speed is forced constant to zero, enabling the battery to recharge. During this time, within the battery block, a negative current is enforced, designed to match the manufacturer's declared charging time for full battery charge, which was set lower than 7 hours for a US standard AC 240V charging (non-fast charging) using a dedicated charging station [17]. Observing the following charts, it is possible to observe the behaviour of the vehicle when charging occurs:

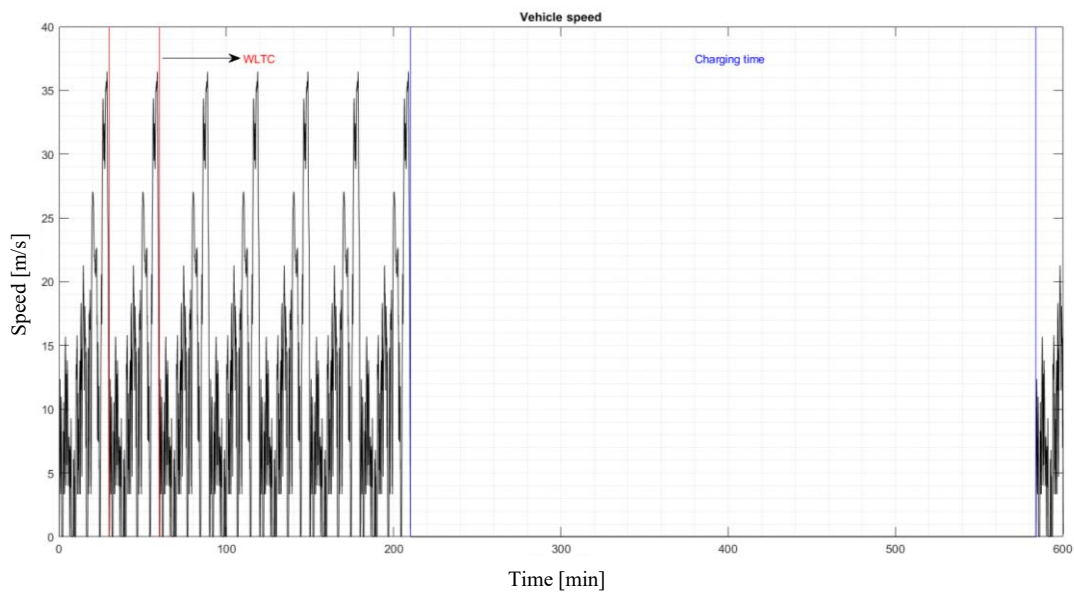


Figure 17: WLTC vehicle speed charging

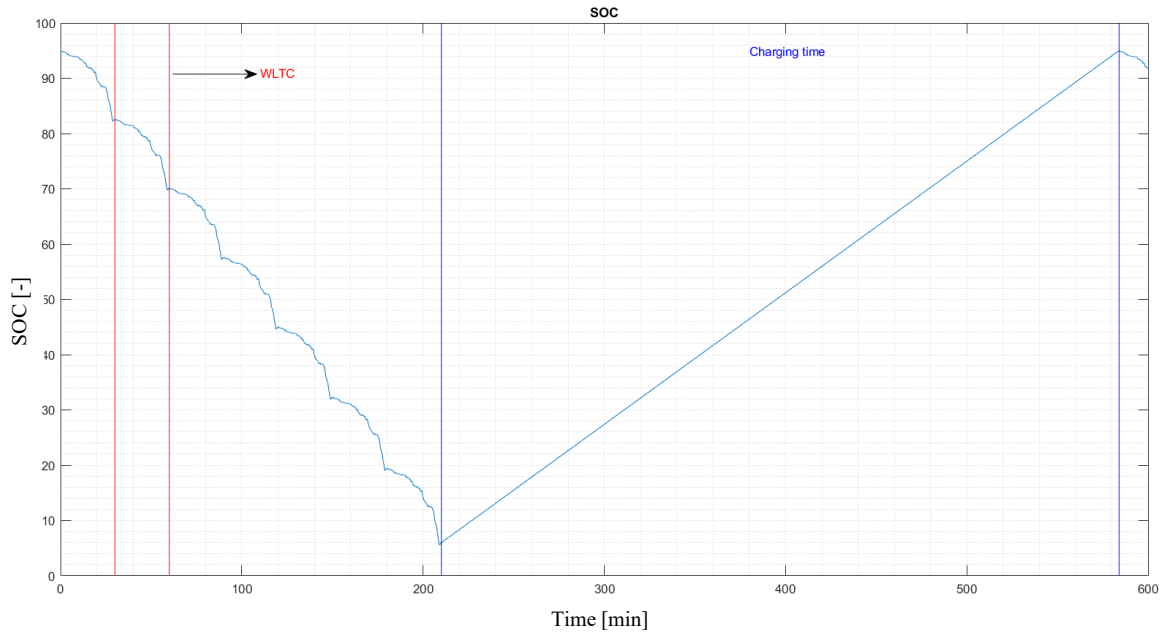


Figure 18: WLTC SOC charging

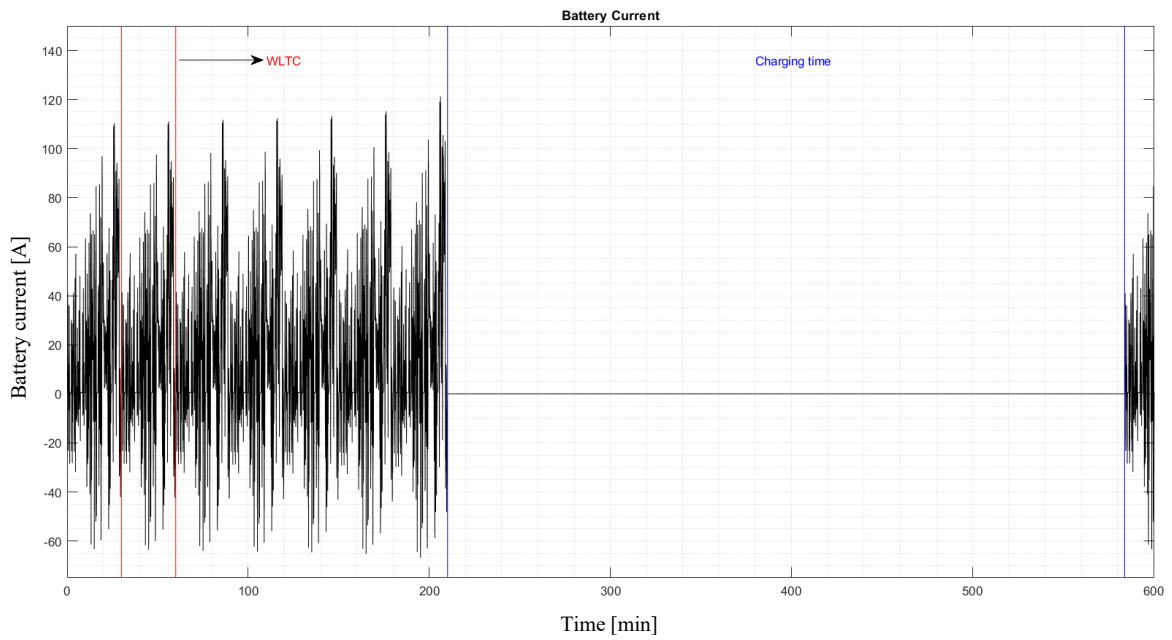


Figure 19: WLTC Battery Current charging

We can observe a sequence of driving cycles in the graph. The red portion represents a single WLTC (Worldwide Harmonized Light Vehicles Test Cycle), while the charging phase is depicted in blue. When the state of charge (SOC) at the end of a cycle is insufficient to initiate another one, the vehicle enters a charging phase. During this phase, the vehicle remains stationary, maintaining a speed of zero. As a result, the battery current also reaches zero, as the vehicle is not in motion. Meanwhile, the SOC gradually increases, accumulating energy within the battery until it reaches 95%. At this point, the vehicle can recommence the driving cycle.

This process can be repeated as many times as necessary and for each driving cycle to assess battery degradation and its impact on vehicle performance.


This model provides a means to evaluate battery degradation, relying solely on battery current output as input. However, it's worth noting that this model has limitations as it is semi-empirical and based on parameters derived from experiments conducted at constant battery temperature and C-rate, with results being fit to the model. Nevertheless, in the context of current industry trends, where car manufacturers should guarantee in the future a minimum number of kilometres until End of Life (EOL), (according to EURO 7 proposal normative the limit is set to 160 000 km [8]), such experiments will become essential. As a result, this model can be readily adapted, taking also into account that these experiments needed for the model implementation can be conducted at the single-cell level, simplifying their implementation.

4. Vehicle speed trajectory optimization strategy

4.1 How Autonomous and Connected vehicle technology can improve energy consumption and reduce battery fading in a BEV

The essence of this chapter lies in exploiting the capabilities of connected vehicle technology and sensors information to optimize vehicle speed trajectories, especially in mixed driving cycle scenarios that encompass urban, extra-urban, and highway conditions. However, before diving into the specifics of this endeavour, it is essential to provide a brief overview of autonomous and connected vehicle technology, elucidating their current capabilities and how they are harnessed in this chapter. Given the challenges associated with Battery Electric Vehicles (BEVs), including range anxiety and battery degradation, the marriage of connectivity and autonomous drive presents a compelling solution. This synergy offers the potential to minimize energy consumption significantly, particularly in architectures where limited energy management can be performed at the powertrain level, as seen in the BEV architecture used as the baseline in this project, equipped with only one electric motor.

4.1.1 Autonomous vehicle technology



SAE J3016™ LEVELS OF DRIVING AUTOMATION™

Learn more here: [sae.org/standards/content/j3016_202104](https://www.sae.org/standards/content/j3016_202104)

Copyright © 2021 SAE International. The summary table may be freely copied and distributed AS-IS provided that SAE International is acknowledged as the source of the content.

		SAE LEVEL 0™	SAE LEVEL 1™	SAE LEVEL 2™	SAE LEVEL 3™	SAE LEVEL 4™	SAE LEVEL 5™
What does the human in the driver's seat have to do?		You are driving whenever these driver support features are engaged – even if your feet are off the pedals and you are not steering			You are not driving when these automated driving features are engaged – even if you are seated in “the driver’s seat”		
		You must constantly supervise these support features; you must steer, brake or accelerate as needed to maintain safety			When the feature requests, you must drive	These automated driving features will not require you to take over driving	
		Copyright © 2021 SAE International.					
		These are driver support features			These are automated driving features		
What do these features do?		These features are limited to providing warnings and momentary assistance	These features provide steering OR brake/acceleration support to the driver	These features provide steering AND brake/acceleration support to the driver	These features can drive the vehicle under limited conditions and will not operate unless all required conditions are met	This feature can drive the vehicle under all conditions	
	Example Features	<ul style="list-style-type: none"> • automatic emergency braking • blind spot warning • lane departure warning 	<ul style="list-style-type: none"> • lane centering OR adaptive cruise control 	<ul style="list-style-type: none"> • lane centering AND adaptive cruise control at the same time 	<ul style="list-style-type: none"> • traffic jam chauffeur 	<ul style="list-style-type: none"> • local driverless taxi • pedals/steering wheel may or may not be installed 	<ul style="list-style-type: none"> • same as level 4, but feature can drive everywhere in all conditions

Figure 20: SAE level of driving automation [19]

Within the field of autonomous vehicle technology, it is crucial to understand the various levels of automation. The levels, as defined by [19], range from 0 to 5, each representing a different degree of automation and driver involvement.

- **LEVEL 0:** At this stage, the vehicle provides warnings such as blind-spot warnings, lane departure warnings, and automatic emergency braking, but no physical support for driving.
- **LEVEL 1:** Level 1 offers support for either steering or braking/accelerating to assist the driver.
- **LEVEL 2:** This level provides support for both longitudinal and lateral dynamics, incorporating features like lane centering and Adaptive Cruise Control (ACC).

The transition from Level 2 to Level 3 marks a significant shift.

- **LEVEL 3:** the driver could become distracted, as the vehicle must allow the driver time to react in case of system faults, making it essential for the driver to take over when needed.
- **LEVEL 4:** the driver is never expected to take control of the vehicle. Pedals and steering can be eliminated. The distinction between Level 4 and fully autonomous vehicles lies in the fact that a Level 4 vehicle may not be capable of driving in all possible conditions. Therefore, it must respond appropriately and safely when it encounters challenging conditions.
- **LEVEL 5:** This represents the highest level of automation, where the vehicle is fully capable of driving in any scenario and under all external conditions.

Notably, the transition from Level 2 to Level 3 is substantial due to the shift in responsibility with Level 3, introducing the need for the vehicle to monitor the environment comprehensively. In this scenario, the vehicle must offer ample time for the driver to react in critical situations, making fault attribution challenging in case of an accident. Levels 3 and above also highlight a significant challenge: the inability of current technology to predict human intention reliably, given its unpredictable and stochastic nature. This challenge is exacerbated when autonomous vehicles operate in mixed environments, further increasing the technology requirements compared to environments where all vehicles are fully autonomous. As automation levels progress from 0 to 5, the driver's effort in driving diminishes, paving the way for more complex optimization strategies, reducing human errors, and enhancing travel comfort in all conditions.

In order to implement this level of automation, sensor fusion is required, namely combine different type of sensor in order to have a complete overview of the environment around the vehicle. Radars, cameras and lidar are the most used to control vehicle dynamics. Also, ultra-sounds sensors are frequently used but are not of interest for this application since more related to blind spot monitoring or parking manoeuvre due to their very small detection range. The Radar instead, can catch metallic object up to 250 m with a 120° horizontal range and 30° vertical range [21]. It has a very high accuracy for long distanced detection and can distinguish objects very closed between each other. It can work almost in any weather condition. Anyway, it has very poor object detection resolution, so we are able to understand the presence of an object without knowing what it is. Cameras are very cheap, can detect object longer than our eyes thanks to postproduction, can detect also non-metallic object but produce very heavy data and it's functioning is impaired by the weather conditions and cameras cleaning. Lidars, from their part, can detect object at very high distance (240 m) and with a very high accuracy [20]. Differently from radar they detect object and are able to distinguish them. They create a 3D map of the environment anyway they are very expensive and very sensitive also to very small particles that can reflect the light and impair their functioning.

Given the focus on Adaptive Cruise Control (ACC) in the strategy to be described in detail, an automation Level 1 technology, primarily utilizing radar, suffices, which could be supported, in particular conditions where the sensor cannot work properly due to its limitations, by connected vehicle information coming from vehicle or infrastructure.

4.1.2 Connected vehicle technology

In recent years, as highlighted by [22], the automotive industry has witnessed rapid advancements in vehicle-related technologies, notably in the context of connected vehicle (CV) technology and automation. These developments have collectively shaped a shared vision of future vehicles characterized by their automation, connectivity, electrification, and shared mobility. Notably, the advent of connected vehicle (CV) technology has ushered in a new era for modern intelligent transportation systems, unlocking a realm of virtually limitless potential applications.

The pivotal enablers of communication between vehicles, as elucidated by [23], are DSRC (Direct Short-Range Communications) and 5G Cellular network technologies. Each of these technologies possesses its own set of advantages and disadvantages, contingent upon the specific use case. DSRC, characterized by its short-range communication capabilities (spanning

hundreds of meters), facilitates the rapid transmission of concise messages with minimal latency. In contrast, 5G technology boasts the ability to transmit data across substantial distances (on the order of kilometres, provided there are no persistent metallic obstacles). However, it does come with higher latency compared to DSRC. In the context of our intended application, which is non-safety related, the adoption of 5G technology emerges as a pragmatic choice. This is primarily due to the significant investment required for DSRC implementation. Furthermore, the presence of 5G in cellular networks, positions it as an accessible and effective solution, with the potential to support safety-related applications when 5G stand-alone configurations become available. Consequently, the integration of connected vehicle technology enhances a vehicle's situational awareness, augmenting sensor robustness and acting as a redundancy measure. This approach allows the vehicle to anticipate scenarios in which sensors may fail due to obstructions, thereby expanding the operational design domain of autonomous vehicles. Notably, the degree of connectivity among vehicles and the extent of shared data directly correlates with the effectiveness of a vehicle's environmental perception.

4.2 Connected Adaptive Cruise Control (CACC)

Examining the presently accessible technology and drawing upon insights from [24], we have the opportunity to delve into ACC controllers and explore their potential applications. In the context of Level 1 or 2 automation, Autonomous Vehicles (AVs) rely heavily on the Adaptive Cruise Control (ACC) algorithm to respond to the movements of preceding vehicles within traffic. The design of these controllers generally falls into one of two categories: reactive controllers or predictive controllers. Reactive ACC controllers (RACC) utilize explicit feedback control laws, typically parameterized to allow for optimization of controller parameters, especially with regards to energy efficiency and car following dynamics. In contrast, predictive ACC (PACC) takes a more proactive approach by directly optimizing the future trajectory based on predictions of the leading vehicle's future movements. This approach yields substantial enhancements in energy efficiency. Importantly, by establishing connections between vehicles, the accuracy of future predictions can be significantly improved. Additionally, the utilization of navigation systems further refines the ability to predict the trajectory of leading vehicles, offering a more precise glimpse into their planned routes. As we peer into the near future of transportation, it becomes increasingly evident that traffic scenarios will evolve towards a heterogeneous mix of connected and non-connected vehicles.

Controllers tailored to function effectively in these mixed traffic environments are collectively referred to as Connected Cruise Control (CCC).

Given the context elucidated above, the strategy developed within this thesis can be aptly categorized as a Predictive Adaptive Cruise Control system capable of operating seamlessly within mixed traffic scenarios. This approach leverages vehicle information from various sources, including other vehicles, infrastructure, and sensors. As a result, the nomenclature "Connected Adaptive Cruise Control" has been chosen to succinctly encapsulate the essence of the implemented strategy.

4.2.1 CACC model implementation

To develop a predictive adaptive cruise control system capable of effectively functioning across diverse driving scenarios by harnessing sensor data and connectivity, we can explore three primary approaches:

1. **Rule-Based Approach:** This approach relies on predefined rules that trigger specific actions when particular conditions arise. It offers simplicity and computational efficiency, but it has inherent limitations. These rules are often tailored to specific situations and can be challenging to generalize across a wide range of scenarios.
2. **Reinforcement Learning:** Leveraging neural networks, this approach involves training an agent to learn optimal actions by interacting with its environment. The agent learns from the consequences of its actions, making it adaptable to various situations. However, one significant drawback is the substantial need for training data to ensure effective performance across diverse conditions.
3. **Model Predictive Control (MPC):** MPC employs an optimization strategy driven by a cost function designed to satisfy desired requirements. It achieves this by predicting the future state of the system and determining actions that minimize the cost while avoiding unfeasible conditions.

Given the project's objectives, which prioritize reliability and manageable complexity, MPC was chosen as the most suitable option. Before delving into the implementation details and results quantification, preliminary data were acquired on the Worldwide Harmonized Light Vehicles Test Cycle (WLTC), EPA cycle, and a basic car-following strategy involving one leading vehicle and an ego vehicle (representing the vehicle I want to control) as baseline for future comparisons.

4.2.2 Vehicles environment set-up

To establish a car-following model, which mathematically describes how vehicles follow one another on a road, the behaviour of the leading vehicle to be followed must be selected. In this case, as explained in Chapter 2, it is assumed that the leading vehicle precisely follows either a WLTC cycle or an EPA cycle. Several assumptions were made regarding the environmental setup for the model:

- Only two vehicles are present in the environment.
- No vehicles enter or exit the lane.
- Only longitudinal dynamic is examined and controlled.
- All types of road conditions, from urban to highway, are considered without accounting for traffic, focusing solely on the actions of the leading vehicle.
- Information from the leading vehicle, including actual speed and position, is available through vehicle-to-vehicle (V2V) or vehicle-to-infrastructure (V2I) communication or sensors, giving the possibility to the leading and ego vehicle to be either connected or non-connected.
- Disturbances in the leading vehicle's information are considered as white noise with a specified maximum amplitude, accounting for sensor accuracy and communication delays.

The results obtained from the leading vehicle, which precisely follows the WLTC or EPA cycle, are presented in the following section. Various aspects are examined to encompass different characteristics:

- **Energy Consumption:** A primary concern in the project, the state of charge (SOC) of the battery is monitored and controlled.
- **Battery Health:** Indirectly affected by control commands, the state of health (SOH) of the battery is monitored to assess potential benefits.
- **Comfort:** To implement an autonomous driving strategy, comfort is essential. Abrupt accelerations or decelerations that would make the strategy impractical in a real vehicle are monitored through jerk measurements.
- **Input Command:** Monitoring acceleration ensures that the optimal solution obtained is feasible without high-frequency oscillations in the control variable.
- **Following Capability and Time:** The strategy should not only reduce energy consumption but also ensure the ability to follow without significantly impacting travel time, thereby improving traffic flow and passenger satisfaction.

- **Safety:** While pursuing performance improvements, safety is paramount. A safety distance that varies with speed is imposed and observed in all scenarios to ensure safety.

These pieces of information are provided to demonstrate the model's capability to enhance performance while considering realistic factors such as comfort and safety.

4.3 Leading vehicle data

The results of a vehicle following precisely the WLTC and EPA cycles are presented here:

WLTC driver	ΔSOC	max acc [m/s ²]	Jerk max [m/s ³]	Time cycle (23,25 km) [s]	ΔSOH
	12,39	1,75	14,06	1791,50	7,329 E-06
EPA driver	ΔSOC	max acc [m/s ²]	Jerk max [m/s ³]	Time cycle (28,49 km) [s]	ΔSOH
	13,05	1,51	15,90	2130,70	7,147 E-06

Table 3: WLTC/EPA results

In this scenario the vehicle initial conditions are $SOC = 95\%$, $SOH = 1$, $v_0 = 0$ (initial vehicle speed) and $x_0 = 0$ (initial position). The values in the table represent the variations at the end of one cycle with respect to the initial conditions and the maximum values recorded during the simulation.

One interesting observation derived from these results is that, despite WLTC being a more aggressive cycle, the SOC degradation at the end of it is smaller compared to EPA. However, when considering the number of kilometres travelled, since the second cycle is longer, the ratio $\Delta SOC / \text{travelled distance}$ confirms the earlier observation. The SOH also supports this, with a greater degradation even when considering a shorter distance. A plot illustrating these results will serve as a reference in all subsequent plots, referred to as 'Leading vehicle,' for the purpose of comparing the analysed methods with a vehicle that precisely replicates these cycles.

4.4 Constant time gap (CTG) method

4.4.1 Model description

The CTG method simulates a reactive adaptive cruise control strategy in which vehicle speed varies according to the leading vehicle's speed. The goal is to maintain a predetermined time interval from the leading vehicle without the need for complex optimization strategies. This method is characterized by its simplicity and low computational cost. Instead of imposing a specific desired distance between the two vehicles, it focuses on maintaining a certain time gap,

which can be readily converted into a distance based on the vehicle's speed using the following relation:

$$L_{desired} = h_{ego} \cdot \dot{x}_{ego} + x_{0\ ego} \quad (XII)$$

Here \dot{x}_{ego} represent the actual ego speed, h_{ego} is the desired constant time gap (set to 2.7 seconds to ensure both safe distance and smooth traffic flow for various speeds) and $x_{0\ ego}$ is the distance when the vehicle is stand still (set to 5 meters). According to [25] this method ensures that errors within a platoon of vehicles do not propagate, ensuring the so called ‘String Stability’. The controller based on this method according to the same paper, follows those simple relations:

$$\varepsilon = x_{ego} - x_{leading} \quad (XIII)$$

$$\delta = \varepsilon + L_{desired} \quad (XIV)$$

$$a_{command} = -\frac{1}{h_{ego}}(\lambda\delta + \dot{\varepsilon}) \quad (XV)$$

Equation XIII calculates the actual distance between the two vehicles by subtracting their instantaneous positions. Equation XIV calculates the distance error between the actual distance and the desired distance. The last equation, Equation XV, combines the previous formulations to command acceleration based on the distance error and the difference in speed ($\dot{\varepsilon}$). The following representation illustrates the variables in the equation and aids in understanding how the controller functions:

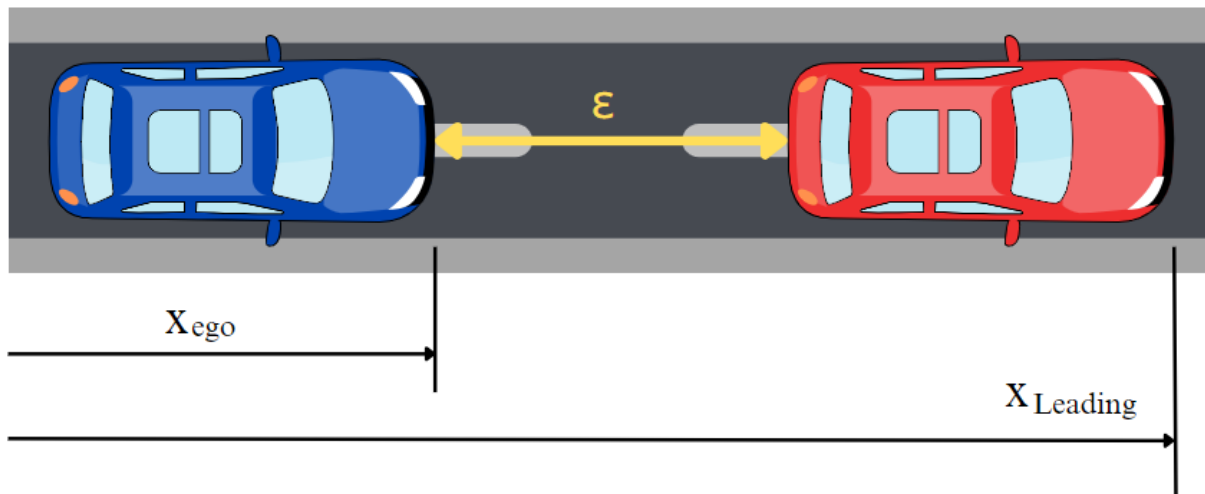


Figure 21: Following vehicle scheme

It's important to note that ε is always negative, resulting in δ ideally oscillating around zero. When the actual distance is smaller than the desired distance (indicating that the vehicle is below the safe distance limit), δ becomes positive, and the commanded acceleration is negative to increase the distance. Conversely, in the opposite case, when the ego vehicle's speed is higher than the leading vehicle's speed, ε becomes positive, leading to a commanded negative acceleration. The only parameter that requires tuning in this controller is λ , which determines the controller's sensitivity to relative distance versus relative speed. For the current vehicle, λ has been set to 0.2 [1/s].

The following strategy has been implemented in Simulink®, utilizing CTG as an input for the BEV driver, as depicted in the figure below:

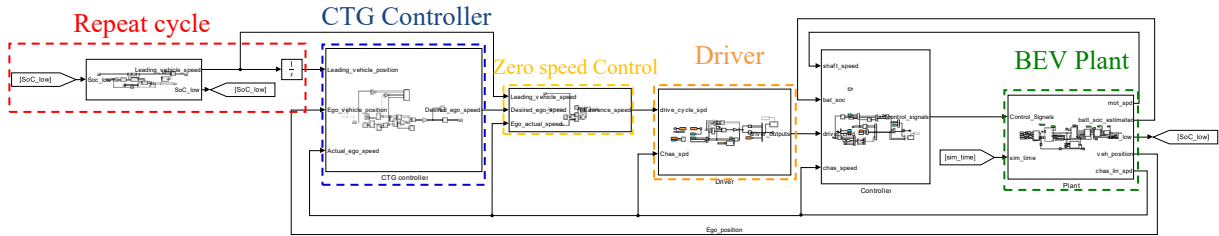


Figure 22: Simulink® CTG vehicle architecture

In this diagram, key components are color-coded for clarity. The red block, highlighted in red, enables the cycle to restart or recharge the vehicle if the State of Charge (SOC) at the end of the cycle is insufficient to begin another one. The blue block represents the previously described controller, which takes leading and ego vehicle positions and ego speed as inputs and provides the commanded acceleration to the driver, depicted in the orange block. The yellow block ensures that the vehicle comes to a complete stop by forcing the driver's input to zero when the vehicle speed falls below 0.01 m/s. Lastly, the green block represents the vehicle's plant, which receives inputs from the preceding blocks and responds by generating feedback for the system. The simulation results obtained using this control strategy are presented alongside those of the leading vehicle, which corresponds to a vehicle precisely replicating the driving cycle.

4.4.2 CTG results

In the first section, we present the results obtained when a leading vehicle follows a WLTC. The first two plots reveal that the CTG attempts to mimic the leading vehicle's speed profile, even if with some discrepancies due to the distance between them. Because the ego vehicle lags the leading vehicle, it reduces speed less or it has smaller peaks in some conditions. Analysing the vehicles relative distances, we observe a significant limitation of this approach. Since it

lacks an optimization strategy, the control system merely aims to keep the vehicle around the safety distance, maintaining δ close to zero with oscillations generally under 1 meter. This happens regardless of the energy needed or safety distance requirements, resulting in certain conditions where the relative distance (the disparity between actual and desired distances) falls below the safety limit, anyway of a very small amount. Indeed, when the relative distance δ turns negative, it signifies that the actual distance is less than the desired safe distance.

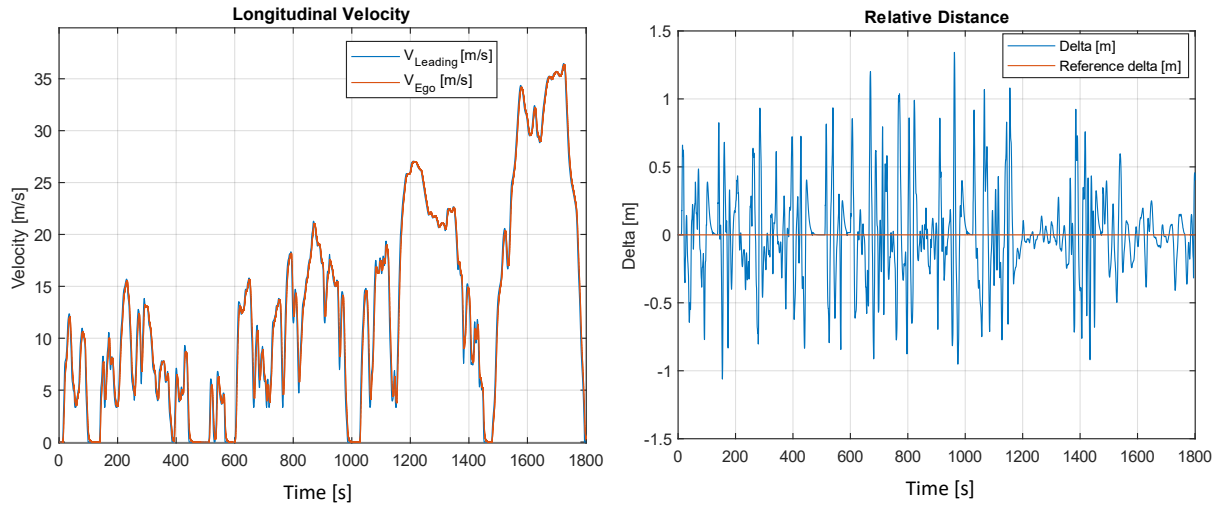


Figure 23: CTG(WLTC) Speed profile - Distance Error Plots

As a result, this impact is evident in the State of Charge (SOC) and State of Health (SOH), both of which are influenced by the accelerations and peak power demands. A system that responds solely to the objective of maintaining a constant distance between vehicles, without considering future predictions, results in higher energy consumption and increased battery degradation, as illustrated in Figure 24.

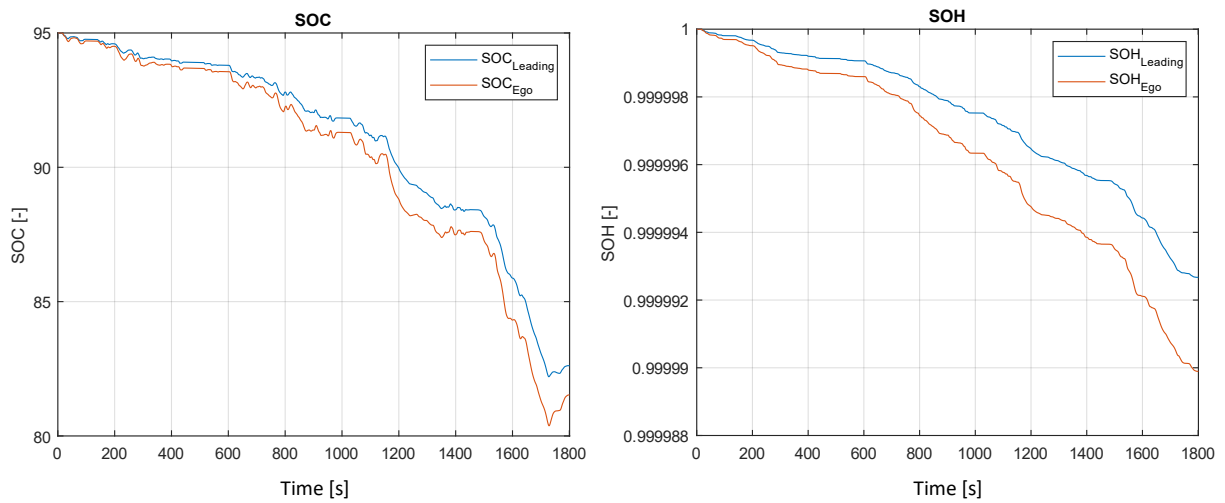


Figure 24: CTG(WLTC) SOC - SOH Plots

The acceleration data confirms our earlier observations, with the ego vehicle being in retard. Consequently, it must react swiftly to the leading vehicle's movements, resulting in more significant accelerations to catch up. Observing the traction power, one can discern a correlation between acceleration and power demand, where a higher request on the acceleration peaks results in a proportionate increase in the requested power peaks. This observation helps provide a more comprehensive explanation for the heightened energy consumption and accelerated battery degradation experienced within a single cycle.

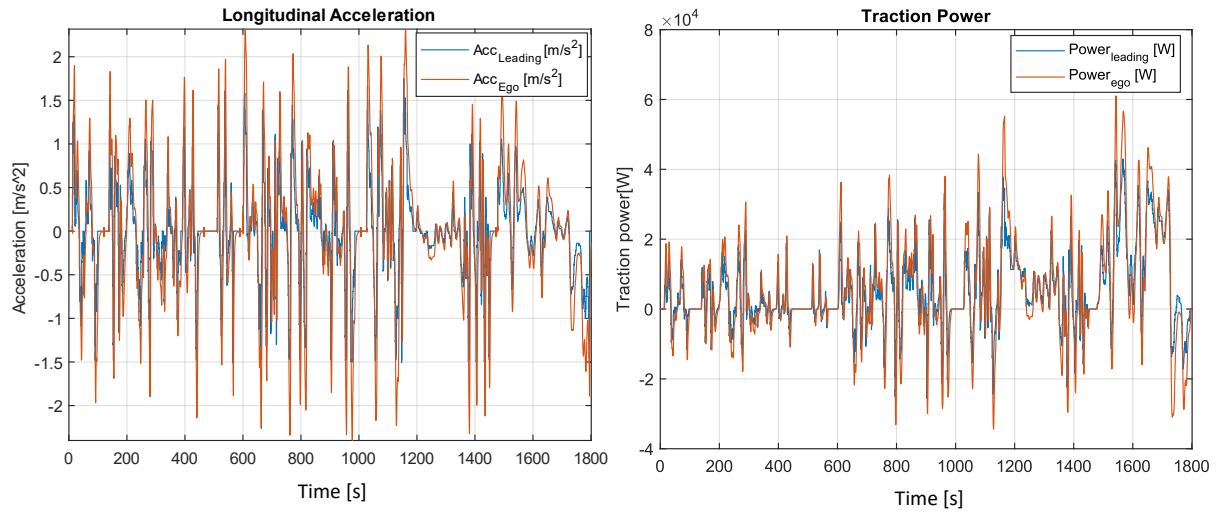


Figure 25: CTG(WLTC) Acceleration – Traction Power Plots

The same principles apply when the ego vehicle follows an EPA cycle, with similar trends but variations in the magnitude of results due to inherent differences in the driving cycles.

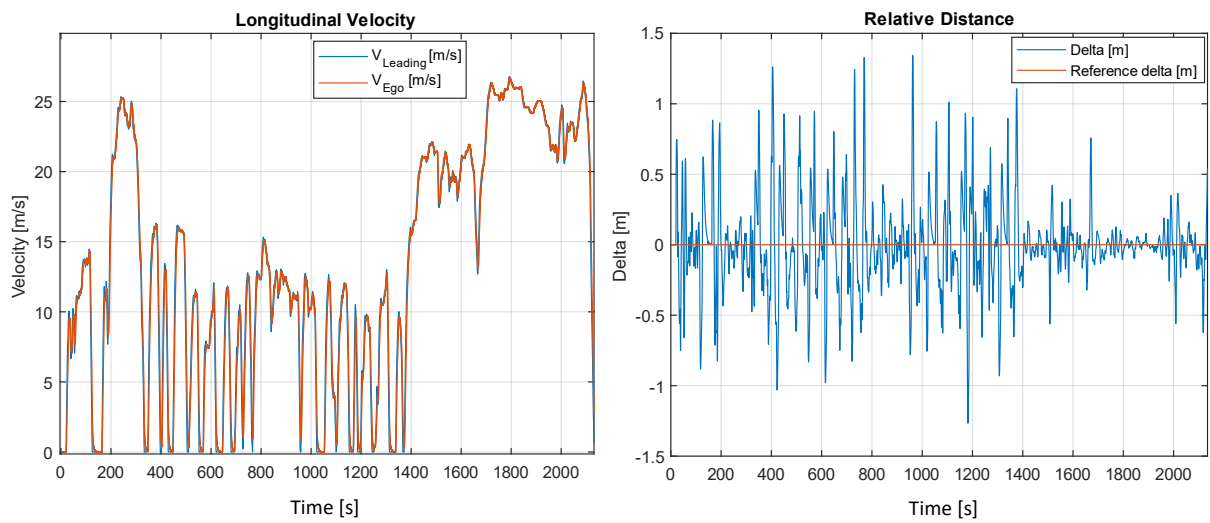


Figure 26: CTG(EPA) Speed profile - Distance error Plots

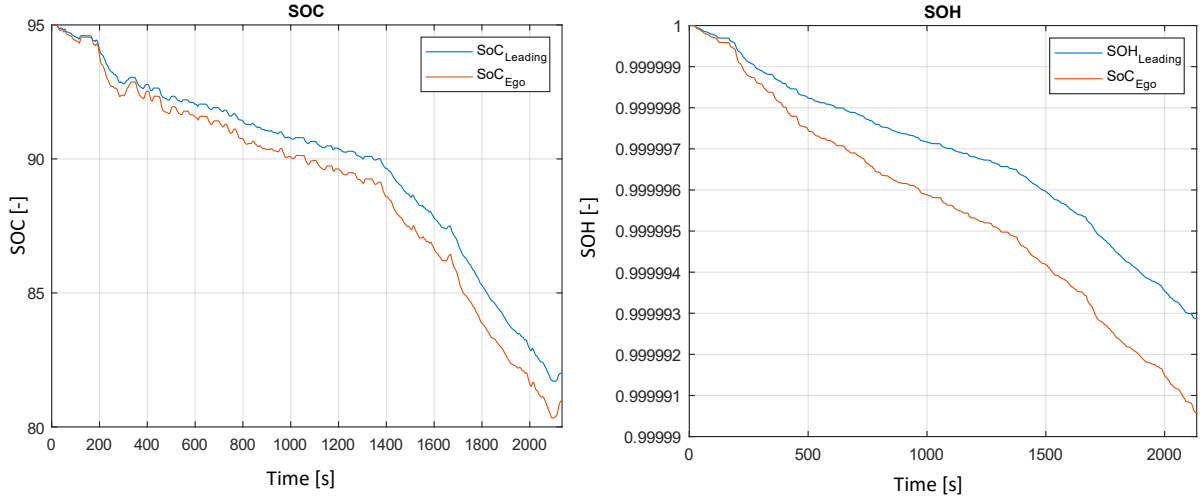


Figure 27: CTG(EPA) SOC -SOH Plots

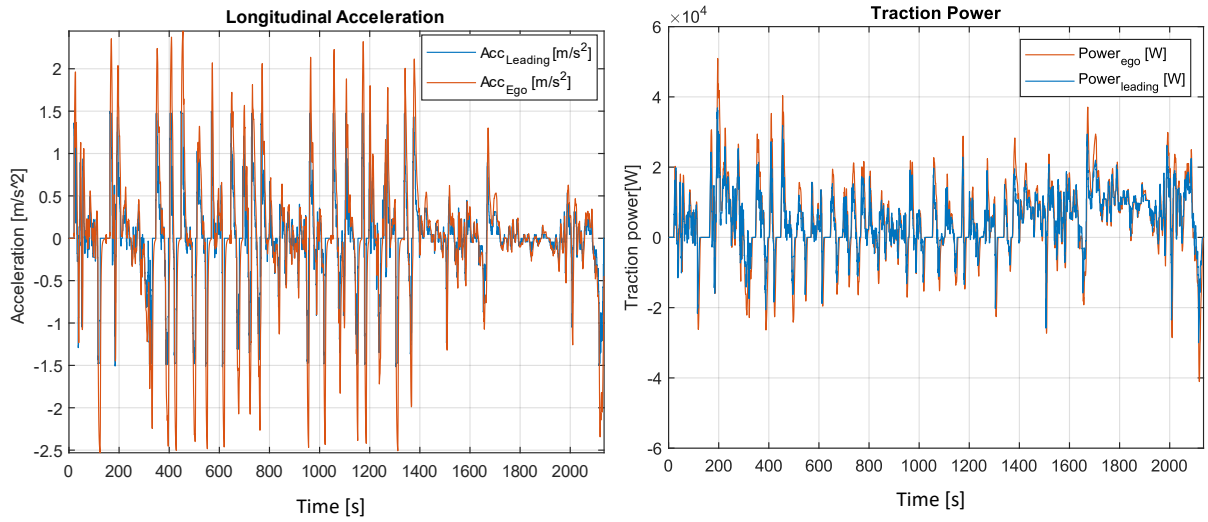


Figure 28: CTG(EPA) Acceleration – Traction Power Plots

The tables below provide a summary of the results at the end of the cycle for the ego vehicle controlled by the CTG, following either a WLTC or EPA cycle.

WLTC - CTG	ΔSOC	$ \max acc [m/s^2]$	$Jerk \max [m/s^3]$	Time cycle (23,25 km) [s]	ΔSOH
	13,48	2,4	3,92	1793,50	10,110 E-06
EPA - CTG	ΔSOC	$ \max acc [m/s^2]$	$Jerk \max [m/s^3]$	Time cycle (28,49 km) [s]	ΔSOH
	14,03	2,53	6,26	2131,90	9,419 E-06

Table 4: CTG results for WLTC and EPA

In conclusion, the CTG is a straightforward controller that effectively follows a leading vehicle at a certain distance with minimal computational cost. However, as highlighted in the previous section, its lack of additional constraints sacrifices energy efficiency and battery life. This suggests that alternative approaches should be explored, as detailed in this thesis.

4.5 Model Predictive Control (MPC)

Recognizing the limitations of the previous approach, we will now delve into a more complex yet efficient method. This approach, as the name suggests, centres on prediction along a specific horizon of future vehicle states to create a smoother vehicle speed profile and enhance overall travel efficiency. In this thesis, we explore the following strategies:

- Non-linear model predictive control (NMPC): This approach employs the entire vehicle plant to simulate future predictions. Consequently, it features a highly non-linear and computationally intensive architecture, serving as a benchmark for subsequent steps.
- Linear model predictive control (LMPC): employs a linearized model, leveraging specific relationships to approximate the real vehicle plant's behaviour based on knowledge gained from the benchmark solution.

4.5.1 NMPC architecture

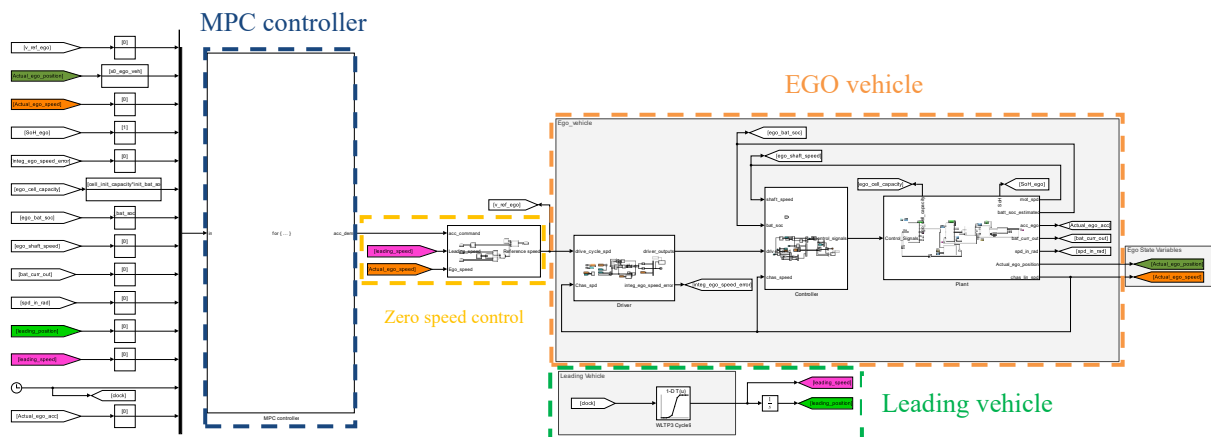


Figure 29: NMPC architecture

In Figure 29, you'll observe a resemblance to the previously explained CTG architecture. To the right, we have the Ego vehicle components in orange, including the driver, controller, and plant. The Leading vehicle, in green, is represented by the driving cycle. Moving to the left, the yellow block denotes the vehicle's zero-speed control, previously described, and the blue block signifies the MPC block containing all the necessary inputs derived from actual ego and leading vehicle information to facilitate predictions. At the core of MPC lies the concept of iterative modelling over multiple time steps. In this case, a non-linear model represents the vehicle's behaviour, with the aim of finding the best control actions for future steps. These control actions are chosen based on a Cost Function, which, taking vehicle states as input, provides a cost for each action. After assessing the cost for each action, a feasibility check is performed to

determine the definitive best action for that specific time step. Different structures are available for MPC, with the Predictive Horizon (PH) and Controlled Horizon (CH) playing critical roles. These factors significantly impact computational cost and result accuracy:

- PH: represents the span of time or states into the future for which the controller calculates and evaluates the system's predicted responses to different control inputs. A longer predictive horizon allows the controller to make predictions further into the future, enabling it to better anticipate and plan for future system behaviour.
- CH: represents the time or states into the future for which the controller actively computes and applies control inputs to the system. The control horizon is typically shorter than the predictive horizon. It defines the finite sequence of control inputs that the controller will use over a specific time period to optimize the system's performance while considering constraints.

To understand the pros and cons of different architectures, a description of the implemented model is done with the related assumptions and the imposed control. The first model, depicted in Figure 29, employs a constant control action for the entire PH (tested for values of 2, 5, and 10 time steps) with a CH of one time step.

Key assumption for realistic predictions in this model includes:

- Leading vehicle speed (acquired from sensors or connectivity) remains constant during the predictive horizons. This assumption holds since, based on the aggressive WLTC cycle, the maximum variation in one time step for peak speed values is only 0.175 m/s, making it a valid hypothesis.
- Only one control variable is utilized: the commanded acceleration, which enters the driver. To further simplify the model, a constant acceleration for the entire PH is chosen for the initial simulations.

To comprehend the model's actions, let's outline the process:

1. Define all the necessary input necessary to define the Ego and Leading vehicle states for the current instant is crucial for successful MPC implementation.
2. Access the MPC block where various accelerations are tested by leveraging a for loop.
3. For each tested acceleration, the model simulates the vehicle state evolution for the entire Predictive Horizon (PH) while considering a constant acceleration. Consequently, a for loop spanning the entire PH duration is necessary.
4. Evaluate the cost function for each locally simulated time-step and accumulate it to assess the overall cost for the entire PH.

5. Conduct a feasibility check for each acceleration to discard control actions leading to unfeasible conditions.
6. Select the optimal acceleration for future use in the Controlled Horizon (CH).
7. Update real ego plant and feed back the vehicle states inside the MPC block after CH in order to restart from step 1.

Now that we have understood how the structure operates, let's delve into each step in detail, elucidating the implementation process.

1.DEFINE INPUT

Precisely defining the input is a critical step in implementing MPC. As iteration is a core element, using Simulink® 'for iteration block' does not allow the use of 'integrator and derivative blocks.' Moreover, feedback cannot be incorporated since the program simulates the flow of all blocks anew with each iteration. Consequently, to work with the vehicle model, we have substituted these blocks by exploiting the mathematical relations governing integrator blocks:

$$Int_{out}(t) = Int_{out}(t - 1) + var_{in} \cdot \Delta t \quad (XVI)$$

Where the output of the integrator is performed summing the previous integrator output (obtained from ego plant simulated at previous time step) to the variable that must be integrated multiplied times the sample time interval. This approach enables integration within the iteration block. Similarly, for derivatives, Equation XVII demonstrates how the derivative output is found:

$$der_{out}(t) = \frac{var_{in}(t) + var_{in}(t-1)}{\Delta t} \quad (XVII)$$

By considering the current and previous values of the variable over the sample time, the derivative is calculated. This is the reason why the input for the MPC block in figure 29, requires this so high number of variables, since the complexity of the iterated model is large and the results for the integrator and derivative variables at previous interval are necessary. Furthermore, these variables include the state variables required for the cost function, namely Ego and Leading actual position and speed, as well as Ego SOC. Subsequently, we will elucidate how the feedback aspect has been managed to make predictions extending beyond a single time-step.

2.ACCELERATION FOR LOOP

Upon entering the MPC block, two For Loop blocks are nested within one another, as illustrated in Figure 30.

The first loop (light blue) is employed to test different accelerations, while the second loop (dark blue) is used to evaluate the best acceleration based on cost considerations over multiple time-steps.

Let's explore the two methods applicable to implement the first loop.

The first method leverages the Golden Section Search Method (GSM)². It is referred to a numerical optimization algorithm used to find the minimum of a unimodal function within a specified interval. For this application a 1-Dimensional approach is sufficient because it operates on a cost function driven by a single control variable. This method works by iteratively narrowing down the search interval (initialize by two arbitrary acceleration values considered as extreme bounds) while maintaining two interior points, often denoted as x_1 and x_2 , that subdivide the interval into two subintervals with the "golden ratio" proportion. At each step, it evaluates the cost function at two interior points and updates the interval based on the function values. The process continues until a predefined convergence criterion is met, such as a specified tolerance or a maximum number of iterations. This method is a very efficient way to find the minimum of a function without recurring on analytical calculations (impractical in some conditions) reducing the iteration number. However, it assumes the cost function to be strictly convex to find the global minimum, which is not feasible for our model considering the cost function we will illustrate later. Even if the model were capable of functioning with this method, it would yield a suboptimal solution. As a result, the outcomes would be significantly influenced by the driving conditions, making it impractical to create a model that can operate effectively in all conceivable driving scenarios, as we desire. Consequently, an alternative approach is presented.

The second approach rely on a for loop where all the possible acceleration are tested one at a time and the best one is chosen. In this case, the computational cost and the results depends

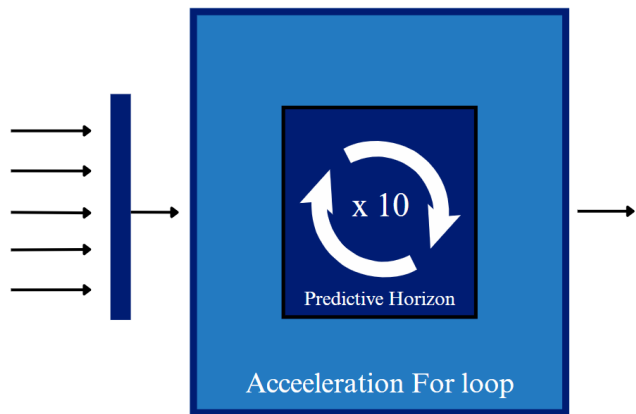


Figure 30: MPC iteration blocks

² GMS definition has been extracted from [26] and contextualized to the project purpose.

significantly on the number of accelerations tested and the discretization of the vector containing these values. With this method, we can be certain of finding the optimal solution, regardless of the shape of the cost function, but within the tested values. Consequently, if the global optimal solution lies outside this tested range, it will never be found.

In order to find a compromise between computational cost and accuracy of the results in almost all the scenario, the following approach has been implemented (this is what the light blue block does in figure 30):

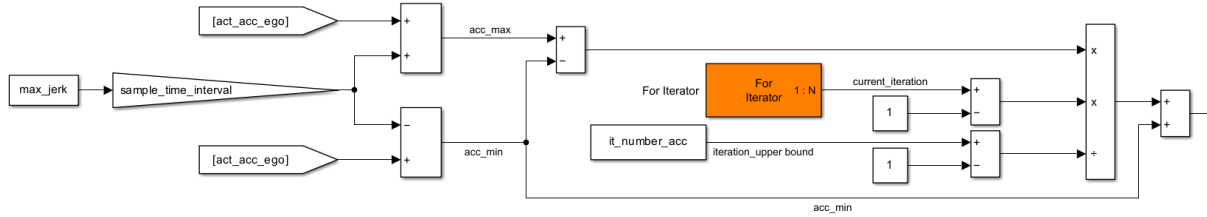


Figure 31: For iteration strategy

Observing the figure, it's evident that the for loop doesn't merely provide the acceleration value as input for the subsequent for loop. Instead, it employs a more complex architecture. Knowing the feasibility limit of the vehicle, in order to impose the one related to the Jerk ($\frac{dacc}{dt}$), and at the same time reduce as much as possible number of iterations, a linear relation has been exploited:

$$acc_{test} = acc_{min} + \frac{(acc_{max} - acc_{min}) \cdot (iter_{actual} - iter_{min})}{iter_{max} - iter_{min}} \quad (XVIII)$$

In the equation acc_{max} and acc_{min} are the upper and lower bounds chosen based on the imposed $Jerk_{max}$ limit:

$$acc_{max}(t + 1) = acc_{ego}(t) + Jerk_{max} \cdot \Delta t \quad (XIX)$$

$$acc_{min}(t + 1) = acc_{ego}(t) - Jerk_{max} \cdot \Delta t \quad (XX)$$

This relation ensures that was tested only accelerations within a feasible range of the current ego acceleration, thereby reducing the number of accelerations tested, enforcing feasibility limits, and enhancing comfort by limiting Jerk values. Anyway, this range of acceleration cannot be too narrow as it could impaired the following capability of the vehicle, making the simulation diverge. Once $Jerk_{max}$ is determined, we can calculate the maximum range of acceleration variation within one time-step. With these boundaries in place, we can determine the number of tested accelerations for each time-step, using a discretization of 0.05 m/s². For

instance, with $\text{Jerk}_{\max} = 2$, the acceleration variation from the current value in one time step (sample time = 0.1) is $\Delta_{\text{acc}} = \pm \text{Jerk}_{\max} \cdot \Delta t = 0.2$. Considering a discretization of 0.05, this results in 9 iterations. This value is incorporated into Equation XVIII as iter_{\max} . The variable iter_{\min} is set to 1 (conventionally starting iterations from 1). By using the current iteration number provided by the for-iterator block, we can test all accelerations within the defined discretization interval, from acc_{\min} to acc_{\max} .

3.PREDICTION PHASE

With the test acceleration defined, it must be applied to the model for a number of time-steps equal to the Predictive Horizon (PH). To execute this step, we enter the dark blue block of Figure 30. To simulate multiple time-steps within a pre-existing for loop, we've implemented another iteration block:

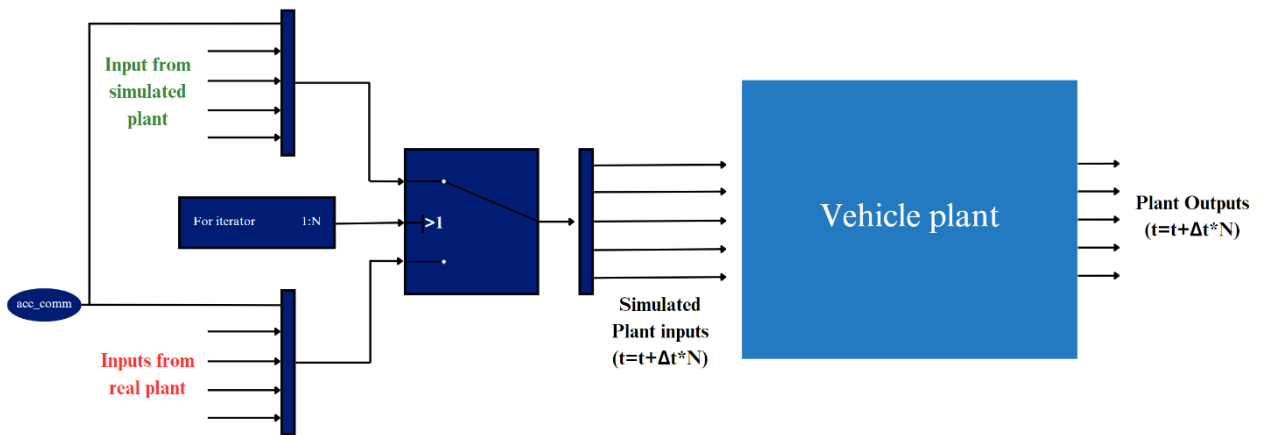


Figure 32: Prediction model implementation

This iteration is essential for predicting multiple local time-steps within a single real time-step, creating a data flow as if a closed loop is running multiple times. The for iterator block in the figure ranges from 1 to N, with N representing the PH. The simulation flow unfolds as follows:

1. Inputs from real plant model, explained in previous point, enters this section through the lower inputs in red, together with the constant acceleration command from the for loop mentioned in above described part.
2. For the first local time-step ($N = 1$) the switch selects the inputs coming from lower part and feeds them into the vehicle plant as input simulating the vehicle's evolution, starting from these inputs, and using the commanded acceleration.

3. The new states of the vehicle at the end of the first local time-step are passed to a block that accumulates the cost for this step and stores it in a 'memory block.'
4. For the subsequent local time-steps, the input selection changes. Instead of the lower input in red, the upper input in green is chosen. These values are retrieved from the memory block, simulating a regular evolution over multiple time-steps.
5. This process repeats, with the selection of green input values being updated for each subsequent local time-step. It is important to notice the acceleration command, kept constant for all PH simulation.
6. At the end of the predictive horizon, the overall cost function, derived from the sum of contributions from each step, is evaluated. Additionally, a feasibility check is performed, as explained in the next section. At this point, the for iterator block is completed, and the for iterator loop is reset to 1. It then proceeds to test the new acceleration from the outer acceleration for loop for the entire Predictive Horizon, re-evaluating the cost function and repeating the process until all accelerations have been simulated.
7. Once all accelerations have been tested, the one providing the best cost function without causing any infeasibility is commanded to the real vehicle model for CH time-steps.

4. COST FUNCTION

In Model Predictive Control (MPC), the cost function, denoted as J , is a mathematical function that assesses the cumulative performance of control inputs and system states over a finite prediction horizon N . It is formulated as the sum of individual cost terms, as shown below:

$$J = \sum_{k=1}^N L(x_k, u_k) \quad (\text{XXI})$$

- k is the time index, ranging from 1 to N , representing the prediction horizon.
- N is the prediction horizon PH.
- x_k is the state of the system at time step k .
- u_k is the control input at time step k .
- $L(x_k, u_k)$ is the state cost function, which quantifies how desirable or undesirable a particular state and control input are at each time step k .

The primary goal of MPC is to determine the optimal control input u^* (in this case acceleration), that minimize the total cost J , while satisfying system dynamics and input/output constraints.

$$u^* = \operatorname{argmin}(J) \quad (\text{XXII})$$

Subjected to:

$$x_{k+1} = f(x_k, u_k) \quad (\text{XXIII})$$

Which indicates the future state x_{k+1} as a function of actual state x_k and actual input u_k . In this case, the states variables x_k we are going to consider are:

- Leading vehicle speed ($\dot{x}_{leading}$)
- Leading vehicle positions ($x_{leading}$)
- Ego vehicle speed (\dot{x}_{ego})
- Vehicle position (x_{ego})
- Ego SOC (SOC_{ego})

On the other hand, the single control action u_k we are going to consider is the commanded acceleration ($acc_{command}$).

The choice of cost function terms, their weights, and the prediction horizon are crucial design parameters in MPC, allowing engineers to customize the control strategy to meet specific performance and constraint objectives for complex dynamic systems.

For this specific application in order to full fill all the requirements in terms of following capability and energy management the following total cost has been designed:

$$J = \sum_{k=1}^N \left[\alpha \left(\frac{\Delta_{distance}}{\Delta_{d_max}} \right)^2 + \beta \left(\frac{\Delta_{speed}}{\Delta_{v_max}} \right)^2 + (1 - \alpha - \beta) \left(\frac{-\Delta_{soc}}{\Delta_{soc_max}} \right) \right] \quad (\text{XXIV})$$

Within this cost function, three main contributions are highlighted allowing to control respectively:

- $\Delta_{distance}$ permit to keep the vehicle in the desired range of distance between max and min value, accounting for the distance error at the future time step. The α factor allows us to adjust the weight assigned to the desired distance constraints. Δ_{d_max} is the maximum distance allowed, normalizing the distance term to ensure all factors in the equation fall within the same range of values (0 - 1). The square value has been chosen taking inspiration from [27] where a cost function for a cooperative adaptive cruise control strategy optimization for EV base with MPC has been implemented. This square term allows to consider detrimental both positive and negative deviations. The most important variable in this factor is presented in the following formulation inspired by CTG approach:

$$\Delta_{distance} = [(x_{ego} - x_{leading}) - (h_{ego} \dot{x}_{ego} + s_{ego_0})]^{k+1} \quad (XXV)$$

The first difference represents the vehicle distance at the next step, enforces the ideal distance according to the vehicle's speed. Here, S_{ego_0} represent the desired distance when both vehicles are stationary.

- Δ_{speed} represents the speed difference between the ego and leading speed in future time steps. This component allows the ego vehicle to more or less strictly adhere to an imposed vehicle speed profile. Similar to the $\Delta_{distance}$ term, a normalization process is applied to accommodate the maximum speed variation we impose between the two vehicles. The square term is introduced for the same reason as in the previous case, and β represents the weighting factor.

$$\Delta_{speed} = (\dot{x}_{ego} - \dot{x}_{leading})^{k+1} \quad (XXVI)$$

- Δ_{SOC} term represent the difference between the ego SOC (State of Charge) at the next step and the current step.

$$\Delta_{SOC} = (SOC^{k+1} - SOC^k) \quad (XXVII)$$

The weighting factor for this term is denoted by $(1 - \alpha - \beta)$ to ensure that the sum of all three weights equals 1. Increasing the weight of a factor effectively adds more cost to it, making variations in that factor result in larger costs. Consequently, the controller responds by reducing control effort on the other factors, allowing them to oscillate more around their desired values. The term Δ_{SOC_max} , serves as normalization factor, ensuring that this factor remains within the 0 to 1 range, similar to the other two cases. To determine its value, a test was conducted to assess its maximum value during a WLTC, and it was then adjusted to align with the order of variation seen in the other two factors.

Unlike the other two components, the SOC factor is not squared because its negative effect should be considered only when the SOC decreases, consequently not in both directions. Therefore, a minus sign is incorporated into the function to assign a higher cost to actions that cause larger negative variations in SOC.

A critical aspect to consider in doing so, is that Δ_{SOC} can have both positive and negative values. During braking, when the SOC-related factor is negative, there is a significant advantage in applying negative acceleration. However, this creates

problems during acceleration phases, especially when the distance and speed factors are not strongly influential. In such cases, the controller may favour negative acceleration even if the leading vehicle is still accelerating. This leads to a local improvement, but as soon as negative acceleration is applied, the distance and speed factors rapidly increase since deceleration occurs while the leading vehicle is accelerating. Consequently, the ego vehicle controller is compelled to command a significant acceleration to recover the gap lost from the leading vehicle, resulting in detrimental effects on energy consumption and battery health.

To mitigate this oscillating effect, a dynamic weight is applied to the SOC factor. This weight is set equal to $(1 - \alpha - \beta)$ when positive accelerations are tested and zero when negative acceleration are tested. This allows negative acceleration to be imposed when the leading vehicle is decelerating or when the vehicles are too close to each other, providing an advantage in applying negative acceleration. This approach optimizes energy consumption during acceleration phases acting also on distance and speed and focus only on distance/speed error during braking manoeuvres where no energy optimization is needed just exploiting as much as possible regenerative braking.

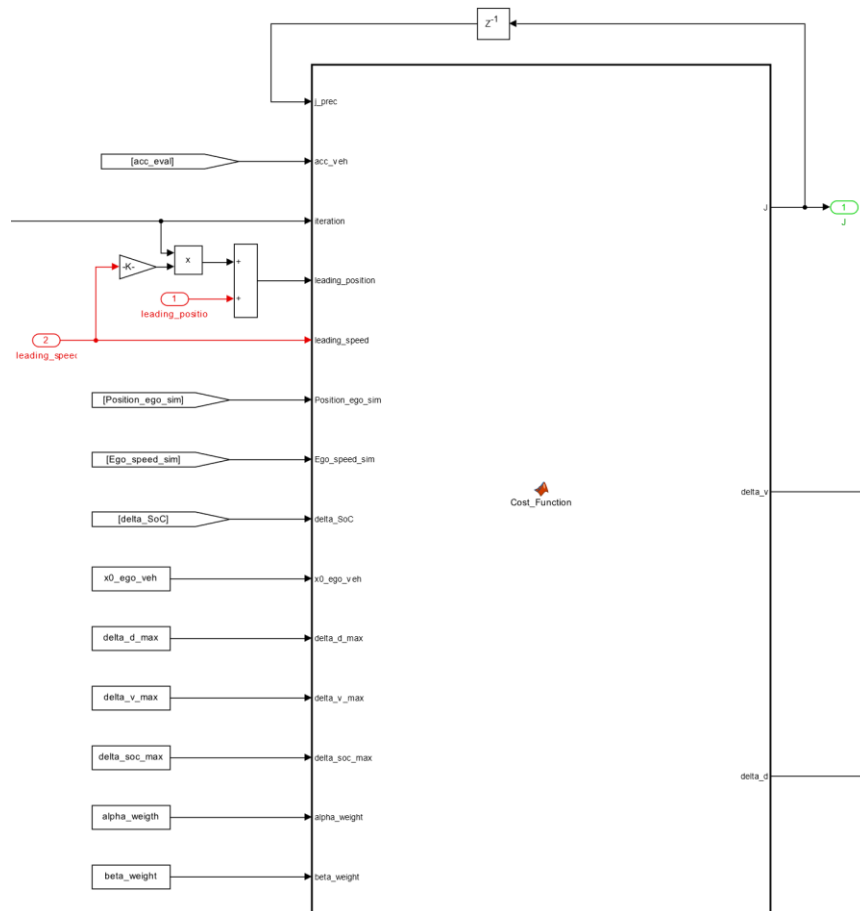


Figure 33: Cost Function Simulink® Block

The block within the previous figure contains the relationships previously outlined for computing the total cost over the entire prediction horizon (PH). The first input represents the value of the cost function evaluated at the previous time step. This value is then summed with the current cost evaluated for each step (k-step), resulting in the total cost of function XXIV. It is important that at the end of the predictive horizon the J_{prec} value is reset to zero in order to perform another prediction using a different acceleration. In the following will be shown the Matlab® script for the cost function evaluation.

```

1  function [J,delta_v,delta_d] = Cost_Function()
2
3  d_des = Ego_speed_sim*2.7+abs(x0_ego_veh); %Safe distance according to vehicle speed
4  d_act = leading_position-Position_ego_sim; %Distance between the two vehicles
5  delta_d = d_act-d_des; %Distance error
6  delta_v = leading_speed-Ego_speed_sim; %Velocity Difference between the two vehicles
7
8  j_track = (delta_d/delta_d_max)^2;
9  j_speed = (delta_v/delta_v_max)^2;
10 j_consumption = abs(delta_SoC/delta_soc_max);
11
12 if acc_veh < 0
13     gamma = 0;
14 else
15     gamma = 1-alpha_weight-beta_weight;
16 end
17
18 if iteration == 1
19     J_prec = 0;
20 else
21     J_prec = j_prec;
22 end
23
24 J = J_prec + alpha_weight*j_speed + beta_weight*j_track+ gamma*j_consumption;
```

Figure 34: Cost Function Matlab® Script

Additionally, it's essential to consider the leading vehicle's speed and position. As assumed earlier in the analysis, the leading vehicle's speed remains constant throughout the prediction horizon. Consequently, this input is kept constant as soon as it enters the for-iterator loop. As a result, the leading vehicle's position entering the cost function is updated using the following straightforward relation:

$$x_{\text{Leading}}^{t+N} = x_{\text{Leading}}^t + N \cdot \dot{x}_{\text{leading}}^t \cdot \Delta t \quad (\text{XXVIII})$$

This equation calculates the position along the prediction horizon by summing the leading vehicle's position at the instant when the prediction phase begins with the product of the constant vehicle velocity and the sample time interval, indicating the distance covered in one sample time at that speed, multiplied by N, which represents the iteration number within the

prediction horizon. This ensures that the leading position increases as the prediction time progresses.

All the remaining inputs are the updated ego vehicle states and constants necessary for cost evaluation. The output of the cost function is the total cost J at the end of the PH, along with $\Delta_{distance}$ and Δ_{speed} , which will be used for feasibility check for next step.

The weight parameters were selected to prioritize energy consumption significantly while assigning relatively lower importance to speed and distance factors. This allocation permits more extensive variations in speed and distance from the nominal values, promoting smoother velocity profiles, while still ensuring adequate following capability. Specifically, α was configured to a value of 0.15, and β was set to 0.05 for these reasons.

5.UNFEASIBILITIES CHECK

Once the total cost has been evaluated for all prediction horizons (PH) for a single control variable, an additional check is imperative to ensure the action leads to feasible conditions. The following constraints have been imposed:

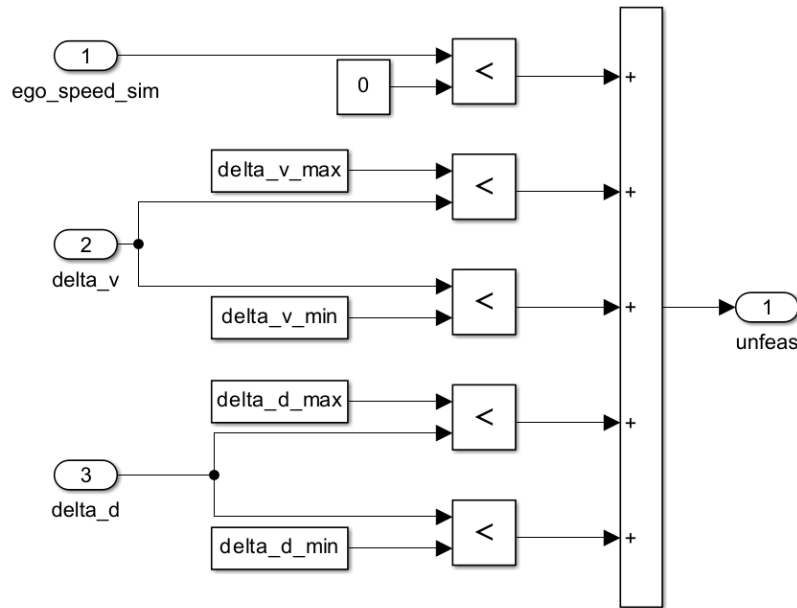


Figure 35: Feasibility check

- $\Delta_{d_{min}} < \Delta_{distance} < \Delta_{d_{max}}$
- $\Delta_{v_{min}} < \Delta_{speed} < \Delta_{v_{max}}$
- $v_{ego} \geq 0$

Here $\Delta_{d_{max}}$ is set to 20 m, $\Delta_{d_{min}}$ at 0 m, $\Delta_{v_{max}}$ at 10 m/s and $\Delta_{v_{min}}$ at -10 m/s. These values indicate that we want our vehicle to operate at a distance bounded within the safety

distance ($\Delta d_{min} = 0 \text{ m}$) and 20 m far from this to ensure following vehicle capability and sufficient traffic flow rate. Speed has also been bounded in that range to prevent excessive speed difference that could lead to dangerous situations or impossible following capability.

It's worth noting that Jerk control has been intentionally excluded from this check. As explained in STEP 2, the accelerations tested are selected based on the maximum jerk value, starting from the current acceleration, creating a form of self-control on jerk beforehand.

The check is performed using relational operators, which output 1 if infeasibility is detected or 0 otherwise. Once all the checks are completed, the sum of these results is sent to the next block to determine the best acceleration to command.

6. MINIMUM COST ACCELERATION

The figure below shows the architecture used for finding the minimum cost acceleration for the entire PH.

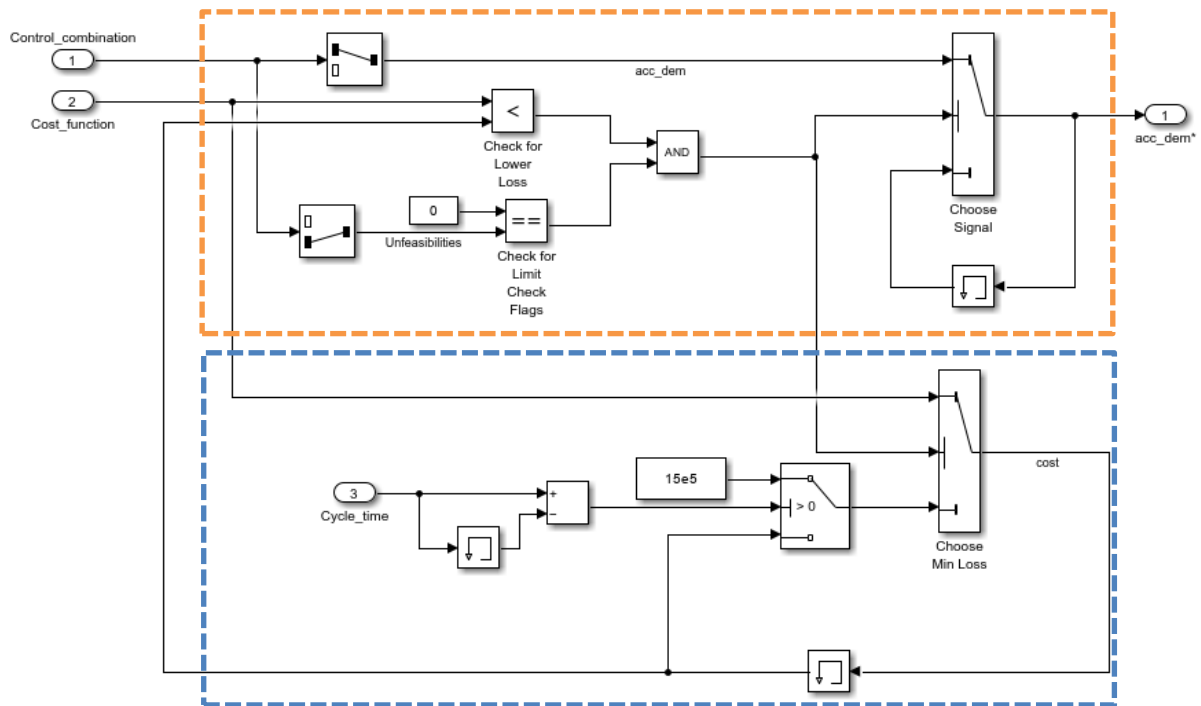


Figure 36: Minimum cost acceleration search

In the orange segment, the system extracts the best acceleration based on the best-cost action stored by the blue block. The flow of this system operates as follows:

1. The commanded acceleration enters the control combination input, which consists of two variables: the commanded acceleration and the unfeasibility variable. The cost function related to the acceleration enters Input 2.

2. The cost function is compared using a relational operator with the best cost function found up to that moment by blue block.
3. If the cycle time (which is kept constant for all prediction horizons, as it is the real global simulation time) differs from previous cycle time, it signifies the start of a new predictive horizon. Consequently, an initial cost value is set equal to $15e5$, which is compared with the first value entering the block as input. Within the prediction horizon, the cycle time remains equal to the previous one. Therefore, the value considered as a reference is the one stored in memory after exiting the cost selector.
4. The blue block selects whether to use the previously stored value or the new one based on input from the orange block. The orange block compares if the cost function evaluated for the currently tested control action is lower than the best previously evaluated cost AND if the unfeasibility variable is equal to zero. If these conditions are met, the output will be 1, the new best cost will be this one, and the new acceleration will be sent as output and stored in the memory block.
5. This iterative procedure is performed for all accelerations for the entire prediction horizon by the iterator block, which provides the best acceleration as output, stored in the memory block.

By following this process, if an infeasibility is detected by the previously examined block, the input variable will differ from zero, and consequently, the acceleration will be discarded, preventing the vehicle from entering an unfeasible condition.

7.UPDATE EGO REAL PLANT

According to the implemented architecture, the number of control accelerations commanded during a single prediction horizon can be larger than one. For the sake of simplicity in this explanation, a scenario with a single constant acceleration is considered. Once the best acceleration is chosen, it exits the MPC controller block, as shown in Figure 29, and is sent to the Ego plant driver to be executed by the real vehicle. The vehicle states evolve and are returned as input to the MPC block, which then recommences from Step 2.

4.5.2. NMPC Test

Using the previously illustrated architecture, numerous tests were conducted to determine the optimal combination of prediction horizon (PH), control horizon (CH), the number of iterations,

and computational cost. The conducted analyses are listed below, with the most significant results presented to highlight the advantages and disadvantages of each tested simulation:

-NMPC with PH = 2, CH = 1 - single constant acceleration for the whole PH:

This is the simplest MPC architecture that can be implemented, as it differentiates from punctual optimization strategies by having a PH greater than one. In this application, a prediction is made over two time-steps, and control is applied to the next single time step. Despite its simplicity, this strategy, with its very small prediction horizon, tends to converge towards a local solution. It optimizes each individual step without sufficiently considering more distant vehicle states. Examining some results reveals that the commanded acceleration exhibits significant oscillations. Since acceleration is closely linked to power request, having high values and large oscillations is detrimental to State of Charge (SOC) and State of Health (SOH). Nonetheless, in this case, peak values are smaller, resulting in small improvements.

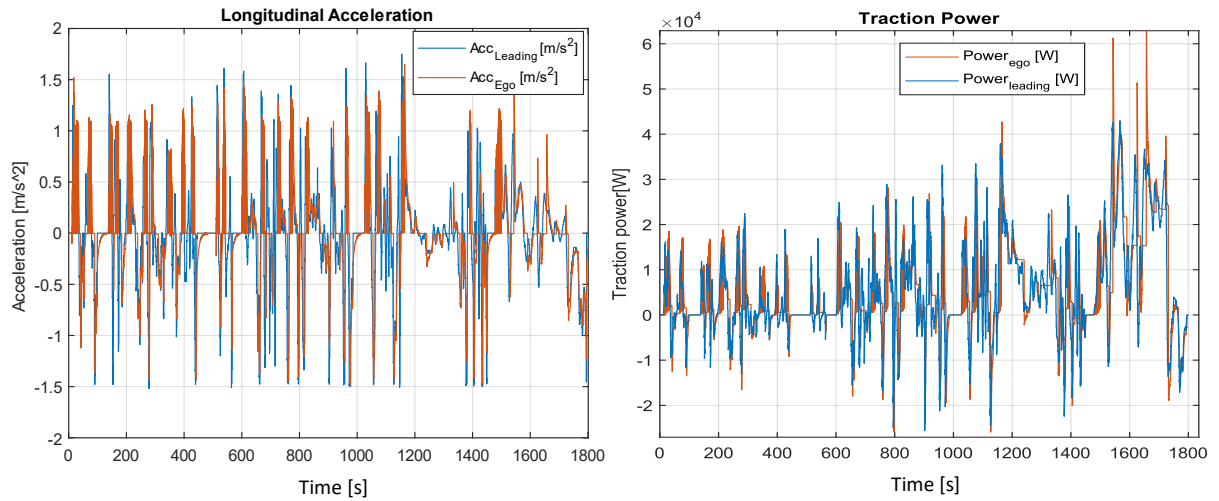


Figure 37: Longitudinal acceleration and Traction Power Plot NMPC PH = 2, CH = 1

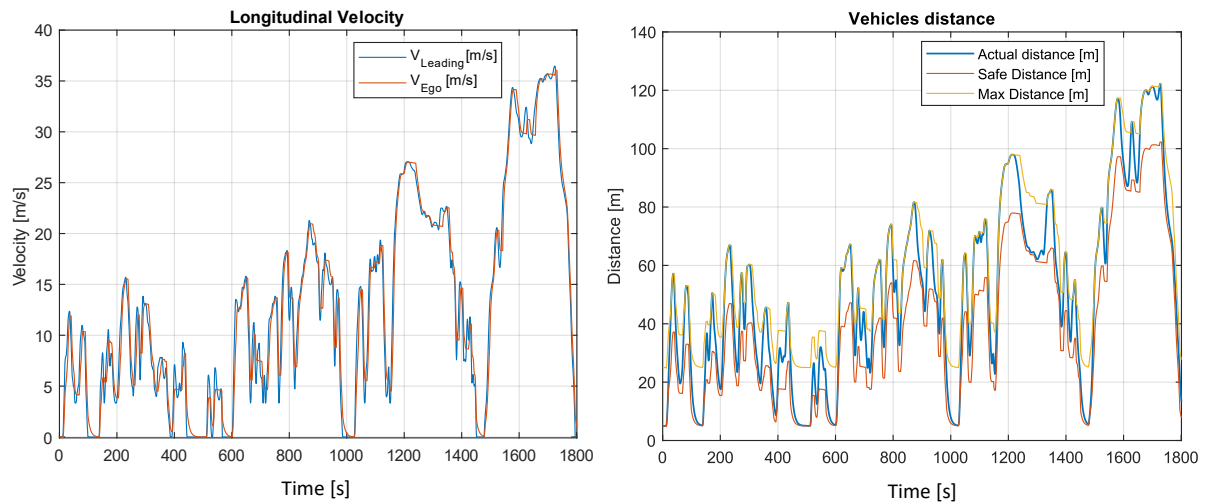


Figure 38: Longitudinal Velocity and Vehicle Distance Plot NMPC PH = 2, CH = 1

These results are depicted for a WLTC, where a more aggressive command clearly highlights the limitations of this control. However, all these tests have also been repeated for the EPA cycle to assess the model's robustness and adaptability to different scenarios.

The most intriguing results can be observed by examining the speed profile and vehicle distance plots. In the speed profile, one can discern an initial hint of smoothing, where most speed peaks are reduced in both acceleration and deceleration phases. This smoothing effect is possible due to the soft constraint on distance, which allows for larger variations. During deceleration, the smoother action is achieved thanks to the distance constraint, which prevents the speed from rapidly reaching zero to approach the desired distance when the vehicle is stationary. This allows for a gradual reduction in speed until reaching a distance of 5 meters.

Analysing the vehicle distance plot on the right reveals a difference from the Constant Time Gap (CTG) approach. In this case, the controller doesn't rigidly maintain a safe distance but rather oscillates, allowing the distance to vary according to current conditions while striving to minimize the total cost function. As expected, these oscillations are bounded within maximum (yellow curve) and minimum (red curve) limits. During this simulation, despite some noise in trends for the explained reasons, the SOC improves by 2.91%, and the SOH improves by 7.8%. Remarkably, even though the cost function does not explicitly aim to minimize SOH, the reduction in peak power requests indirectly benefits battery SOH. Additionally, other important statistical data show reductions, such as a 4% decrease in maximum acceleration and an 8% reduction in maximum Jerk value due to the imposed constraints. These advantages have been achieved while maintaining the time required to complete the overall cycle, with a difference of only 6.5 seconds over a 30 minutes trip. To achieve a more realistic and applicable control strategy with fewer oscillations, further tests were conducted by increasing the PH to find the optimal compromise between computational cost, low oscillations, and improvements.

-NMPC with PH = 10, CH = 1 - single constant acceleration for the whole PH:

After conducting various tests, we identified the best compromise with this configuration. In this case, the prediction horizon is sufficiently large to ensure a smoother profile without an excessively long horizon, which would lead to incorrect predictions. This is particularly problematic when considering the assumption of constant Leading vehicle speed, especially when transitioning from braking to accelerating and vice versa, causing overshoot in ego vehicle actions.

The results presented here are based on simulations using the WLTC since it is a more aggressive cycle compared to the EPA cycle, making improvements more evident. In this case,

the acceleration command exhibits significantly less oscillation, with considerable reductions in all peaks. Approaching zero speed, a smoother profile (for the same reasons explained earlier) is achieved, indicating a substantial reduction in power request. Furthermore, in terms of comfort, jerk values are greatly reduced in all conditions, more than halved, indicating that the controller operates more effectively and smoothly.

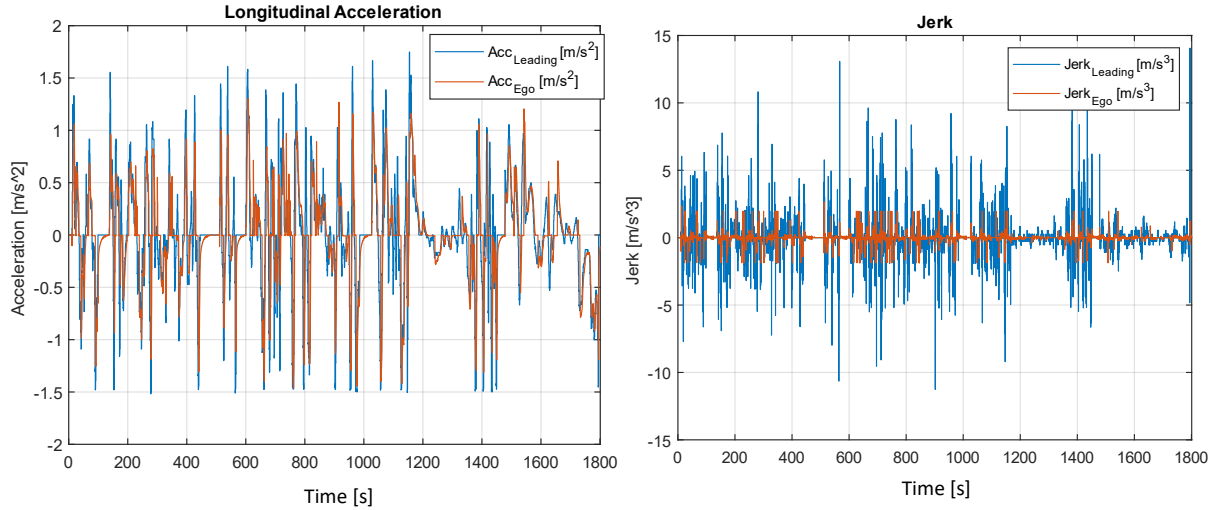


Figure 39: Longitudinal acceleration and Jerk Plot NMPC PH = 10, CH = 1

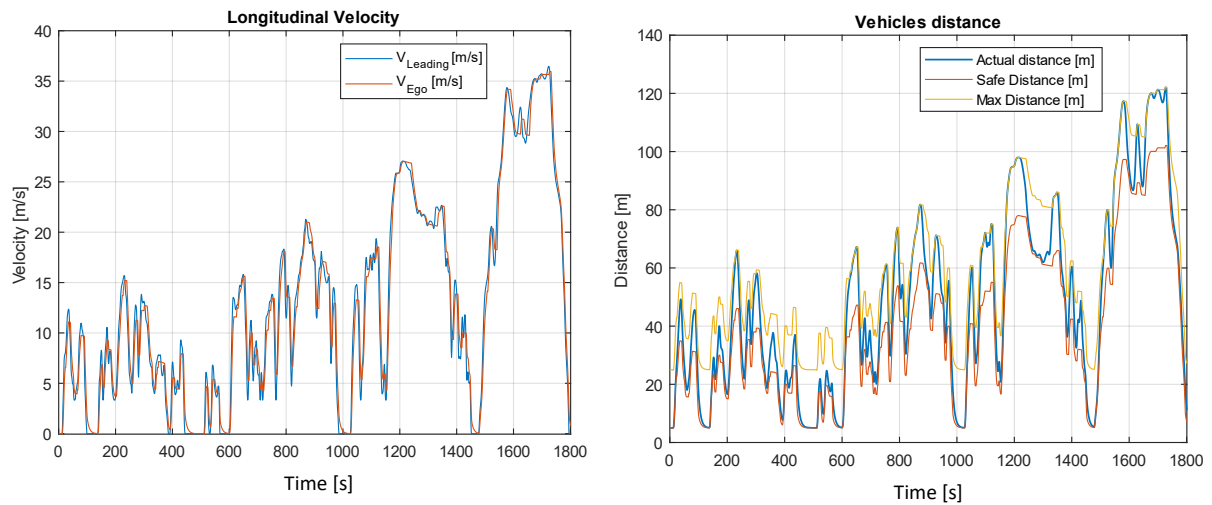


Figure 40: Longitudinal speed and Vehicle distance Plot NMPC PH = 10, CH = 1

Now, let's focus on the two most important results. Examining the velocity profile, it's evident that the initial objective, set at the beginning, has been successfully achieved. The ego vehicle (in red), predicting future vehicle behaviour, optimizes its trajectory, smooths its speed profile, and avoids oscillations in the behaviour of the leading vehicle. All speed peaks are diminished, and the vehicle approaches zero speed more smoothly, sometimes even avoiding stops when the leading vehicle comes to a halt. In many instances, the leading vehicle experiences rapid positive and negative speed changes, but our ego vehicle effectively smooths them out,

exhibiting nearly linear behaviour. Moreover, the distance is expertly managed, varying as much as needed within the desired interval without ever falling below the safety distance or exceeding the maximum limit. However, it's essential to acknowledge the limitations of this configuration. For instance, in some peak speed conditions, the ego vehicle exhibits a slight delay in speed reduction compared to the leading vehicle. This limitation arises from assuming constant leading vehicle speed throughout the entire prediction horizon. If in reality the leading vehicle's speed changes sign in the next steps, our predictions for that instant would be entirely inaccurate, causing this discrepancy observable in figure 40. Despite these limitations, the improvements achieved with this approach are more significant, with a 4.12% reduction in energy consumption and a 10.2% improvement in battery State of Health (SOH) for a single cycle. These values are primarily due to a 17% reduction in maximum acceleration, indicating a decrease in power demand. In terms of comfort, the 81% reduction in jerk peaks ensures a substantial improvement for passengers. These improvements are achieved while keeping travel time almost constant, with a difference of only 5 seconds for the same distance travelled.

These results confirm the anticipated benefits of leveraging leading vehicle information to predict future vehicle trajectories, smoothing profiles, and consequently improving energy consumption and indirectly enhancing battery life. However, it's important to consider another factor. To perform such extensive prediction, the computational cost becomes substantial for a passenger car's microprocessor, as it simulates the overall nonlinear model within the controller during simulations. Therefore, the next step is proposed to address this issue.

4.5.3 LMPC architecture

The previous architecture demonstrated the potential of leveraging leading vehicle information to enhance energy consumption and extend battery life. However, it also revealed limitations in terms of computational cost due to the complex model simulated within the plant. As a benchmark, NMPC was considered, from which simplifications could be made and compared against the ideal result. The primary challenge with the previous architecture, as explained, lies in the nonlinear model simulated within the controller. To address this, the following strategy was implemented to establish a linear relationship between vehicle states and control variable, significantly simplifying the simulation cost.

Several realistic assumptions were made to facilitate the linearization of the model:

- **Constant Cell actual max capacity during PH:** This assumption was made because, over ten time-steps (equivalent to 1 second), the cell's actual max capacity degrades by a factor of 10^{-7} .
- **Ego Plant's Ability to Replicate Driving Cycle:** It was assumed that the ego plant can precisely replicate the imposed driving cycle by the controller. This assumption enabled the evaluation of vehicle speed, position, and acceleration at the next time steps as function of the command input using linear relations:

$$\ddot{x}_{vehicle\ sim} = acc_{command} \quad (XXIX)$$

$$\dot{x}_{vehicle\ sim}^t = acc_{command} \cdot \Delta t + \dot{x}_{vehicle\ sim}^{t-1} \quad (XXX)$$

$$x_{vehicle\ sim}^t = x_{vehicle\ sim}^{t-1} + \dot{x}_{vehicle\ sim}^t \cdot \Delta t + \frac{1}{2} \cdot acc_{command} \Delta t^2 \quad (XXXI)$$

It has been possible to do that since the PI controller inside the ego vehicle driver provides a command which allows to exactly copy input request as shown in the following charts where the lines are overlapped, and no difference could be appreciate:

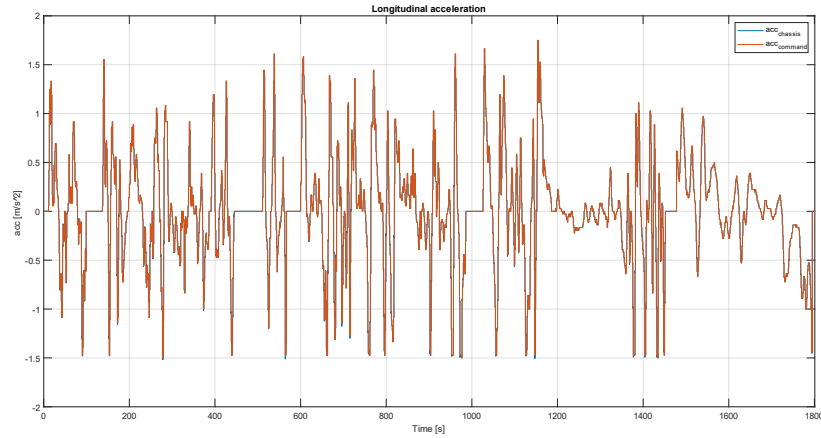


Figure 41: Commanded vs Chassis acceleration WLTC

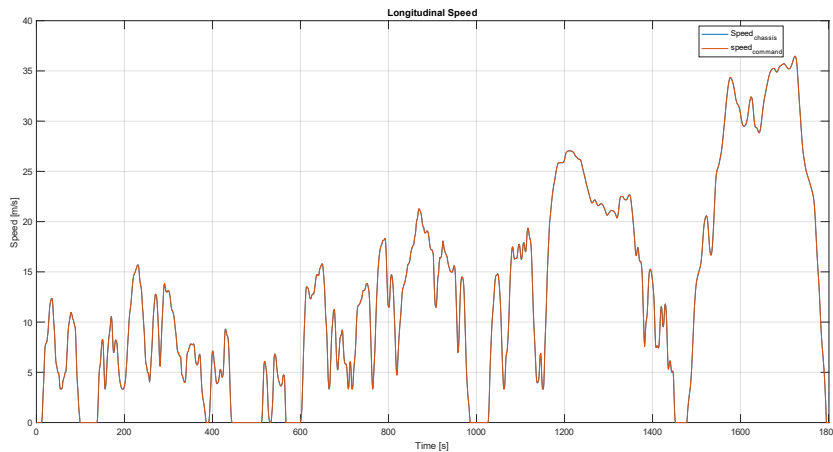


Figure 42 Commanded vs Chassis speed WLTC

- Linear relation between commanded acceleration and Ego battery SOC:** This characteristic was considered linear after specific tests. In particular, given that the effect of acceleration on State of Charge (SOC) within the cost function is significant only for positive accelerations (as the weight associated with the energy-related factor is set to zero in other cases), a series of tests were conducted focusing on various positive accelerations. To establish this linearity, a ramp signal ranging from 0 m/s^2 to 2 m/s^2 (covering most positive accelerations the vehicle can withstand) was used. This range of accelerations was tested on the real vehicle plant, revealing an almost linear relation between $\frac{\text{cell current}}{\text{vehicle speed}}$ and commanded acceleration. Given that cell current depends on both acceleration and current vehicle speed (due to different resistance forces at different speeds), considering this ratio allowed for the establishment of a linear relation with input acceleration. After an initial approximation using linear regression with Matlab® functions such as 'polyfit,' the following equation was derived: $y = 0.00112 + 0.2057 \cdot \text{acc}_{\text{command}}$.

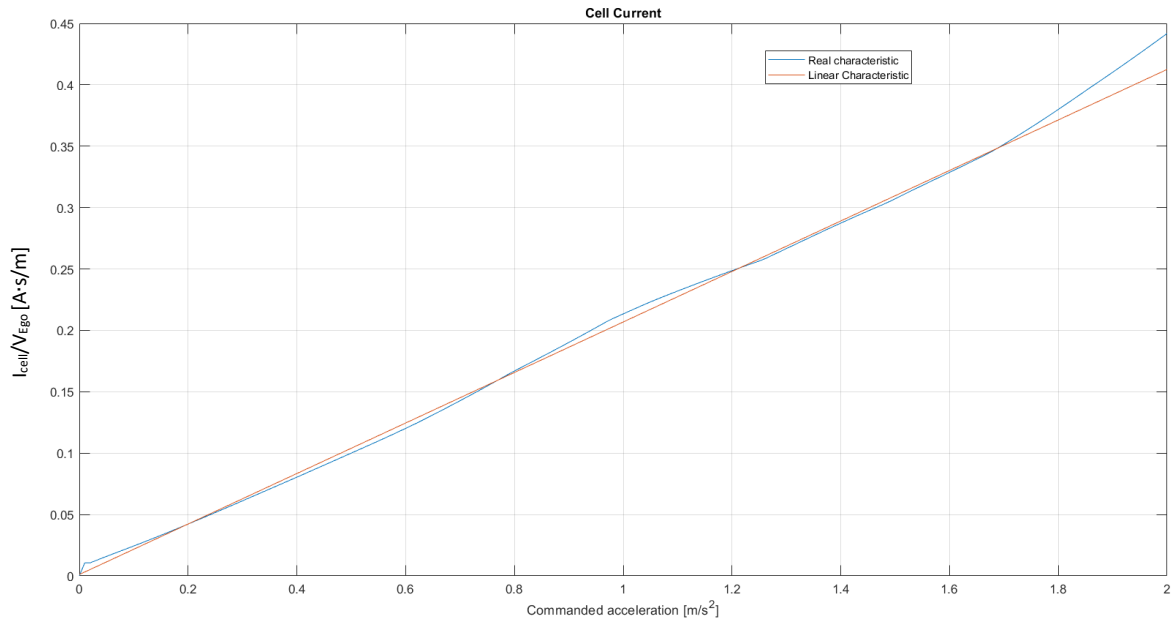


Figure 43: I/V linearized characteristic

The trends in the figures closely overlapped, particularly within the useful cell current range from 0 to 5 A for the WLTC request. This suggested that the linearization hypothesis and implementation were successful.

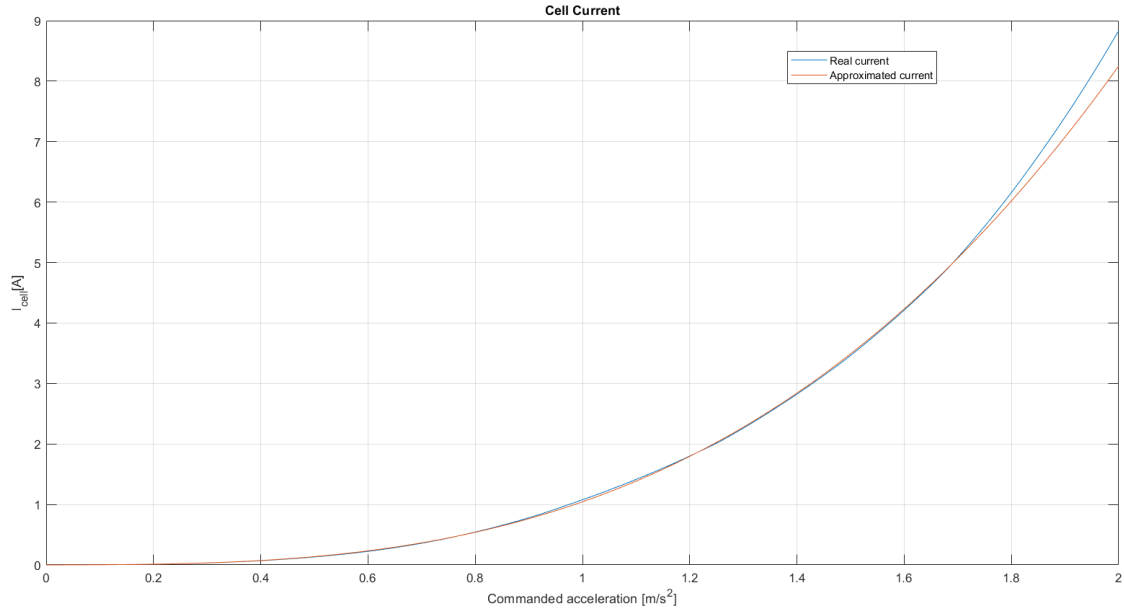


Figure 44: Cell current comparison

With the output cell current evaluated, the transition to State of Charge (SOC) follows linear relations:

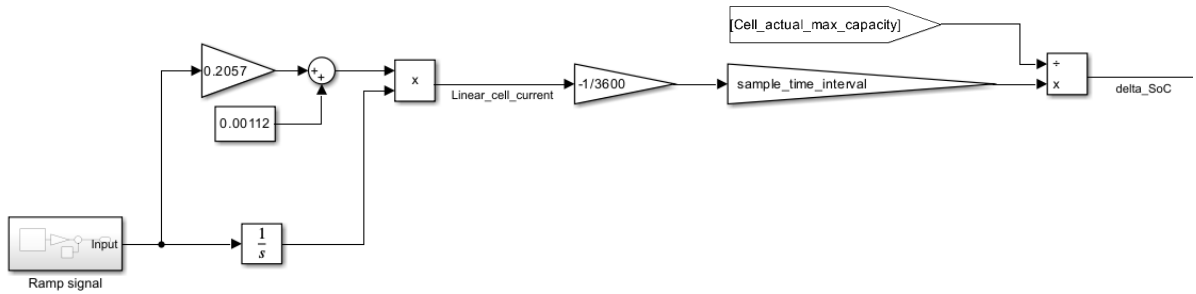


Figure 45: Linearized model

The change in SOC for a single time-step (Δt), i.e., the numerator of the energy-related factor within the cost function, can be calculated by multiplying the current by the sample time interval, dividing by 3600 to obtain Ampere-hour (Ah), and then dividing by the cell's actual max capacity.

$$\Delta_{SOC} = - \frac{I_{cell} \cdot \Delta t}{3600 \cdot C_{actual \max cell}} \quad (XXXII)$$

Now it becomes possible to comprehend the reasons behind the initial assumption of maintaining the Cell's actual maximum capacity as constant throughout the Prediction Horizon

(PH). In this simplified model, which lacks an estimation mechanism for battery State of Health (SOH), the actual maximum capacity of the cell is not updated at each local time-step. Instead, this update is deferred until the conclusion of the PH, once the control action is transmitted to the actual vehicle plant, and the vehicle's states evolve. Consequently, we opt for treating this value as a constant, albeit with infinitesimal error, when making predictions. With these assumptions, in line with those presented previously, the linearized model (as depicted in Figure 45) is now fully established. It is noteworthy that this linearized model substantially reduces the number of inputs required for the controller compared to its non-linear counterpart (as illustrated in Figure 46), thus significantly simplifying the model's complexity. This potentially allows testing on a real vehicle microprocessor to evaluate its real-time capabilities.

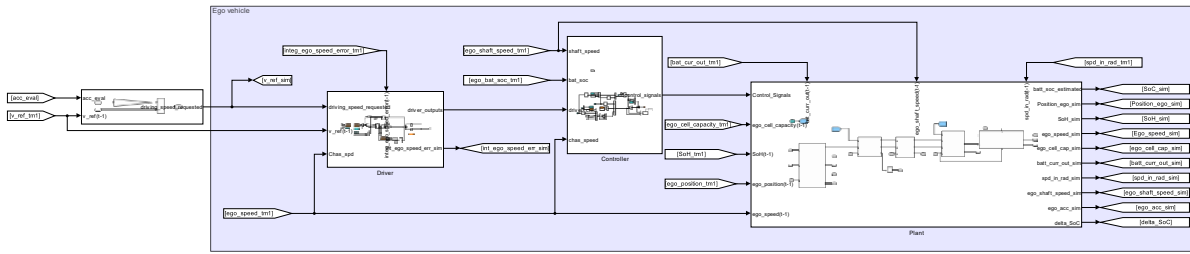


Figure 46: NMPC simulated model

Despite the linearized model, the overall scheme and steps required for prediction remain unchanged. Two main simulations were performed using the new linearized model, starting from the best configuration of NMPC tests:

- PH = 10, CH = 1 with constant acceleration along PH: This simulation aimed to evaluate the effectiveness of the linearized model compared to the benchmark solution, verifying if the model correctly predicts outcomes.
- PH = 10, CH = 2 with constant acceleration along PH and CH: This configuration aimed to reduce the number of iterations significantly and assess whether the computational cost reduction still preserves the improvements.

LMPC PH = 10, CH = 1 with constant acceleration along PH

Despite the linearized model closely mimic the realistic trend of the vehicle plant, it incorporates certain limits and simplifications that yield slightly different results. To quantify the performance reduction resulting from these simplifications, we repeated the same tests

conducted for NMPC under this configuration. Consequently, this simulation was executed for both the WLTC and EPA to assess the controller's robustness and flexibility.

This specific configuration keeps the same structure of NMPC with modification limited to the components related to figure 46, which are modified as follows:

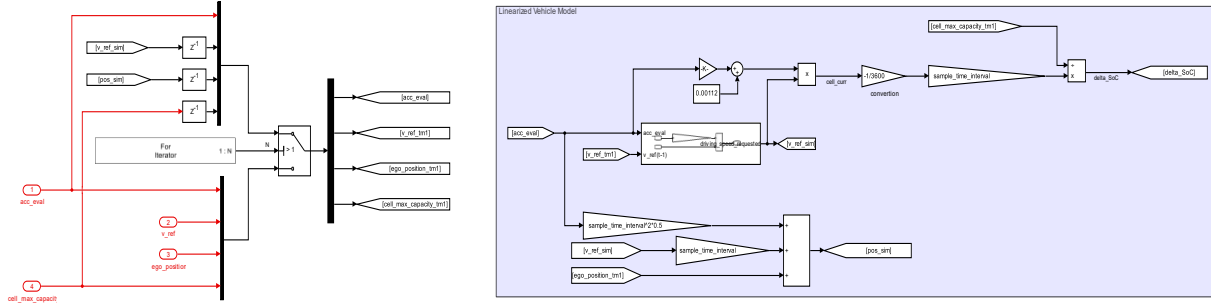


Figure 47: LMPC internal blocks structure

The number of inputs required is significantly reduced, employing expressions XXIX, XXX, XXXI, and utilizing a mechanism identical to that used in Figure 32. With this setup, the following results were obtained.

The plots in this case show similarities to those from NMPC, featuring some oscillations or larger peaks that, nevertheless, do not lead to unrealistic trends. Utilizing this model, the reductions in improved performance compared to the WLTC (following the leading vehicle) are noticeable, with a 7.84% decrease in SOC improvement and a 3.09% reduction in SOH improvement. However, this decrease is reasonable considering the simplifications and assumptions in the model, yet the resulting improvements in SOC and SOH compared to the WLTC remain substantial at 3.79% and 9.8%, respectively.

When examining the EPA cycle, the decrease is less pronounced, at 7.69% for SOC and 1.31% for SOH. This lesser impact is attributed to the less aggressive nature of the EPA cycle, which reduces the influence of different strategies and the resulting reduction.

LMPC PH = 10, CH = 2 with constant acceleration along PH and CH

After quantifying the performance reduction, we further analysed and reached the final configuration, which halves the number of iterations while maintaining high performance levels. This section presents all the results in comparison to both leading vehicle following under the WLTC or EPA and a current strategy implementable in real vehicles, Adaptive Cruise Control (CTG). This comparison helps us understand the improvement achieved by implementing this strategy in vehicles that already have a standard control architecture.

The solution achieved in this section involves implementing a Control Horizon (CH) greater than 1, specifically set to 2. It operates with constant acceleration during this period. This outcome follows multiple simulations that tested various CH lengths with constant acceleration to determine the best compromise. $CH = 2$ emerged as the optimal choice, as increasing this horizon led to controlling the vehicle in ways that deviated significantly from realism due to the assumption of constant Leading vehicle speed. To implement multiple controlled horizons with constant acceleration, the MPC block must be enabled not at each time-step, acting anyway on the plant also when the controller is turned off. This was made possible by utilizing the architecture shown below:

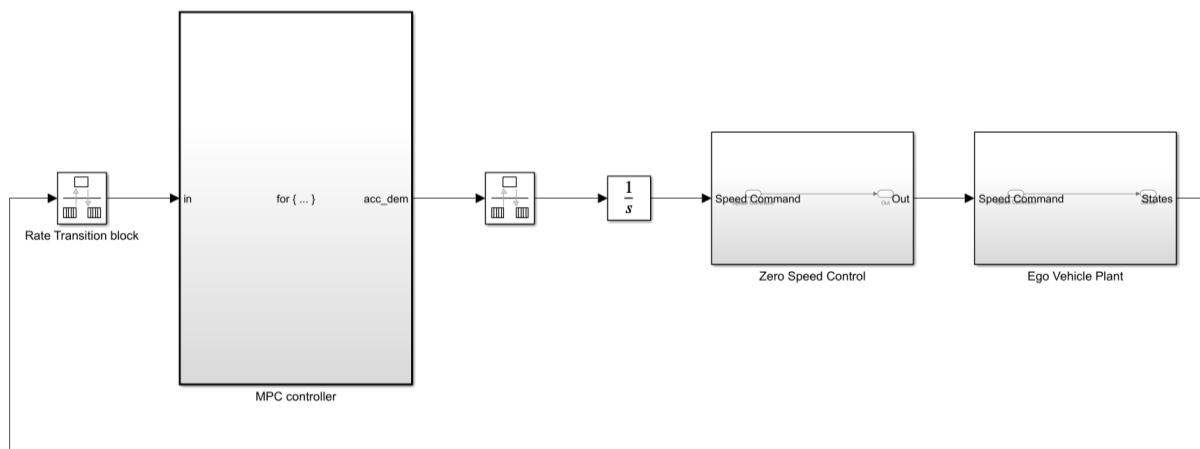


Figure 48: Multiple CH block scheme implementation

The largest block on the left is the MPC controller, responsible for determining the optimal acceleration command. To predict values every two time-steps and influence the plant accordingly in the subsequent two time-steps, a 'Rate Transmission' block has been incorporated. This block enables the adjustment of the sampling frequency of its output, thereby modifying the operational response of the subsequent blocks. Placing this block before the MPC controller and setting the output sampling frequency to half of the simulation frequency ensures that it produces results every two-simulation time-steps.

Once the results exit the MPC controller block, the rest of the Simulink model must revert to working with the normal sampling frequency. Therefore, another 'Rate Transmission' block with an output frequency equal to the simulation frequency has been introduced. Given that the input to this block is generated every two-simulation time-steps, the remaining time step it is kept constant equal to the last output value. This architecture allows predicting a single

commanded acceleration while acting on two time-steps, significantly reducing computational costs and enabling the spreading of MPC predictions over two time-steps.

With this alternative method, utilizing $\text{Jerk}_{\max}=4 \text{ m/s}^3$, a discretization of 0.1 for the acceleration loop, $\text{PH}=10$, and $\text{CH}=2$, the number of iterations required for each time-step is 45. Given the very simple linearized model employed, this setup could ensure real-time implementation on a passenger car microprocessor. Employing this alternative method, the following results were collected.

WLTC BASED SIMULATIONS

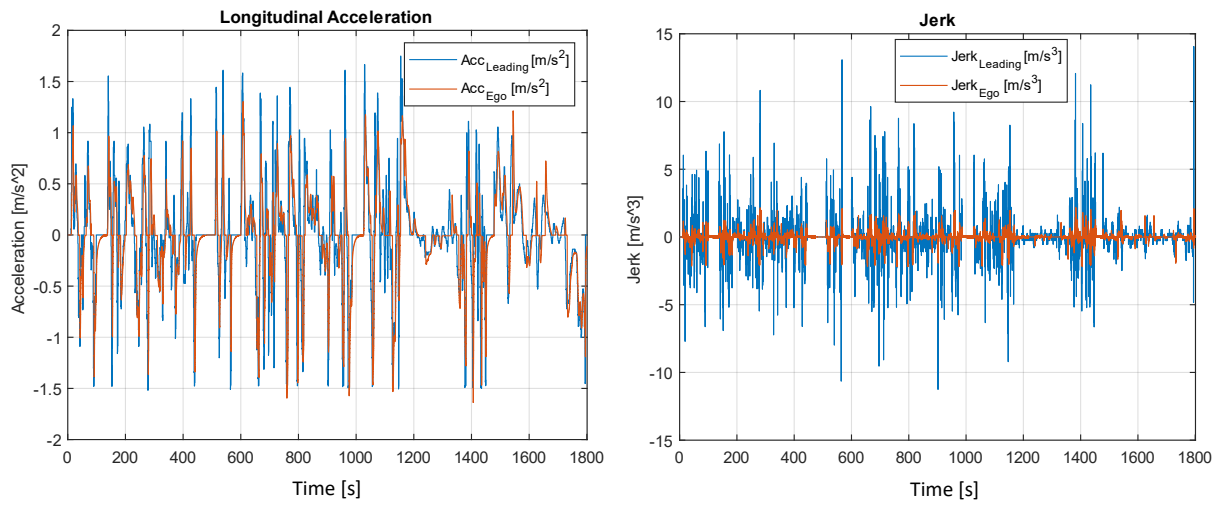


Figure 49: WLTC Longitudinal acceleration and Jerk Plots LMPC PH = 10, CH = 2

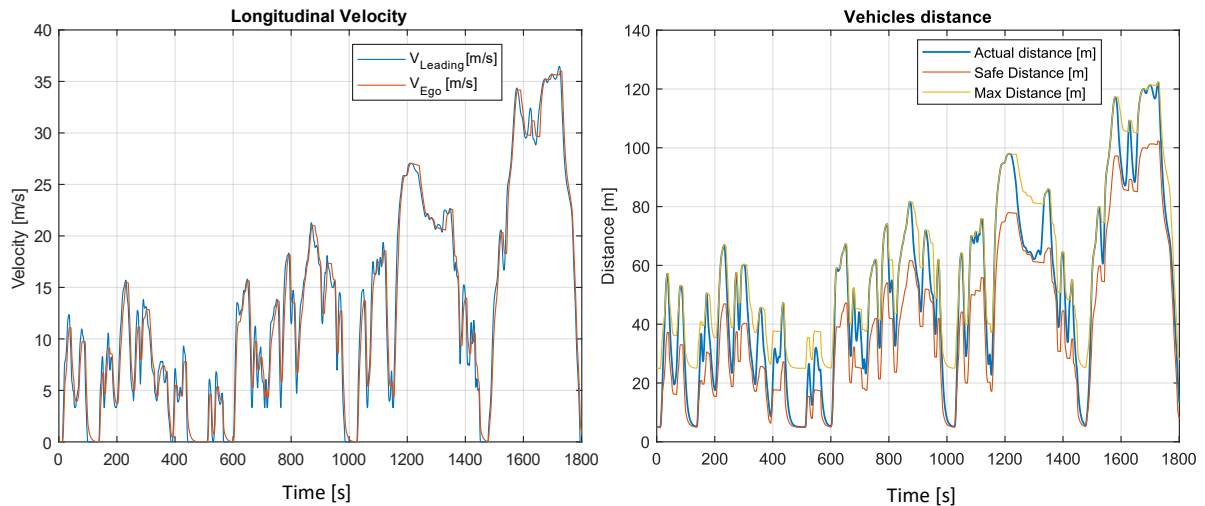


Figure 50: WLTC Longitudinal speed and Vehicle Distance Plots LMPC PH = 10, CH = 2

Upon examining these plots, it becomes evident that the results closely resemble those obtained for NMPC, even though in this case, the number of iterations is significantly reduced, and the

model complexity is simplified. In this case, the reduction in performance compared to NMPC is slightly higher but still within a small amount. The increase in energy consumption compared to the WLTC is also noticeable, with a 9.8% decrease for SOC improvement at the end of the cycle and a 4.7% decrease in battery degradation improvements. As expected, these results are less favourable compared to having $CH = 1$. Nevertheless, the residual improvement is still significant, with 3.71% and 9.7% improvements in SOC and SOH, respectively.

Examining the maximum acceleration values reveals a more substantial deterioration, approaching 60%, due to higher peak requests. However, this value still remains below the peak acceleration request by the leading vehicle by 6.5% (compared to the 17% observed in NMPC). In this case, the jerk value, resulting from imposing constant acceleration for two time-steps, experiences a smaller decrease in the jerk peak value, with a gain of 4.03%. Overall, the driving travel is completed in nearly the same time. Based on these results, this configuration has been selected as the definitive one, capable of enhancing vehicle energy consumption and battery life while keeping computational costs to a minimum.

RESULTS COMPARISON WITH CTG STRATEGY (WLTC)

Up to this point, the implemented strategy has been compared with the results from a leading vehicle that exactly replicates a driving cycle, benefiting from the aforementioned improvements. To gain a more comprehensive understanding, this section compares the optimization strategy's results with a simple CTG control strategy that does not leverage optimization or prediction, relying on a basic formulation instead.

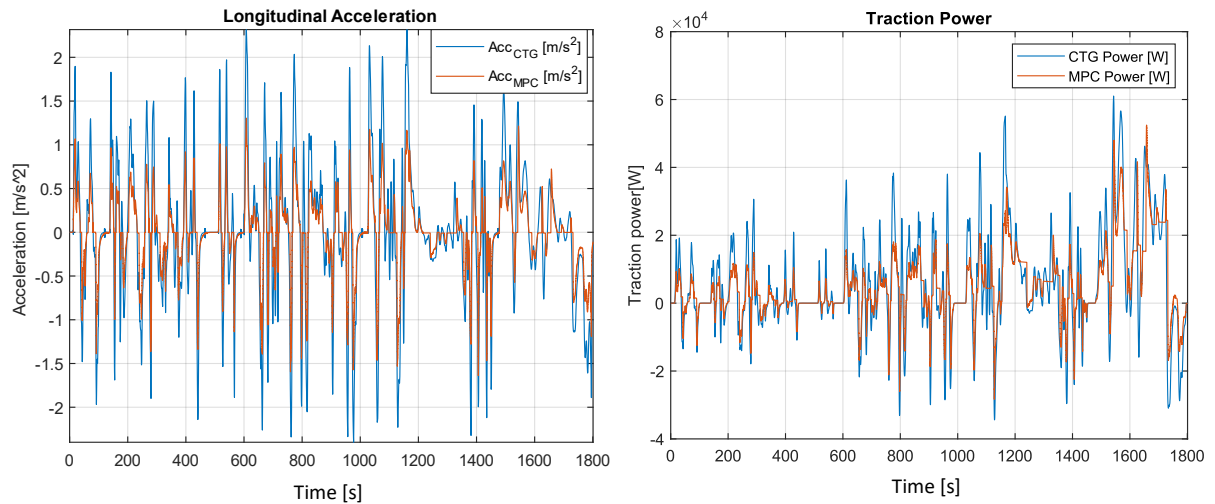


Figure 51: WLTC- [MPC vs CTG] longitudinal acceleration and Traction Power

These results are useful to understand the improvement that can be achieved by implementing this optimization strategy compared to the simplest implementable one.

Observing the plots, it's clear that the acceleration command for each instant is significantly reduced, directly linked to the traction power requested. In this case, all the peaks are consistently lower, thanks to optimization ensuring a lower current request. This reduction is further justified by the improvements showcased in SOC and SOH in the following images.

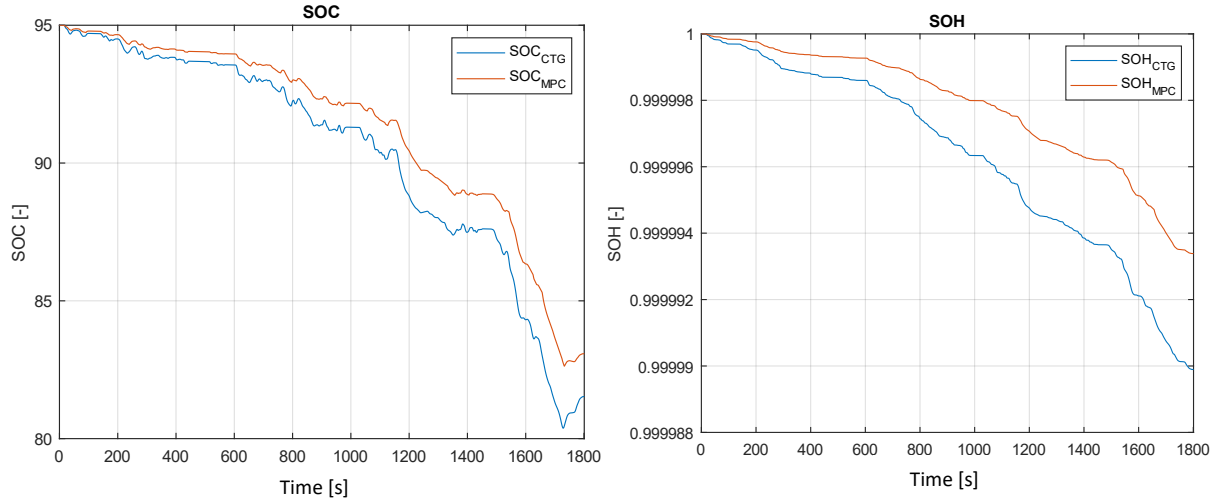


Figure 52: WLTC – [MPC vs CTG] SOC and SOH

Analysing energy consumption and battery health status at the end of the WLTC cycle reveals substantial improvements. In numbers, this translates to a 12.34% improvement in SOC and a 34.2% enhancement in SOH, signifying a remarkable gain in performance. This underscores the potential of a predictive model that leverages information from the leading vehicle. Even with basic data, these predictions yield significant improvements.

EPA BASED SIMULATIONS

All these experiments were replicated for the EPA cycle, showcasing the ability to improve performance in a different scenario. In this case, given the less aggressive nature of the cycle, the improvements are naturally smaller but still substantial. Since these experimental charts do not provide additional information beyond what has been explained, only plots illustrating speed smoothing and commanded acceleration will be presented in comparison to results following a leading vehicle, ensuring completeness. Even for this cycle, all the previously stated findings are reaffirmed, with significant improvements, especially when comparing results with the CTG controller. Relative to WLTC-based simulations, although the improvements are slightly lower, at 7.6% for SOH and 2.8% for SOC, they remain noteworthy.

All simulation results will be summarized at the end of this chapter in the final tables.

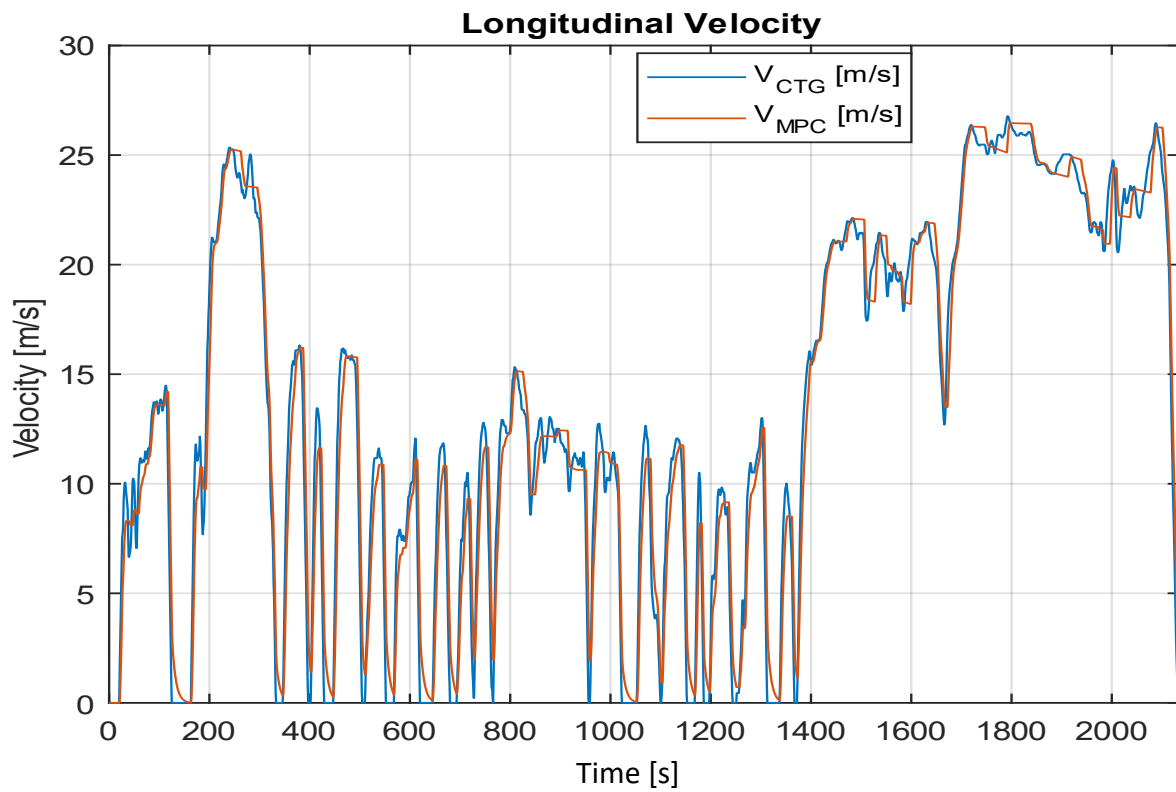


Figure 53: EPA Longitudinal speed Plot LMPC PH = 10, CH = 2

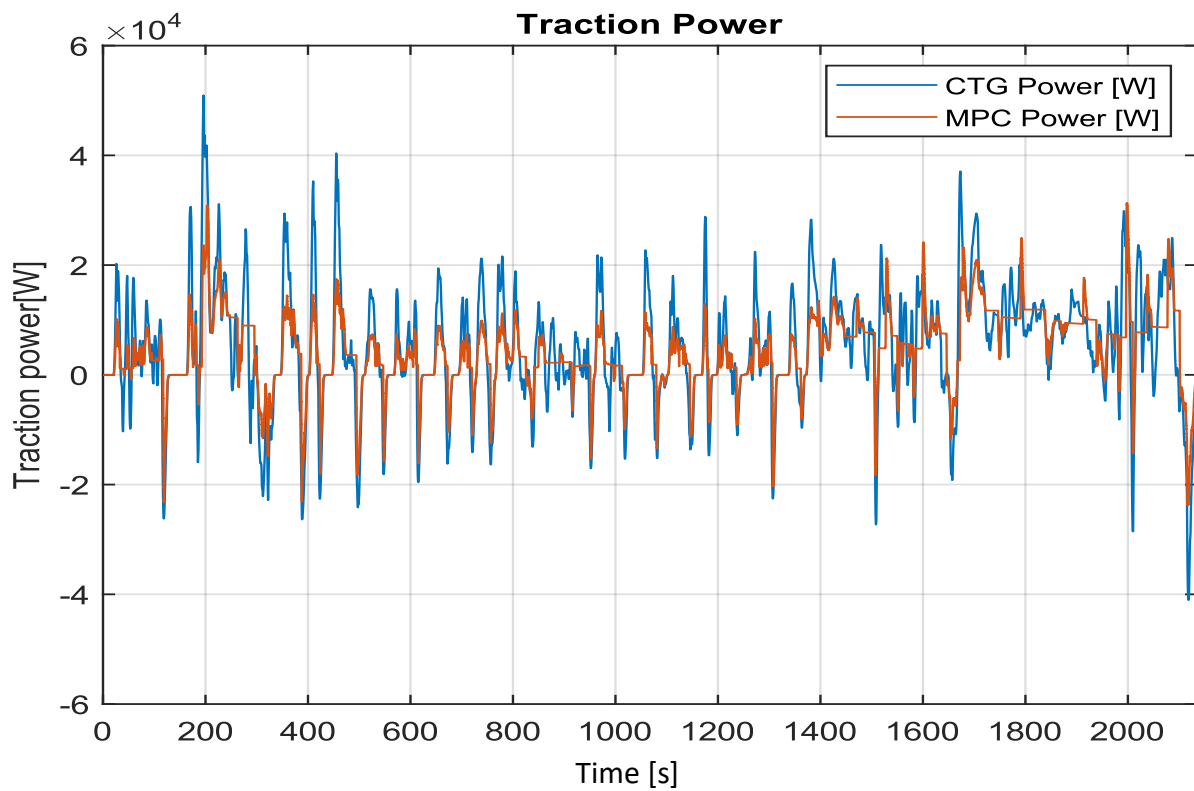


Figure 54: EPA Longitudinal acceleration Plot LMPC PH = 10, CH = 2

4.6 Noise and delay sensitivity analysis

To enhance the realism of the simulation, we considered incorporating noise and data delays from the leading vehicle information. This addition aimed to evaluate the control strategy's robustness and effectiveness. To introduce these external disturbances, we incorporated two simple blocks into the input for Leading Speed and Leading Position:

- Delay block: This block enables us to specify the number of time-steps after which the information entering the block must be provided as output.
- Band Limited White Noise: This block allows us to create a white noise signal with a predefined maximum oscillation amplitude.

The delay block should be implemented before providing the information as input to the MPC controller, while the white noise is added to that data by simple summation, as shown below:

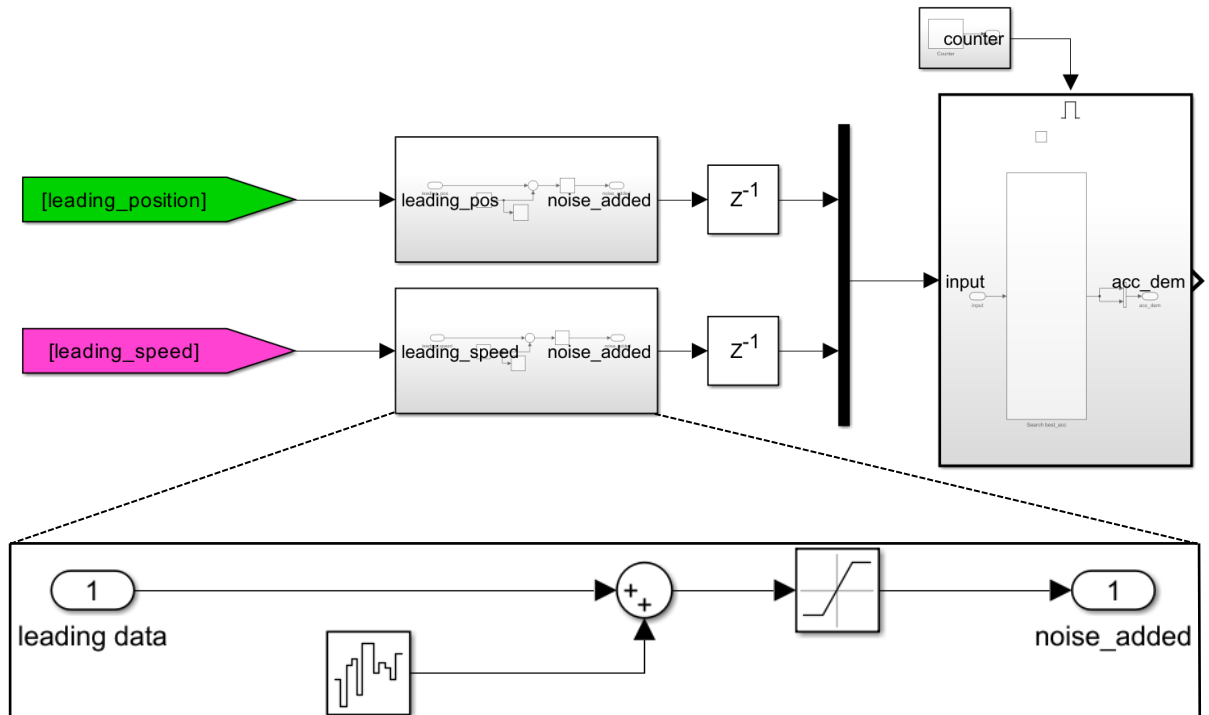


Figure 55: Noise and Delay implementation

Within the Noise block, you can observe the inclusion of a saturation block before the output, which is bounded between zero and infinity. The lower bound is essential to discard unrealistic information that, in specific conditions such as when the vehicle starts from zero speed, might result in negative speed or position values. We analysed the effects of these two contributions separately to comprehend the influence they have.

4.6.1 Delay in data Communication and Sensor data acquisition

Delays in communication, whether in Vehicle-to-Vehicle (V2V) or Vehicle-to-Infrastructure (V2I) communication, as well as inherent sensor acquisition delays, can have significant impacts on the performance and safety of connected and autonomous vehicles. The magnitude of these delays varies and depends on the sensors and infrastructure used.

Since our application is non-safety-related, we considered using 5G cellular network technology for communication and a specific radar, LLR4 [21], commonly used in vehicle applications. According to references [21] and [28], the delays induced by these technologies are as follows:

- The long-range radar has a cycle time of 60 ms, indicating how frequently the sensor collects and processes data or updates its measurements.
- The latency values for cellular network technology, representing the delay or lag in data transmission between a sender and receiver, are highly dependent on the level of technology implemented. According to test results from Ookla, average latency values for specific countries are 32 ms for the United States (US) and 37 ms for Italy. While these values are averages and can vary by country, they provide a useful reference, especially since they are lower than the delay induced by the sensor.

Having identified a range of reasonable delay values, we assessed whether their implementation would lead to significant modifications. Considering a simulation time-step of 100 ms in Simulink, the minimum delay we can implement is at least that value, resulting in an overestimation of the disturbance.

Within one time-step, assuming worst-case scenarios with maximum speeds in the WLTC, the speed variation is approximately 0.175 m/s, and the distance travelled is around 3.6 m. Given these values, we expect practically negligible variations in the speed profile and more significant changes in relative distance. Particularly with respect to distance values, the ego vehicle's controller consistently receives delayed information, effectively acting as if it were one time-step behind. This discrepancy causes the actual real distance to be poorly managed, leading to unnecessary increases in the gap from the leading vehicle at each moment leading the vehicle out of the upper bound limit. While this is almost imperceptible in speed, it's more noticeable in the relative distance. The phenomenon is illustrated in the following plots:

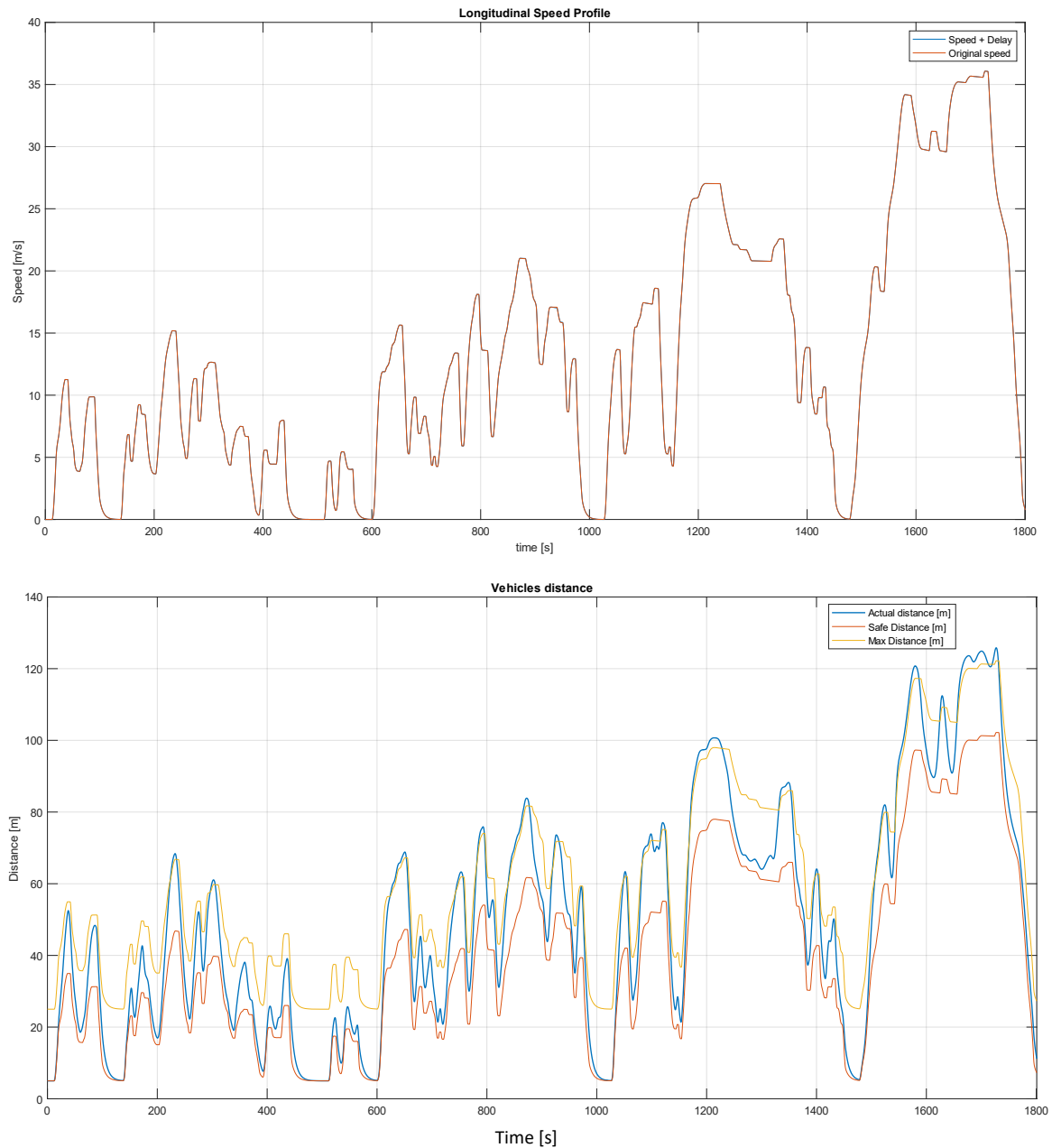


Figure 56 WLTC - Delay effect on Relative distance and Speed

This behaviour has minimal influence on the results. In fact, SOC and SOH remain practically the same because the MPC operates exactly as before, and the effect on distance goes unnoticed since the controller continuously takes into account the delayed information it receives.

We also repeated this simulation using the EPA cycle. Here, the results remained almost unchanged, but slight differences in the speed plots became more apparent due to the delay. These differences are more noticeable because, although the cycle is less aggressive, there are more points where the speed remains higher. Consequently, the error becomes more evident, especially in the speed chart.

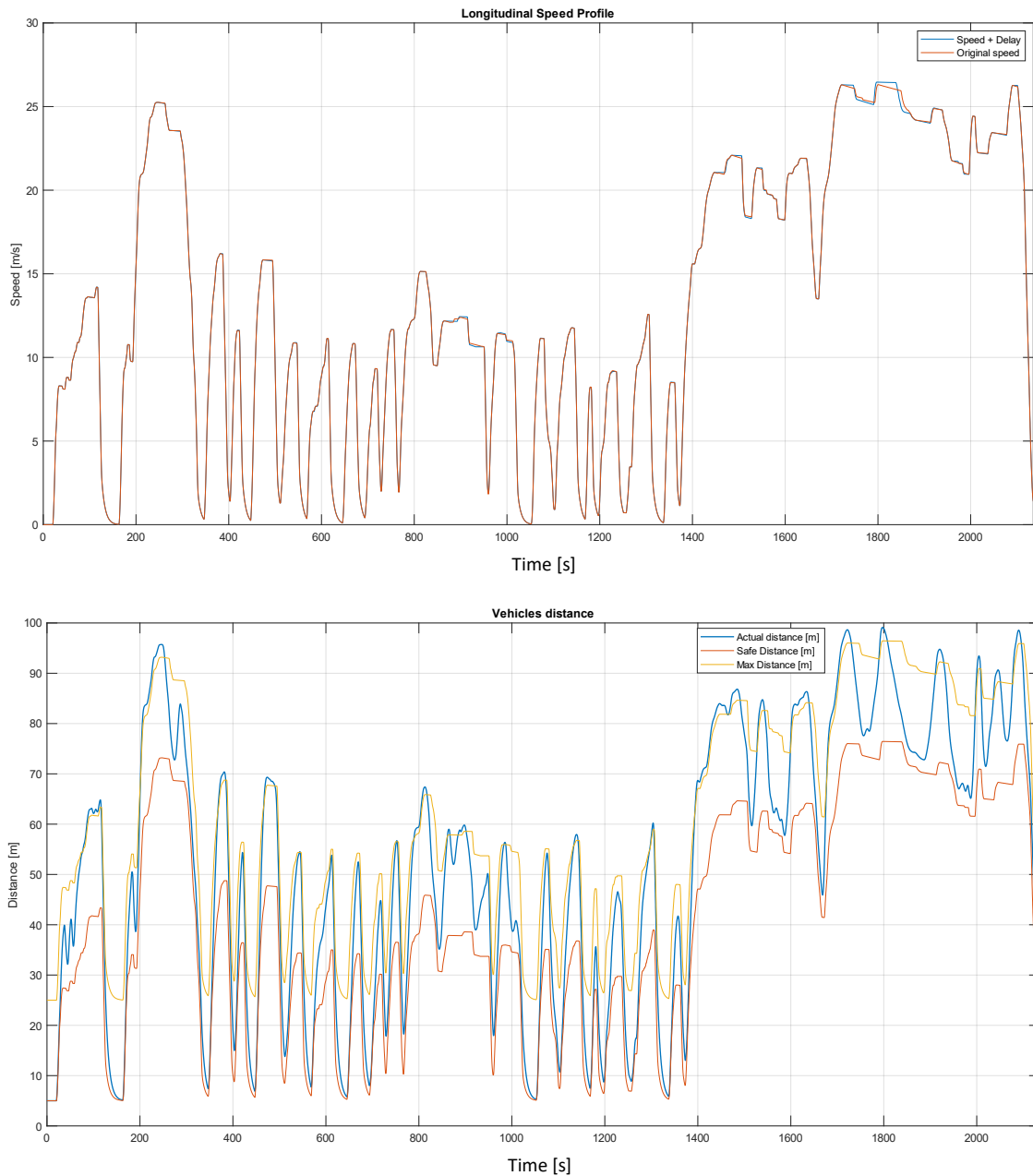


Figure 57: EPA-Delay effect on Relative distance and Speed

4.6.2 Noise in Sensor data acquisition

Another aspect that requires consideration is the presence of noise in the acquired information. From a communication perspective, data is divided and transmitted in packets according to specific protocols that ensure the correct addressing and formatting of messages. In the event of transmission errors, messages are retransmitted to correct these errors, contributing to communication latency. Data packets can be lost for various reasons, such as network congestion, obstacles, or interference. In all such cases, when a packet is lost, it must be

retransmitted. Therefore, introducing noise into the signal due to this reason is not entirely appropriate.

Instead, a more realistic scenario involves the noise introduced by sensor acquisition. Due to their nature, sensors inherently possess some degree of error in their measurements, leading to variations from the nominal values. This variation is precisely what sensor accuracy describes. For example, [21] indicates that the speed and distance measuring error achievable with the described long-range radar are approximately ± 0.11 m/s and ± 0.12 m, respectively.

Given this information, we introduced white noise with an amplitude within this specific range and a frequency equal to the simulation frequency (10 Hz) into our input signals, as shown in Figure 58:

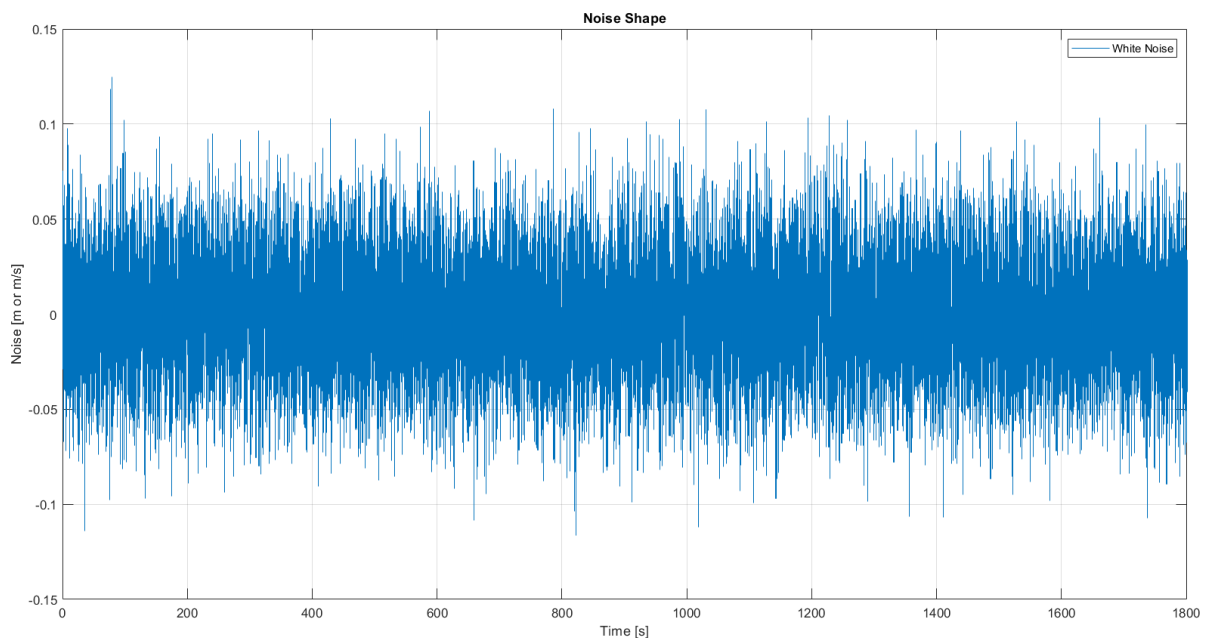


Figure 58: White Noise signal

The addition of this noise has a more significant impact compared to the introduction of communication delays. This is because noise introduces oscillations in the commanded acceleration, which, even if to a small extent, deteriorates performance. Consequently, this effect results in a decrease in performance compared to improvements without noise, amounting to -2.17% for SOC and -2.3% for SOH improvements. These values are obtained when simulating a WLTC. However, the decrease is nearly the same for the EPA, with -2.78% for SOC and -2.4% for SOH.

This noise has similar adverse effects for both cycles and on both SOC and SOH. This is because its detrimental impact is independent of speed, unlike the Delay. Consequently, using the same controller, if the vehicle is capable of following a specific driving cycle, it should be

robust enough to perform effectively in other cycles. The obtained results confirm all these assertions. For the sake of clarity, WLTC results are displayed below.

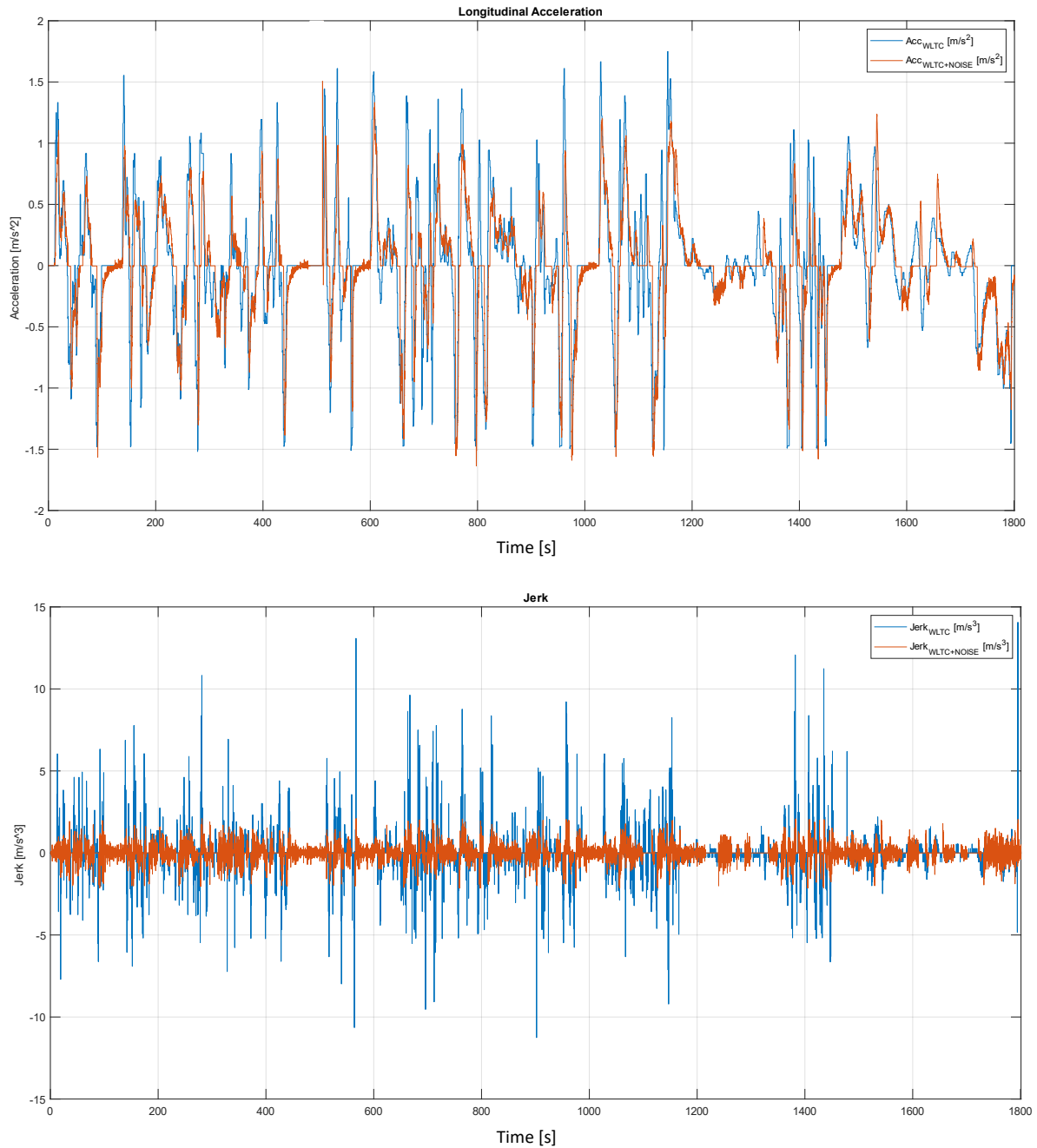


Figure 59: WLTC - Acceleration and Jerk with added NOISE

These plots clearly illustrate how noise influences the introduction of oscillations in the acceleration command, resulting in a much more disturbed profile. This, in turn, affects the jerk values, which are reduced but exhibit significant oscillations. Therefore, the inclusion of noise and delays in the simulation allows us to assess the model's capability to operate effectively in more realistic environments without excessively compromising performance. Simulate noise and delay together doesn't provide any additional information because the delay merely

translates the command one step earlier, but it doesn't alter the random nature of the noise. In essence, the two effects operate independently and do not add to or amplify each other, resulting in no added information or meaningful interaction between them in this context.

4.7 MPC Results

In the concluding section, we delve into the comprehensive results obtained from an array of MPC tests. These tests evaluate various control strategies, shedding light on their individual impacts and effectiveness. As we analyse the outcomes, our focus gravitates towards critical performance indicators.

Throughout these experiments, our primary aim was to optimize the control strategy to achieve several key objectives. Foremost among these was the minimization of energy consumption, monitoring SOC factor. Additionally, we observe maximum acceleration in absolute value since both positive and negative peaks greatly influence State of Health (SOH), another important parameter to be monitored. We also examined jerk to ensure passenger comfort and trip duration to ensure sufficient traffic fluidity and customer satisfaction.

These findings serve as a comprehensive overview, illustrating the extent of improvement brought about by each method while rigorously monitoring the essential parameters that drive performance and sustainability in our system.

Before delving into the detailed results, it's crucial to have in mind that the maximum jerk and maximum acceleration data presented here refers to peak values. Consequently, these peak values might not necessarily translate to consistently higher accelerations across the whole cycle. This observation helps explain instances where we may find higher values in places where we expect lower ones.

4.7.1 WLTC based simulation Results

The first set of tables shows the benefits of some architecture compared to the leading vehicle following a single WLTC starting from 95% SOC. The gain values refer to the difference between the architecture results subtracted to the leading one and the normalized over the leading one to have a percentage of improvement. The time cycle gap is evaluated in the same way but in this case the percentage shown represents the additional time required to drive over the cycle by the specific architecture. Through this some frequent trend could be observed:

- CTG has almost everywhere the worst results with worsening with respect to the leading vehicle especially on SOH and SOC which are the most relevant parameters to consider.

- Increasing the PH performance improvement is higher compared to the leading vehicle in particular for SOC and SOH.
- NMPC with PH = 10 and CH = 1 has almost everywhere the best results as expected.
- Adding linearization performance slightly reduces with respect to the best architecture of NMPC, observing table 6, but are still satisfactory.
- Increasing CH the performances are generally slightly worsened.
- The inclusion of a delay in the simulations has minimal impact on the results, whereas the addition of noise marginally diminishes performance, as highlighted in Table 7.

CACC effects		HVAC OFF			
Benefits wrt WLTC					
	ΔSOC Gain	max acc Gain	Time cycle Gap (23,25 km)	Jerk max Gain	ΔSOH Gain
CTG	-8,80%	-37,14%	0,11%	72,15%	-37,95%
NMPC P.H. = 2 C.H. = 1	2,91%	4,00%	0,36%	7,54%	7,82%
NMPC P.H. = 5 C.H. = 1	3,47%	14,29%	0,36%	28,88%	8,79%
NMPC P.H. = 10 C.H. = 1	4,12%	16,57%	0,28%	81,15%	10,15%
LMPC P.H. = 10 C.H. = 1	3,79%	16,00%	0,35%	89,40%	9,84%
LMPC P.H. = 10 C.H. = 2	3,71%	6,40%	0,35%	84,42%	9,67%
LMPC P.H. = 10 C.H. = 2 + NOISE	3,63%	5,71%	0,36%	84,21%	9,46%
LMPC P.H. = 10 C.H. = 2 + DELAY	3,71%	5,71%	0,36%	84,35%	9,63%

Table 5: WLTC - Architecture Benefits compared to Leading vehicle

CACC effects			HVAC OFF
LMPC vs NMPC			
CACC vs EPA	Δ SOC	-7,84%	
	Δ SOH	-3,1%	

Table 6: WLTC - LMPC vs. NMPC performance reduction

CACC effects			HVAC OFF
<u>NOISE Analysis</u>			
CACC vs WLTC	Δ SOC	-2,17%	
	Δ SOH	-2,3%	

Table 7: WLTC - Decrease In performance of LMPC PH = 10, CH = 2 adding Noise

All the subsequent data has been compared also with the CTG strategy, instead of the leading vehicle, to unveil the full spectrum of optimization benefits for each architectural configuration. In this context, the improvements are more pronounced, and, in general, all the trends elucidated earlier remain consistent.

CACC effects		HVAC OFF			
Benefits wrt CTG					
	ΔSOC Gain	max acc Gain	Time cycle Gap (23,25 km)	Jerk max Gain	ΔSOH Gain
WLTC driver	8,09%	27,1%	-0,11%	-259%	27,5%
NMPC P.H. = 2 C.H. = 1	10,76%	30,0%	0,25%	-232%	33,2%
NMPC P.H. = 5 C.H. = 1	11,28%	37,5%	0,25%	-155,4%	33,9%
NMPC P.H. = 10 C.H. = 1	11,87%	39,2%	0,17%	32,3%	34,9%
LMPC P.H. = 10 C.H. = 1	11,57%	38,8%	0,24%	62,0%	34,6%
LMPC P.H. = 10 C.H. = 2	11,50%	31,8%	0,24%	44,1%	34,5%
LMPC P.H. = 10 C.H. = 2 + NOISE	11,42%	31,3%	0,25%	43,3%	34,4%
LMPC P.H. = 10 C.H. = 2 + DELAY	11,50%	31,3%	0,25%	43,8%	34,5%

Table 8: WLTC - Architecture Benefits compared to CTG controlled vehicle

4.7.2 EPA based simulation Results

CACC effects		HVAC OFF			
Benefits wrt EPA					
	ΔSOC Gain	max acc Gain	Time cycle Gap (28,49 km)	Jerk max Gain	ΔSOH Gain
CTG	-7,51%	-67,55%	0,06%	60,63%	-31,79%
NMPC P.H. = 2 C.H. = 1	1,69%	0,66%	0,06%	18,24%	5,08%
NMPC P.H. = 5 C.H. = 1	2,22%	1,32%	0,05%	37,11%	6,00%
NMPC P.H. = 10 C.H. = 1	2,99%	1,32%	0,05%	54,84%	7,65%
LMPC P.H. = 10 C.H. = 1	2,76%	1,32%	0,05%	85,85%	7,61%
LMPC P.H. = 10 C.H. = 2	2,76%	-9,27%	0,08%	86,67%	7,60%
LMPC P.H. = 10 C.H. = 2 + NOISE	2,68%	-14,57%	0,04%	86,60%	7,43%
LMPC P.H. = 10 C.H. = 2 + DELAY	2,76%	-11,26%	0,04%	86,54%	7,44%

Table 9: EPA- Architecture Benefits compared to Leading vehicle

All the architectural configurations tested on a WLTC have been replicated while travelling on the EPA cycle. The results continue to exhibit the same trends elucidated previously. In this scenario, the magnitudes are marginally reduced, as repeatedly clarified, owing to the less aggressive nature of the cycle. Consequently, the optimization strategy's effectiveness diminishes somewhat, as the reduction in peaks becomes smaller in percentage. Nevertheless, the improvements remain noteworthy. In this case as well, the results are compared with those of a CTG-controlled vehicle. Sensitivity analyses for disturbances have also been conducted in this context, comparing the definitive architecture (LMPC PH = 10, CH = 2) both with and without noise, and assessing the performance differences between LMPC and NMPC.

CACC effects		HVAC OFF			
Benefits wrt CTG					
	Δ SOC Gain	max acc Gain	Time cycle Gap (28,49 km)	Jerk max Gain	Δ SOH Gain
EPA driver	6,99%	40%	0,06%	-154%	24%
NMPC P.H. = 2 C.H. = 1	8,55%	41%	0,00%	-108%	28%
NMPC P.H. = 5 C.H. = 1	9,05%	41%	0,00%	-60%	29%
NMPC P.H. = 10 C.H. = 1	9,76%	41%	0,00%	-15%	30%
LMPC P.H. = 10 C.H. = 1	9,55%	41%	0,01%	64%	30%
LMPC P.H. = 10 C.H. = 2	9,55%	35%	-0,03%	66%	30%
LMPC P.H. = 10 C.H. = 2 + NOISE	9,48%	31,6%	0,02%	66,0%	29,8%
LMPC P.H. = 10 C.H. = 2 + DELAY	9,55%	33,60%	0,02%	0,02%	29,77%

Table 10: EPA - Architecture Benefits compared to CTG controlled vehicle

CACC effects			HVAC OFF
<u>NOISE Analysis</u>			
CACC vs EPA	Δ SOC	-2,78%	
	Δ SOH	-2,2%	

Table 11: EPA - Decrease in performance of LMPC PH = 10, CH = 2 adding Noise

CACC effects			HVAC OFF
LMPC vs NMPC			
CACC vs EPA	ΔSOC	-7,69%	
	ΔSOH	-0,5%	

Table 12: EPA - LMPC vs. NMPC performance reduction

In conclusion, the MPC (Model Predictive Control) strategy detailed throughout this discussion offers significant advantages in the realm of battery electric vehicles (BEVs). This approach has proven instrumental in considerably reducing both battery degradation and energy consumption. By doing so, it not only could aids automotive companies in successfully meeting homologation test requirements but also could steers BEVs toward a more sustainable choice for modern mobility.

One of the most compelling aspects of the strategy presented in the preceding sections is its adaptability. It can be seamlessly integrated into the majority of existing vehicles, regardless of their powertrain architecture. This integration is accomplished with remarkable simplicity, as it operates solely at the software level. This accessibility allows for a flexible and scalable deployment, making it an attractive proposition for the broader automotive industry's pursuit of cleaner, more efficient transportation solutions.

5. HVAC Model

As explained in the introduction of the thesis the CACC strategy was a part of a broader project developed. In fact, a second optimization strategy was created in parallel with the one explained in this thesis with the purpose of leveraging auxiliaries power demand according to traction power request without compromising the latter. In order to make this second optimization strategy effectively working and analyse its contribute, a vehicle cabin model and a control strategy used as reference has been also developed and will be explained in this section. Before delving into the detail of the implemented model let's analyse the motivation behind the choice of working on this strategy.

5.1 Auxiliaries effect on battery life and energy consumption

The Heating, Ventilation, and Air Conditioning (HVAC) system is a vital component in both conventional Internal Combustion Engine (ICE) vehicles and Battery Electric Vehicles (BEVs), accounting for a significant share of their energy consumption. However, it's crucial to recognize that the impact of HVAC systems differs substantially between these two vehicle types. This distinction underscores the critical need for dedicated HVAC optimization tailored to BEVs.

In ICE vehicles, the HVAC system's energy requirements are relatively modest. This is primarily due to the availability of excess heat generated by the engine's inherent inefficiencies. In colder months, this surplus heat is efficiently harnessed to warm up the cabin, with minimal fuel consumption attributed mainly to fan operation. Consequently, the HVAC system's energy demand remains relatively low in ICE vehicles.

On the contrary, BEVs operate on an entirely different principle. With the absence of an internal combustion engine, BEVs rely solely on electrical power for cabin temperature control. This reliance on electric power results from the remarkable efficiency of electric motors, which minimizes heat dissipation. To tackle the challenge of cabin heating in a BEV, more complex HVAC systems are employed, often integrating Positive Temperature Coefficient (PTC) heaters or heat pumps [30]. This complexity leads to higher power consumption, occasionally reaching up to some kW. Remarkably, this power demand can constitute a substantial portion of the total energy consumption in a BEV moreover, this consumption is highly dependent on external conditions, which in turn significantly impacts the BEV's driving range and battery longevity. As observed in the following figures, the power demand of auxiliary systems and the

overall battery current request exhibit a strong correlation with seasonal changes in ambient temperature. The figures, obtained from a study on a Nissan Leaf, a compact vehicle equipped

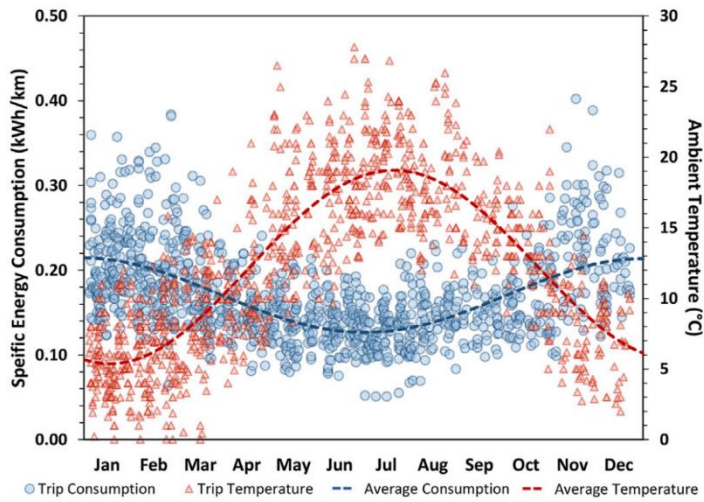


Figure 60: Monthly change in specific energy consumption and ambient temperature [29].

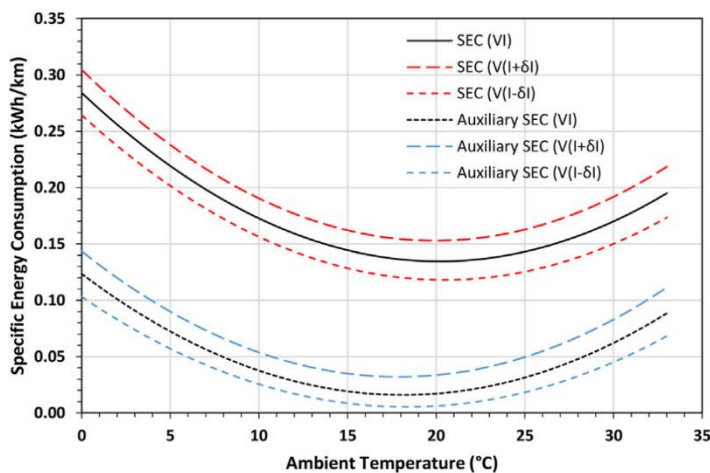


Figure 61: Sensitivity analysis of battery current in the calculation of specific energy consumption and auxiliary specific energy consumption with varying ambient temperature [29].

with a 24 kWh battery capacity, depict the vehicle's performance during a driving cycle designed to meet Real Driving Emission (RDE) requirements [29]. Upon closer examination of these plots, it becomes evident that specific energy consumption is significantly influenced by temperature variations, manifesting differently across the various seasons. Furthermore, the same study provides an insightful chart illustrating the impact of temperature fluctuations on battery current. It also dissects this influence, isolating the contribution of auxiliary systems' energy consumption. This approach enables us to assess the proportion of energy consumption attributable solely to auxiliary systems and to gauge their sensitivity to temperature fluctuations.

This heightened dependence on the HVAC system underscores that any inefficiencies or excessive power consumption directly affect the BEV's driving range. Furthermore, given the comparatively longer recharging times and limited charging infrastructure for BEVs, as discussed in introduction chapter, the consequences of excessive HVAC power consumption can be exacerbated, potentially leading to range anxiety among drivers.

While tackling these challenges, it's worth noting that many HVAC optimizations for BEVs can be implemented through software-level adjustments. This approach offers a cost-effective means of enhancing performance without necessitating extensive hardware modifications. By

harnessing data on battery fading and implementing sophisticated software strategies, BEV manufacturers can bolster energy efficiency and extend battery life.

In essence, optimizing the HVAC system in BEVs represents a multifaceted endeavour. It not only significantly influences energy consumption and driving range but also demands innovative solutions to navigate the unique complexities of electric vehicle architecture. This chapter introduces a foundational model. This model has been crafted to simulate the authentic evolution of cabin temperatures within a BEV. Employing a standard Proportional-Integral (PI) controller, it adeptly manages the cabin's temperature dynamics. Through this approach, we can emulate real-world scenarios, capturing the fluctuations in energy consumption and the variations in battery degradation highly dependent on external conditions and the desired cabin temperature. Subsequently, building upon this baseline model, another study was conducted to develop a strategy aimed at optimizing HVAC power consumption. While my direct involvement in this strategy creation was limited, it will be shortly described in future section. The final chapter of this thesis will concentrate on the integration of this strategy with the developed CACC strategy, examining their combined impact on energy consumption and battery life degradation.

5.2 Cabin Model

To assess the power demands of the HVAC system, has been developed a cabin model that accurately simulates the temperature changes within the vehicle. To ensure the model closely resembles real-world conditions, has been utilized Simscape™ as working environment. The primary assumption made in this model is the omission of cabin moisture level monitoring. We made this choice to streamline the model, assuming that the air entering the cabin contain the required humidity level for comfort, considered in the HVAC model design.

5.2.1 Interaction with external environment

The general First Law of Thermodynamics for an open system, tailored to describe the energy balance in a particular context, such as a vehicle cabin with various heat sources, internal energy changes, and heat removal mechanisms will be shown in order to understand all the contributes playing a role in the examined thermodynamic system. In this case the considered relation is the following:

$$\dot{Q}_{sun} + \dot{Q}_{conv,cond} + \dot{Q}_{passeng} = \left(\frac{\partial E_t}{\partial t} \right)_{C.V.} + (\dot{m}_{recirc} + \dot{m}_{leak}) c_p T_{cabin} - \dot{m}_{HVAC} c_p T_{HVAC,out} \quad (XXXIII)$$

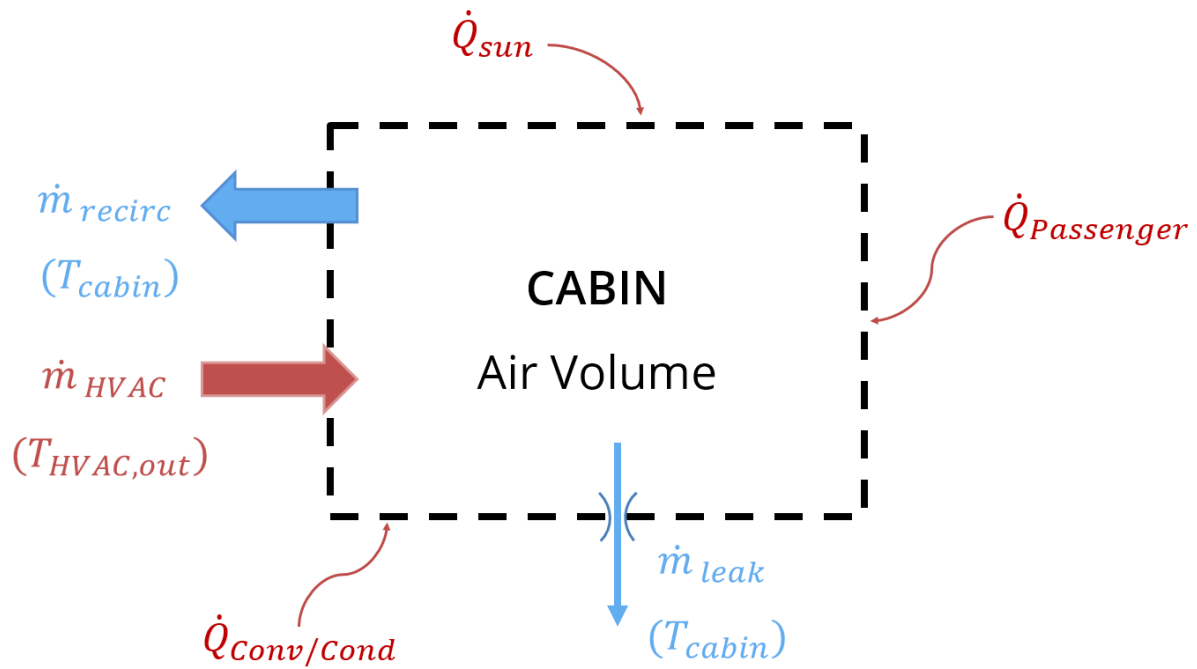


Figure 62: Cabin C.V. thermodynamic contributions

Upon examining the equation and the accompanying figure, several key components become evident. Let's delve into these contributions:

The first three terms account for the net heat transfer rates into the system, originating from diverse sources. These sources encompass solar radiation (\dot{Q}_{sun}), convection and conduction ($\dot{Q}_{\text{conv,cond}}$), and passenger-generated heat (\dot{Q}_{passeng}). In the general first law of thermodynamics equation, these terms collectively represent ΔQ , the net heat transfer rate.

The subsequent term $\left(\frac{\partial E_t}{\partial t}\right)_{\text{C.V.}}$ represents the rate of change of total energy content within the control volume (C.V.). In the general equation, this term represents ΔE , encapsulating changes in the total energy content within the open system.

The last two terms encompass the heat that is either added to or removed from the system. This can be attributed to recirculated air, leaks, and the HVAC system. In the general equation, this pair of terms collectively signifies ΔH , indicative of the rate of change of enthalpy within the system. For context, \dot{m}_{HVAC} , \dot{m}_{recirc} , \dot{m}_{leak} denote the mass flow rates of air managed by the HVAC system, the recirculation system, and any leakages (as previously explained). Additionally, c_p represents the specific heat capacity of air, $T_{\text{HVAC,out}}$ is the temperature of air as it exits the HVAC system, and T_{cabin} denotes the temperature within the vehicle cabin.

5.2.2 Solar radiation contribution

The first contribute described in equation XXXIII is the solar radiation one (\dot{Q}_{sun}). This term reflects the heat transfer rate from the sun to the system. In an open system, energy can be exchanged with the environment through heat. We consider incoming solar radiation \dot{q}_{sun} as a constant value, typically set at $1000 \frac{W}{m^2}$ for worst-case scenarios during summer months at midday [31]. When solar radiation reaches the vehicle's surface, it is divided into different components that affect the cabin temperature. For instance, when it interacts with a glass surface, some of the radiation is reflected, and some is transmitted, while metal panels only experience reflection. Subsequently, a portion of this radiation is absorbed by the external surface layer and then conducted through all internal layers, ultimately reaching the innermost layer. At this point, temperature differences between the internal layer and the internal air, as well as between the external air and external layer, induce heat exchange through convection. The expressions describing these contributions are derived through the application of fundamental thermodynamic relations:

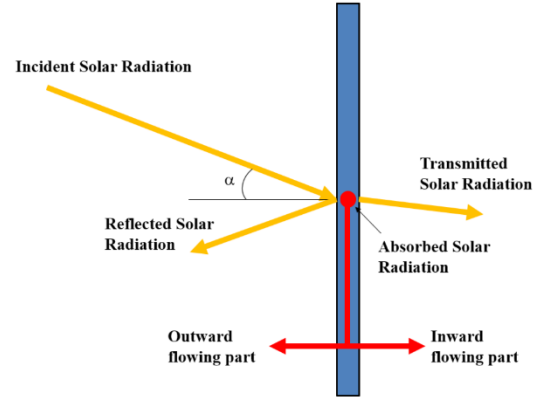


Figure 63: Incident Solar Radiation Contributions

$$\dot{Q}_{rad\ trans\ glass} = \tau \cdot \dot{q}_{sun} \cdot \sum_{i=1}^{N_{surf}} C_i \cdot A_i \cdot \sin(\alpha_i) \quad (XXXIV)$$

$$\dot{Q}_{rad\ abs} = \rho \cdot \dot{q}_{sun} \cdot \sum_{i=1}^{N_{surf}} C_i \cdot A_i \cdot \sin(\alpha_i) \quad (XXXV)$$

The first equation quantifies the contribution given by the sun directly transmitted into the cabin through vehicle glass surfaces. Here τ represents the transmissivity of the glass, as previously introduced. \dot{q}_{sun} is the incoming solar radiation, while the summation accounts for contributions from each glass surface, including a shading coefficient C_i and only the surface orthogonal to the incoming solar radiation taken into account multiplying the area times the sin of the incidence α_i .

The second equation encompasses the portion of radiation absorbed by both the glass and metal surfaces, considering a different absorptivity factor ρ for metal and glass surfaces. An average shading factor \bar{C} is utilized to account for the various surfaces, and consequently it is taken out from the summation.

As outlined in reference [31], the key surfaces contributing to the effects described earlier are as follows:

- Roof
- Floor
- Glasses

It's important to mention that doors are not considered in these equations. This omission is based on the assumption that doors, featuring almost vertical surfaces, have negligible contributions to radiation transfer. This is due to the sine of the incidence angle $\sin(\alpha_i)$ approaching near-zero values for such surfaces. Subsequently, these prepared contributions feed into a dedicated block modelling the cabin's heat transfer process.

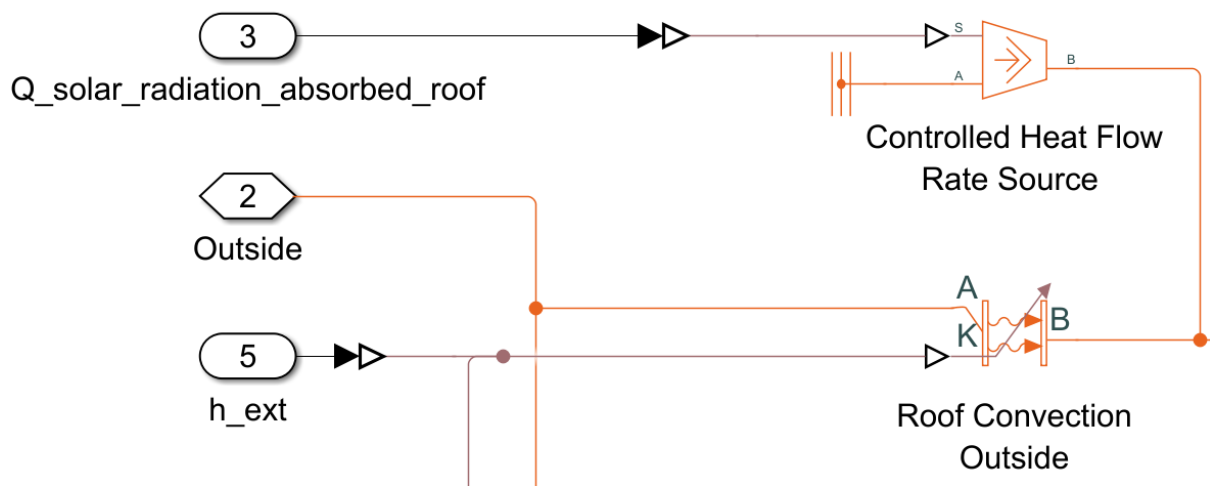


Figure 64: Simscape™ - Solar radiation absorbed roof

Starting with the first contribution, as illustrated in the initial diagram, we can observe how the solar radiation absorbed by the roof is incorporated into the model. Within the Simscape™ environment, a primary block named 'Controlled Heat Flow Rate source' is employed for this purpose. This block functions as an ideal energy source, capable of maintaining a controlled heat flow rate independently of temperature variations. It is important to note that this block has no specific setup and exclusively receives the source input, which, in this case, represents solar radiation absorbed by the roof.

The second block utilized in the simulation is the 'Convective Heat Transfer' block. This component models heat transfer through convection induced by fluid motion, which will be explained in the following paragraph. It's crucial to highlight that the input radiation is intentionally placed after the convective heat transfer block. Given that it represents absorbed radiation, it needs to act directly on the roof surface, as will be clarified in the subsequent section, where the mechanism of heat transfer within the roof layers via conduction is explained.

Consequently, the image left side represents the external environment, while the right side symbolizes the transition into the cabin.

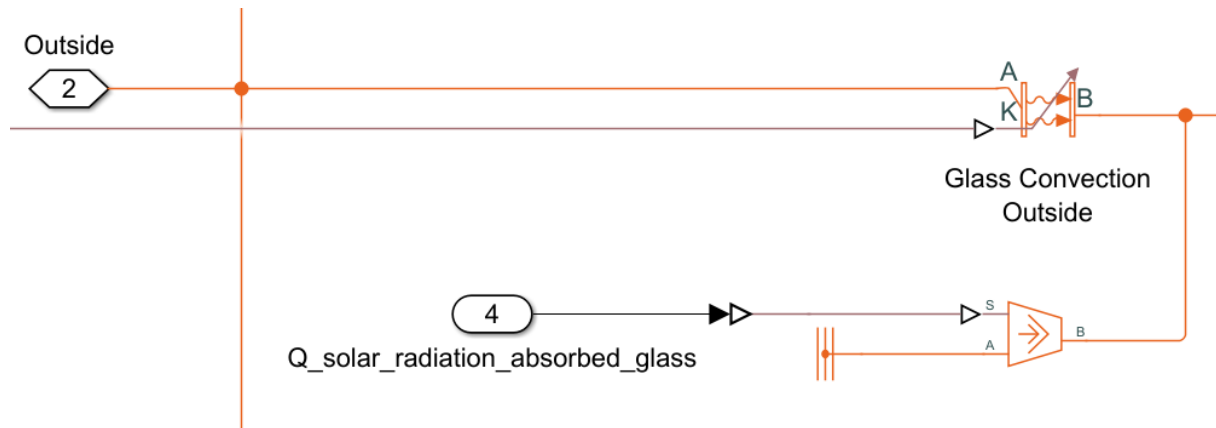


Figure 65: Simscape™ - Solar radiation absorbed glass

Concerning the second contribution, solar radiation absorbed by the glass, the same approach is employed. The input is positioned after the convection block for the same reasons as described earlier.

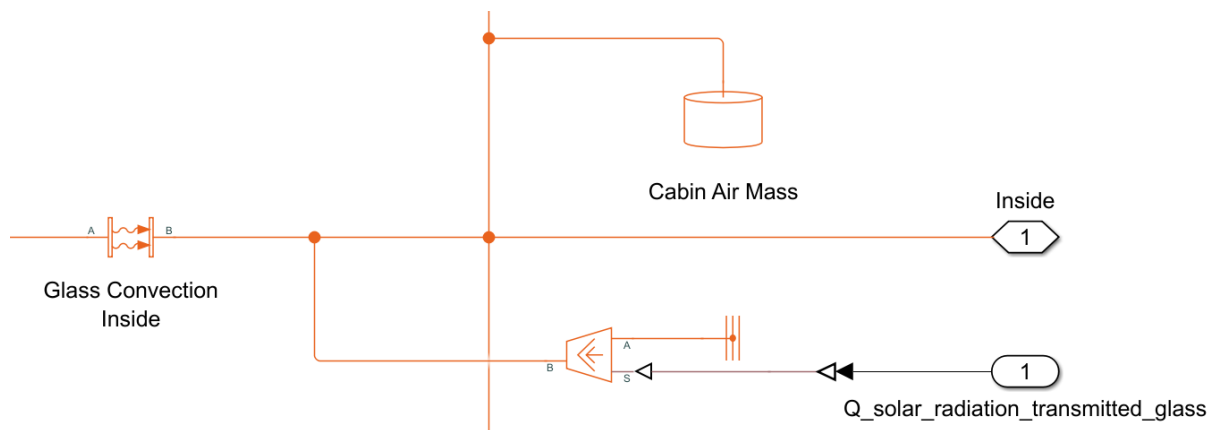


Figure 66: Simscape™ - Solar radiation transmitted glass

The final contribution stemming from solar radiation is the portion transmitted through the glass and directly entering the vehicle. In this case, the input block, as observed in the preceding diagram, is applied to the innermost section on the right, where it directly influences the thermal mass that simulates the thermal inertia of the vehicle cabin's air. It's worth noting that in the previous scenario, a thermal mass representing the external air was not included. This omission is based on the assumption that external air mass, being infinite, is capable of maintaining a constant temperature, regardless of the vehicle's conditions. Conversely, within the cabin, a finite amount of air is contained, and temperature variations are significant. As a result, a thermal mass is introduced, calculated as the product of the cabin volume (considered constant

due to fixed walls) and air density. Similar blocks are employed to incorporate this contribution as input, which, in turn, influences the cabin temperature, as depicted in the thermal model.

5.2.3 Conduction – Convection thermal contribution

The second contribution within equation XXXIII is the one related to conduction and convection.

Concerning convection, the 'Convective Heat Transfer' block is introduced at the two extremes of the model, representing the heat exchange between the external air and the external metal/glass layer, as well as between the internal air and the more internal layer of the vehicle. In this case the surfaces involved also includes the contribution of lateral doors. To ensure a realistic cabin temperature evolution with the appropriate thermal inertia, also conductive heat transfer is considered. Moreover, a detailed internal layer stratigraphy is employed for the most influential surface, such as the roof, due to its large area and significant contribution from solar radiation, which significantly impacts the results.

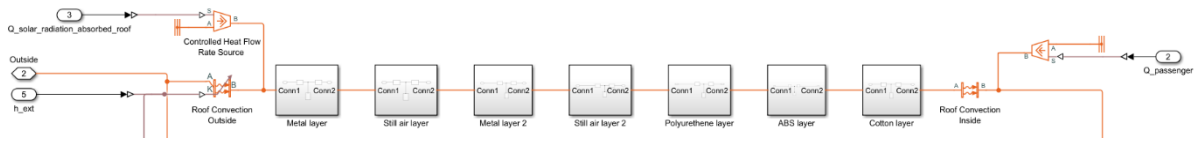


Figure 67: Simscape™- Roof Conduction/Convection

The diagram above depicts on the left the external air, and on the right, the internal air. As expected, the first blocks simulate convective heat transfer from both sides. This block receives, for example, on the left side, the external air temperature ('Outside'), roof surface, and minimum heat transfer coefficient, enabling the simulation of heat transfer by convection between the external air and the roof. The second external input to this block is the convective heat transfer coefficient h_{ext} . Since the vehicle is in motion, the heat transfer coefficient due to convection varies with speed. This effect, is considered using the following relation from [33]:

$$h_{ext} = 1.163 \cdot (4 + 12\sqrt{\dot{x}_{vehicle}}) \quad (XXXVI)$$

This equation is formulated so that when the vehicle is stationary, the convection heat transfer coefficient is equal to $4.652 \text{ W}/(\text{m}^2\text{K})$.

Once the heat exchange through convection is evaluated, it 'flows' into the metal, where the stratigraphy detailed by [31] is implemented. Here, heat is transmitted by conduction between each layer. To further enhance the realism of heat transmission, a thermal mass is introduced

between the two halves of each layer to accurately account for thermal inertia, as depicted in the following figure.

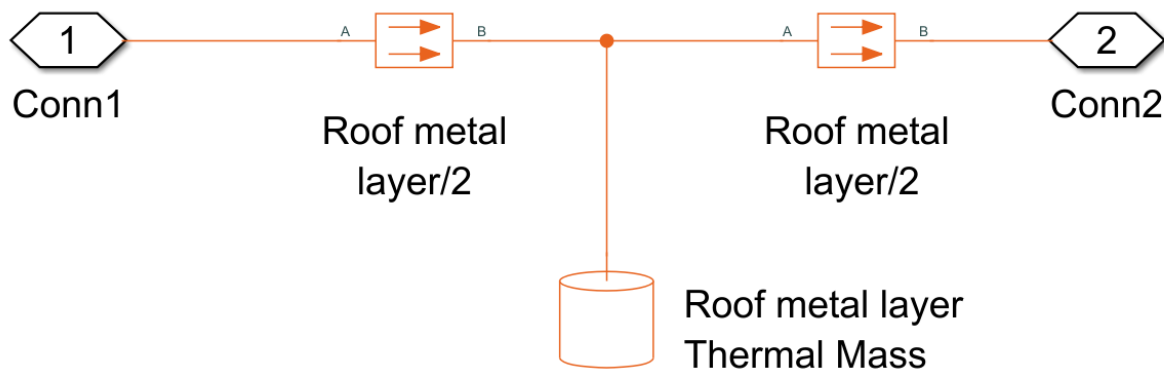


Figure 68: Simscape™ - Conduction roof metal layer

The mass is calculated by multiplying the material density by the single layer's thickness and the roof surface (as each layer covers the entire area). This process is repeated for all the layers, considering the thickness and conductive heat transfer coefficient for each layer. It's essential to note that the insulant layer of still air is considered in the conduction transfer since, being motionless, it doesn't induce any convective effects.

For the glass, doors, and floor surfaces, a more simplified structure is employed, applying the same concept used for the roof. This involves considering a single material layer with an overall thickness and an average convective heat transfer coefficient, along with a thermal mass in between. The areas considered include the front/rear windshield and lateral windows for the glass. For the doors, it encompasses lateral doors, the trunk, and the front firewall. The floor is treated as a unified surface covering the entire underbody.

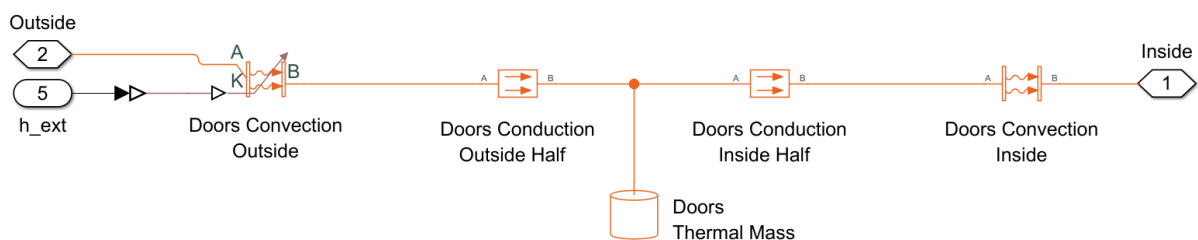


Figure 69: Simscape™ - Conduction/Convection doors

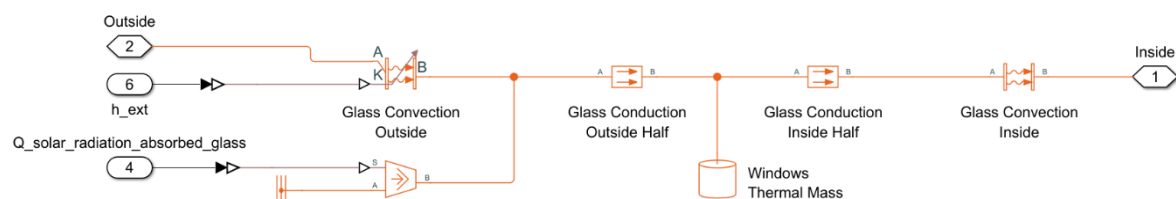


Figure 70: Simscape™ - Conduction/Convection glass

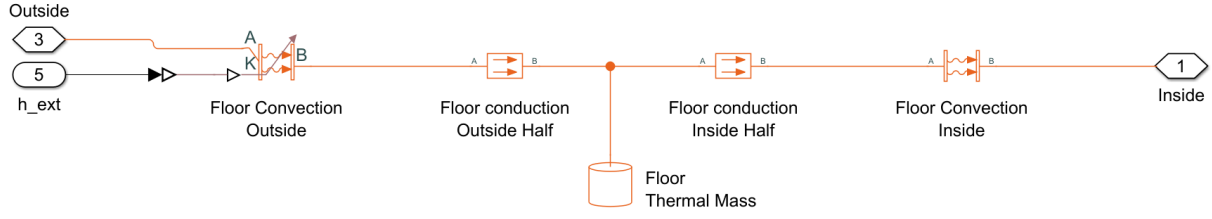


Figure 71: Simscape™ - Conduction/Convection Floor

5.2.4 Passenger contribution

The final heat source considered in the system is that generated by passengers inside the vehicle. $\dot{Q}_{passeng}$ term accounts for the heat transfer rate associated with passengers inside the system. For instance, the metabolic heat generated by passengers can contribute to the energy balance of the system. To incorporate these factors, the following relation from [32] is applied:

$$\dot{Q}_{passeng} = N_{pas} \cdot A_{pas} \cdot M_s \quad (\text{XXXVII})$$

Here N_{pas} represents the number of passengers within the cabin, A_{pas} symbolizes the average passenger areas set equal to 1.8 m^2 and M_s , represents the sensible specific heat set equal to 70 W/m^2 . This contribution should be considered as originating from inside the cabin and directly connected to the innermost point in the model.

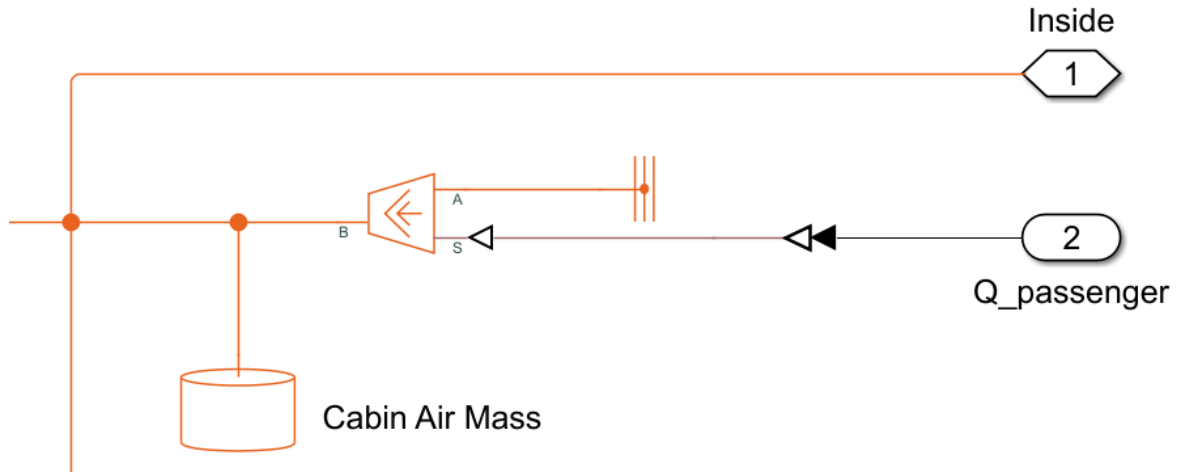


Figure 72: Simscape™ - Passenger heat contribution

For a comprehensive view of the entire structure encompassing all contributions, the following figure provides an overview of the previously described components.

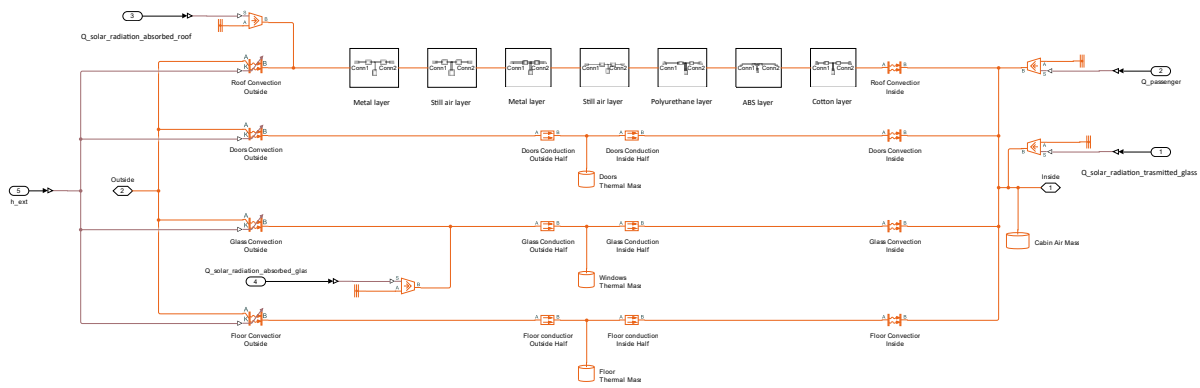


Figure 73: Simscape™ complete cabin heat transfer blocks

5.2.5 Cabin Control Volume model

Once all the external heat transfer contributions have been analysed, we delve into the mass flow rate equilibrium within the control volume represented in the right part of equation XXXIII. A dedicated set of blocks is employed with the assumption of a constant control volume (the vehicle cabin's volume). The following image illustrates all these contributions and how they have been considered.

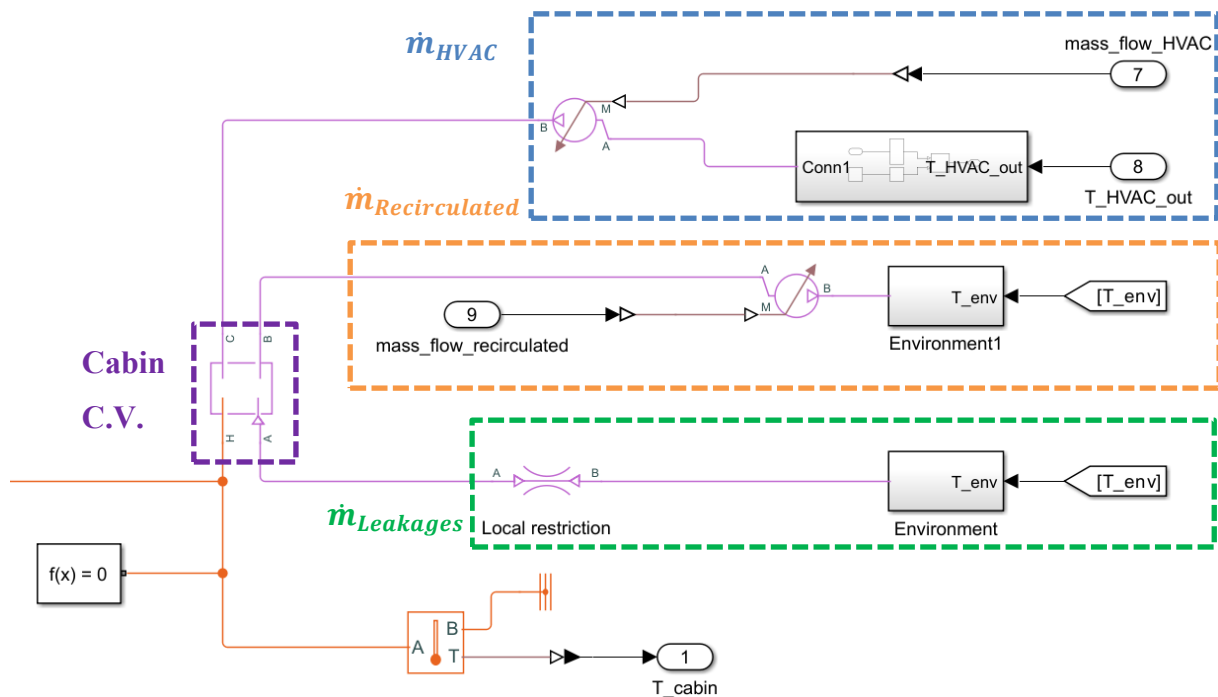


Figure 74: Simscape™ mass equilibrium blocks

The purple square, labelled, **Cabin control volume (C.V.)**, simulates a constant volume chamber containing gas. This block models mass and energy storage and evolves pressure and

temperature according to the dynamics of the gas volume. Port H of the block represents the thermal conserving port related to the thermal mass contribution received from the previously illustrated blocks' output. This input evolves in response to temperature differences between the environment and the cabin. The remaining ports represent chamber input ports where all the previous mass flow rate contributions are taken into account for equilibrium.

The first term, \dot{m}_{HVAC} , represents the air mass flow rate regulated by the HVAC system as it enters the cabin. This parameter is under the control of a dedicated controller, which acts in response to the relative difference between the desired internal cabin temperature and the actual temperature. As a result, this mass enters the cabin with a precise temperature, known as $T_{HVAC,out}$. The Simscape™ block, referred to as the 'Controlled Mass Flow Rate Source,' is the component responsible for providing a specific mass flow rate at a designated temperature and direction. This source can ensure a predetermined mass flow rate independently of pressure differentials. It's important to note that this block neglects flow resistance and involves no heat exchange with the environment. When the mass flow rate is positive, it signifies that gas flows from port A to port B. To specify the environment from which the gas originates, the following blocks have been incorporated.

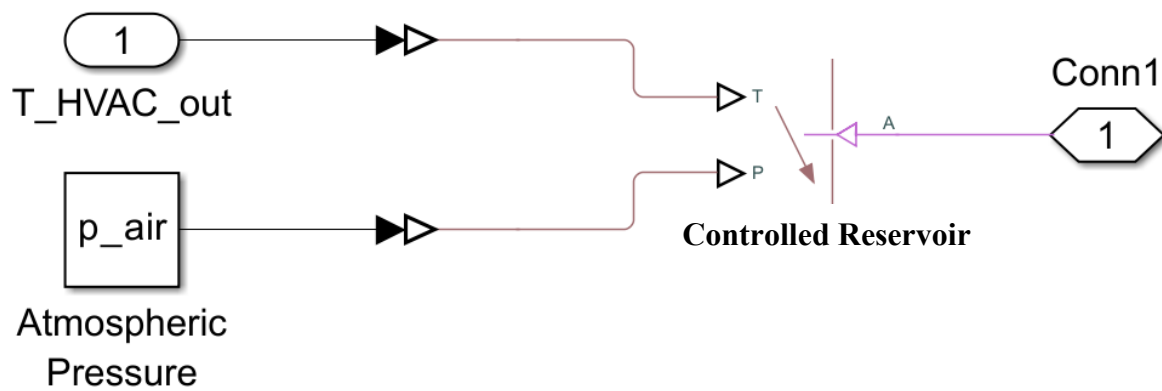


Figure 75: \dot{m}_{HVAC} boundary conditions

The controlled reservoir block defines an environment with infinite volume, which allows it to maintain consistent temperature and pressure characteristics, essentially behaving as a quasi-static volume. The second component, $\dot{m}_{recirculated}$, refers to a predefined portion of air within the cabin that is recirculated and directed back to the HVAC system. Further details regarding this will be discussed in the following section, where the control architecture is explained. In this context, considering the cabin as the control volume, this mass is exiting the system. Consequently, in this scenario, the 'Controlled Mass Flow Rate Source' block is essentially reversed, indicating an outflow from the cabin. As this air must ultimately return to the HVAC

model's starting point, it is regarded as entering an external environment with ambient pressure and temperature. This environment is simulated accurately by using the 'controlled reservoir block' and modifying the boundary conditions for temperature and pressure.

The last contribution is denoted as $\dot{m}_{leakages}$. In real-world scenarios, the control volume is not hermetically sealed due to mechanical tolerances, resulting in additional airflow entering and exiting the cabin based on temperature differentials between the interconnected environments. To address this contribution, a 'local restriction block' is employed to simulate pressure loss due to a flow area restriction, similar to an orifice in a gas network. Importantly, this process involves no heat exchange with the environment. Given that this mass is exchanged with the external ambient in this case, the flow directed from point A to point B reaches an environment simulated in a manner consistent with that used for the recirculated mass.

With all the contributions considered and evaluated, a cabin model capable of simulating a realistic temperature evolution is completed and ready for control. To assess the realism of temperature increase within the vehicle, a free temperature evolution simulation was conducted with the HVAC system turned off. This simulation considered the following initial conditions:

- External temperature of 32°C
- No passenger inside the vehicle
- 1000 W/m^2 solar radiation acting vertically on the vehicle
- Initial cabin temperature of 23 °C

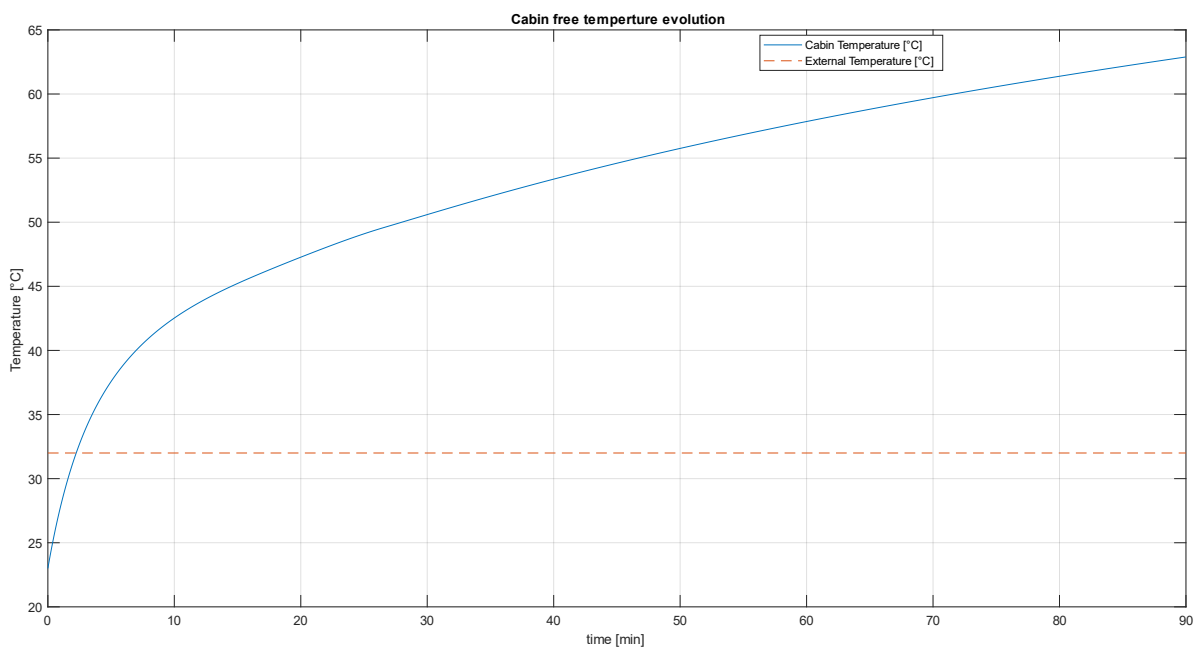


Figure 76: Free Cabin temperature evolution

Examining the chart, it becomes evident that the initial temperature increase exhibits a steeper slope. This is because the heat flow is directed into the cabin due to both solar radiation and the temperature difference (initially, $T_{\text{cabin}} < T_{\text{environment}}$). As the cabin temperature surpasses the external temperature, the slope of the curve decreases, although it continues to rise. This is because the incoming solar radiation contributes more heat than the cabin loses to the surroundings. In the end, the temperature evolution tends to stabilize, reaching reasonable temperatures for a vehicle stopped, exposed to direct sunlight in the worst-case scenario.

5.3 HVAC system model and control

In this paragraph, we will elaborate on how the HVAC architecture is modeled and controlled to achieve a more realistic representation, taking into account benchmark solutions found in the literature. The baseline architecture considered for HVAC in a BEV has been adopted from [30]. This architecture involves a cooling phase executed by an evaporator, which absorbs heat from incoming air to produce a cooling effect. Subsequently, a heating process is required. Given the absence of an Internal Combustion Engine (ICE), a heat pump system has been integrated. This system employs a condenser to release heat into the incoming airflow and control the temperature of the air entering the cabin. Based on this, the following scheme has been employed:

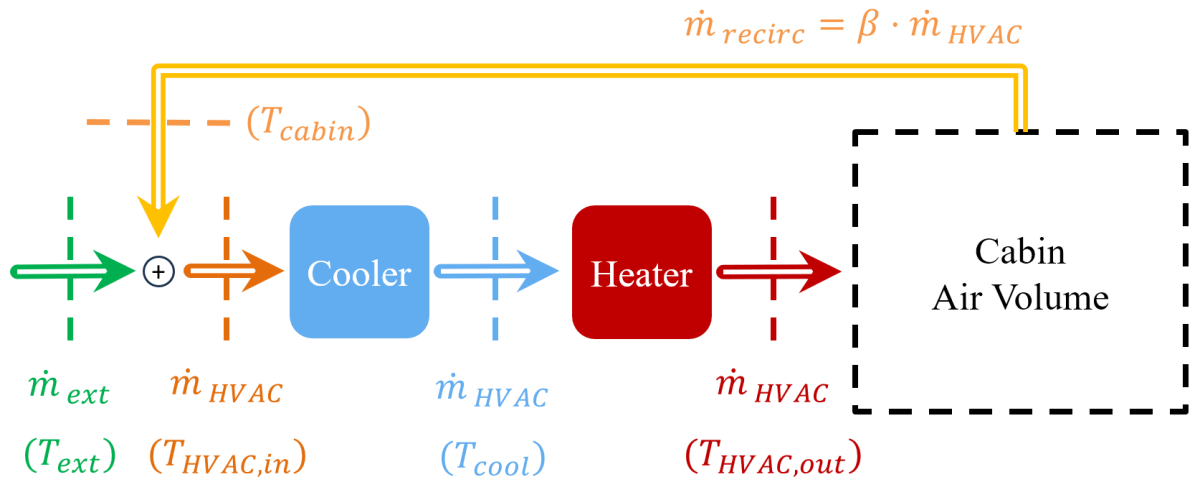


Figure 77: HVAC system architecture

In this context, one can observe the interplay of mass flow rate and temperature contributions. To begin, external air, maintained at a fixed ambient temperature, is subjected to a certain mass flow rate regulated by a fan. It is then mixed with a constant fraction of recirculated cabin air, considered at the current cabin temperature. These two streams, once combined, are introduced into the cooling system with a specific total mass flow rate, \dot{m}_{HVAC} , at a designated temperature,

$T_{HVAC, in}$. For the purposes of this system, we have ignored mass flow rate losses through the components, assuming a constant value throughout the system.

The architecture is engineered so that the air exiting the cooling component achieves a predefined temperature, T_{cool} which depends on T_{ref} , representing the desired cabin temperature. This temperature has been selected to ensure that the air entering the cabin maintains an acceptable relative humidity level for passenger comfort, falling within the range of 20% to 60% [34]. This is derived from an analysis of the Mollier chart, revealing that to stay within this relative humidity range, cooling of up to 3°C is necessary for a reference temperature of 18°C, and up to 17°C for a reference temperature of 27°C within the cabin. For the intermediate values within this range, a linear interpolation method has been applied. By doing so, we guarantee that the air exiting the cooler is maintained at the appropriate humidity level.

Subsequently, this air undergoes reheating through the heat pump while retaining a constant absolute humidity. This process consistently maintains passenger comfort. Once the air enters the cabin, it undergoes temperature evolution, and the entire procedure is repeated to attain the desired cabin temperature. To establish this control system, we rely on the initial assumption of mass conservation:

$$\dot{m}_{HVAC} = \dot{m}_{Recirculated} + \dot{m}_{Leakages} \quad (XXXVIII)$$

Utilizing this assumption, we formulate the first law of thermodynamics as follows:

$$\dot{Q}_{sun} + \dot{Q}_{conv,cond} + \dot{Q}_{passeng} - \dot{Q}_{HVAC} = \left(\frac{\partial E_t}{\partial t} \right)_{C.V.} \quad (XXXIX)$$

Where:

$$\dot{Q}_{HVAC} = \dot{m}_{HVAC} c_p (T_{cabin} - T_{HVAC,out}) \quad (XL)$$

$$\left(\frac{\partial E_t}{\partial t} \right)_{C.V.} = M_{air} c_p \frac{\partial T_{cabin}}{\partial t} \quad (XLI)$$

Basing on that it is possible to elaborate on how cabin temperature control and HVAC power demand are determined. The following steps outline the process required to derive the desired parameters:

1. The first analysed information is the temperature error $T_{ref} - T_{cabin}$. This error is pivotal in understanding and regulating the required HVAC power. It serves as an input for a Proportional-Integral (PI) controller, which produces the desired \dot{Q}_{HVAC} , directly related to the cabin temperature variable T_{cabin} . Consequently, the HVAC power demanded will

vary depending on the temperature difference between the desired and actual cabin temperatures.

2. Knowing the desired reference temperature inside the cabin, a specific value for $T_{HVAC,out}$ is imposed. This value is set to be 7°C lower than the reference temperature. This reduction is necessary in achieving a swift approach to the reference temperature and is particularly vital because, to maintain a constant cabin temperature while continuously exposed to solar radiation, a temperature lower than the desired cabin temperature is necessary.
3. Having \dot{Q}_{HVAC} , the actual T_{cabin} , $T_{HVAC,out}$ and c_p (air specific heat) at our disposal, we can reverse Equation XL to find the required, \dot{m}_{HVAC} needed to satisfy the heat power demand of the cabin.
4. With this variable in hand, we can further calculate the recirculated mass flow rate by simply multiplying it by the constant recirculation ratio. At this stage, having \dot{m}_{HVAC} , $T_{HVAC,out}$ and $\dot{m}_{Recirculated}$, which are necessary for minimizing the temperature error, they are integrated into the cabin model, as previously explained, enabling the cabin temperature to evolve accordingly.

At this juncture, the control process is concluded, and the temperature evolution is regulated to align with the desired cabin temperature.

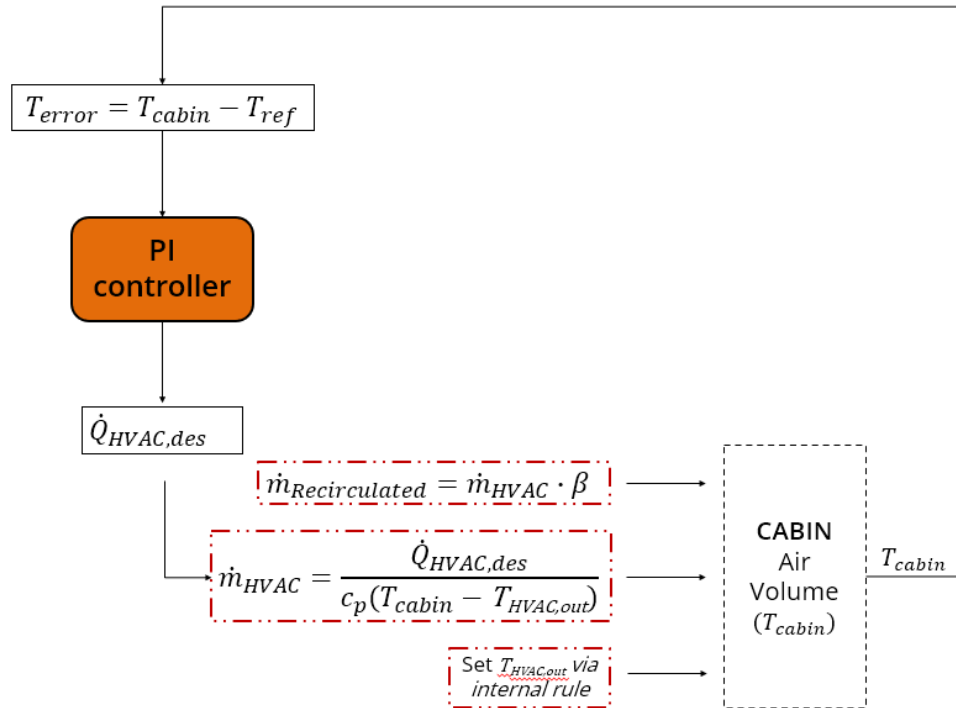


Figure 78: HVAC controlled architecture

To incorporate the HVAC system's impact on energy consumption and battery degradation within the battery model, an assessment of the power required for this operation is essential. The following set of operations is implemented to achieve this.

1. By Knowing \dot{m}_{HVAC} and $\dot{m}_{Recirculated}$, their subtraction yields $\dot{m}_{Leakages}$.
2. In reference to the HVAC system architecture, the following relation can be established: $\dot{m}_{HVAC} \cdot T_{HVAC,in} = \dot{m}_{Recirculated} \cdot T_{cabin} + \dot{m}_{ext} \cdot T_{ext}$. By reversing this relation, we can determine $T_{HVAC,in}$, the only unknown variable in the equation.
3. To calculate the total power required by the HVAC system, the thermal power requested by the cooling and heating systems must be assessed:

$$\dot{Q}_{cool} = \dot{m}_{HVAC} c_p (T_{HVAC,in} - T_{cool}) \quad (XLII)$$

$$\dot{Q}_{heat} = \dot{m}_{HVAC} c_p (T_{cool} - T_{HVAC,out}) \quad (XLIII)$$

Starting from these relations, they can be converted into electrical power requirements by considering the coefficient of performance (COP). Additionally, an efficiency term is incorporated to consider additional power required for compressors and heat exchangers power request:

$$P_{cool} = \frac{\dot{Q}_{cool}}{COP} \cdot \frac{1}{\eta_{compressor} \cdot \eta_{heat\ exch}} \quad (XLIV)$$

$$P_{heat} = \frac{\dot{Q}_{heat}}{COP-1} \cdot \frac{1}{\eta_{compressor} \cdot \eta_{heat\ exch}} \quad (XLV)$$

$$P_{HVAC} = P_{cool} + P_{heat} \quad (XLVI)$$

Once all these computations are completed, and the cabin temperature is allowed to evolve while the power requirements are calculated, the process restarts, beginning again at the initial point. At the subsequent time step, the temperature error is reevaluated, and the following steps are executed.

The results presented are derived from various simulations commencing with the cabin initially set at 40°C. These simulations illustrate how the HVAC controller manages the temperature and which are the related power consumption compared to the traction power request.

The initial two plots demonstrate the exemplary management of temperature, starting from the initial cabin temperature and progressing towards the reference temperature. In this scenario, it's noteworthy that the HVAC power starts slightly lower. This is attributed to the cabin

temperature being higher than the external temperature, which enhances heat transfer to the surroundings, thus reducing the power demand on the HVAC. The power requirements stabilize once the reference temperature is achieved. The vehicle follows the WLTC during these simulations.

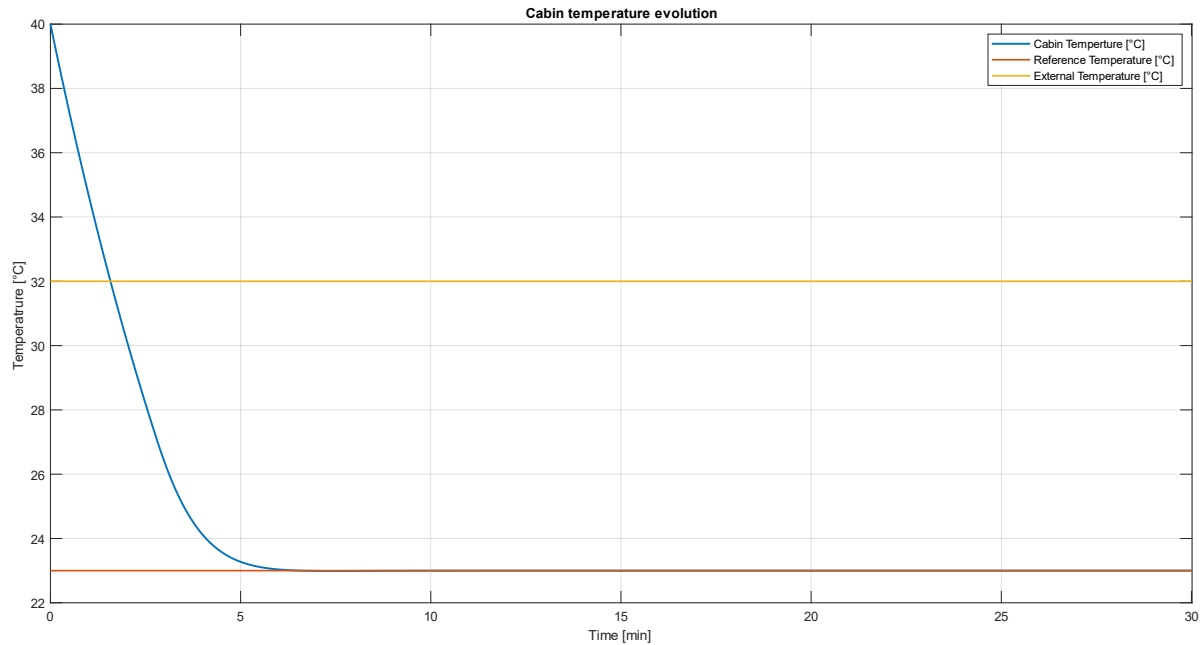


Figure 79: PI controlled cabin temperature evolution with constant reference temperature

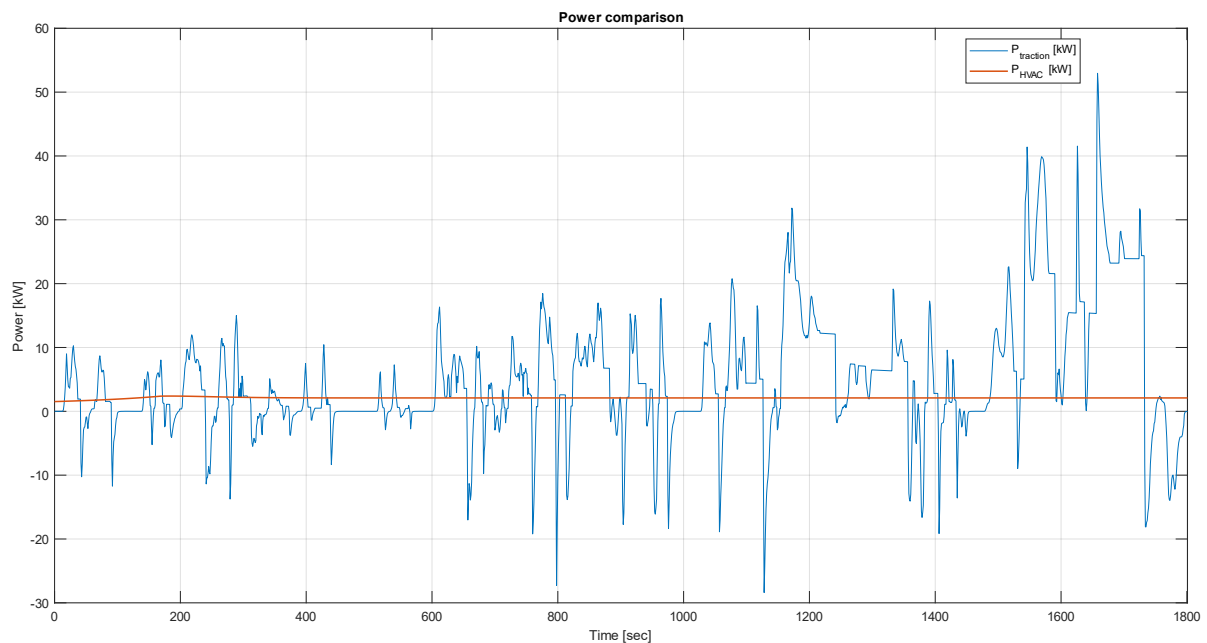


Figure 80: PI controlled HVAC power request compared to Traction Power with constant reference temperature

It's important to emphasize that the power value is dependent on both the reference temperature and the initial vehicle temperature. Consequently, in the following chart, we can observe how altering the reference temperature impacts the results, leading to a variation in the required

power. Additionally, this chart clearly illustrates the controller's capability to promptly track and converge to the updated reference temperature. As expected, the higher is the reference temperature the smaller will be the required power by the HVAC system. Moreover, it is worth noting that when the temperature must increase the controller does not provide any power allowing the temperature to evolve naturally and reacting as soon as the cabin temperature overcome the reference temperature. This behaviour accounts for the temperature overshoot observed in the final temperature plot.

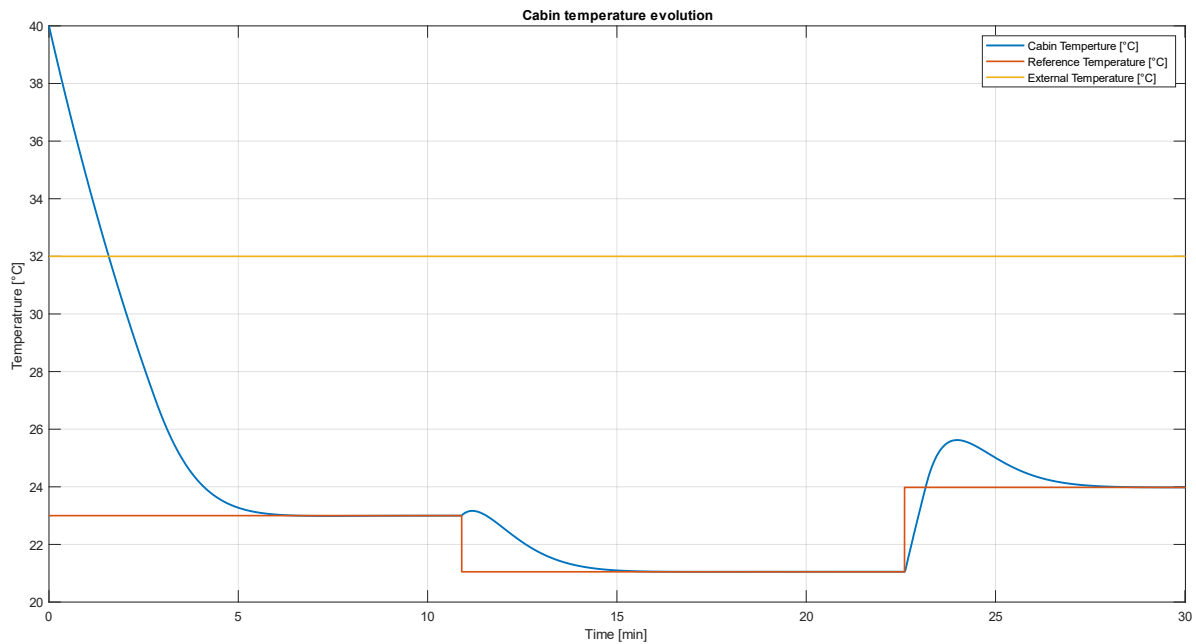


Figure 81: PI controlled cabin temperature evolution with variable reference temperature

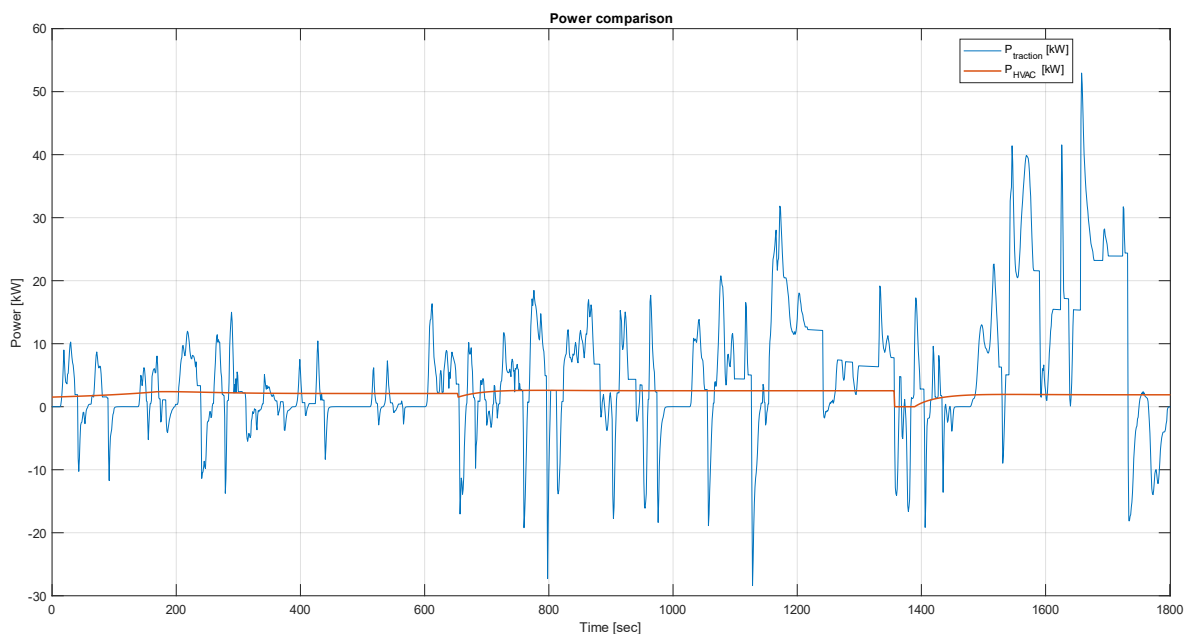


Figure 82: PI controlled HVAC power request compared to Traction Power with variable reference temperature

5.3 Lumped parameter model for cabin temperature evolution

As previously discussed at the outset of this chapter, the HVAC model was created as a foundational framework for the implementation of an optimization strategy. This strategy is designed to control HVAC power with the goal of reducing battery degradation and energy consumption, without compromising traction power request.

The results presented in the preceding section indicate that maintaining a cabin temperature of 23°C when the outside temperature is 32°C leads to a 39% increase in energy consumption and a 17% higher battery degradation compared to a vehicle following the same WLTC cycle with the HVAC system turned off. To address this, the research group (not authored directly by me) has developed an optimization strategy. To ensure real-time applicability of this strategy, a simplified cabin model was created, avoiding computationally intensive Simscape™ blocks. Instead, the original Simscape™ model served as a reference to design a lumped parameter model capable of replicating the temperature dynamics within the desired operational range.

Based on the first law of thermodynamics, the following equation (XLVII) has been derived. Building upon equation XXXIX, it expresses each contribution as follows:

$$C_1 \cdot \dot{q}_{sun} + C_2 \cdot (T_{ext} - T_{cabin}) + \dot{Q}_{passenger} - \dot{Q}_{HVAC} = C_3 \cdot \frac{\partial T_{cabin}}{\partial t} \quad (XLVII)$$

Each parameter introduced in this equation is grounded in physical principles, ensuring that the implemented model is based on realistic assumptions. C_1 denotes an effective surface area of heat exchange with the external environment [m^2], C_2 physically represents an average heat transfer coefficient [W/K], and C_3 corresponds to the thermal capacity of an air volume [J/K]. By utilizing this equation, it can be readily implemented in Simulink through simple elementary blocks, and integrating the last term on the right allows for the calculation of cabin temperature evolution given the other contributions as input.

This approach allows for the simplification of the complex Simscape™ model, making use of these coefficients, which have been fine-tuned to replicate the temperature dynamics within the cabin accurately.

The inclusion of a free cabin temperature evolution serves to illustrate both the limitations of this lumped parameter model and why it was deemed suitable for the specific objectives of our study.

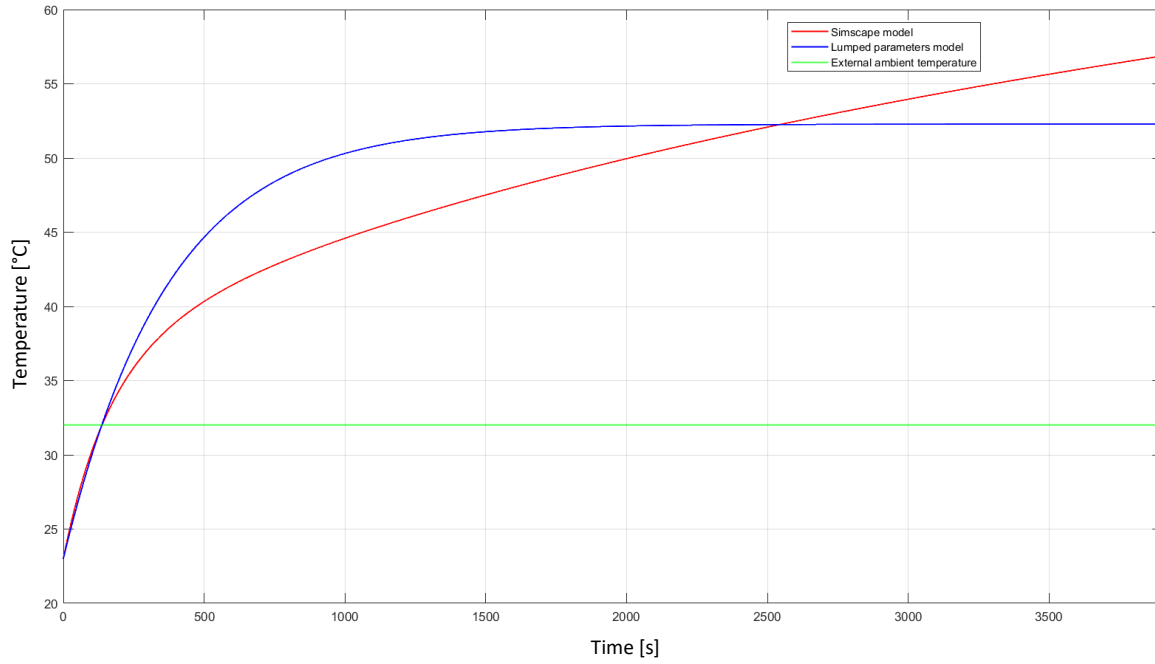


Figure 83: Simscape™ model vs. Lumped parameter model free temperature evolution

In each of these simulations, the initial conditions are consistent, with an initial cabin temperature $T_{\text{cabin}} = 23^{\circ}\text{C}$, no passengers within the vehicle, a stationary vehicle, and a constant solar radiation input $\dot{q}_{\text{sun}} = 1000 \text{ W/m}^2$. Initially, the two curves are nearly identical, but as the simulation progresses, they begin to diverge significantly. This divergence arises from a key limitation of the lumped parameter model, which does not accurately account for the thermal inertia of materials, as effectively managed by the Simscape™ model.

Accordingly, the gap between the two curves widens as the lumped parameter model, represented by the blue curve, responds more rapidly to changes. Moreover, due to this limitation, the materials in the lumped parameter model reach equilibrium with the external environment quickly, ultimately stabilizing at a lower temperature.

Despite this limitation, for the specific application's requirements, the model remains valid. When the HVAC system is active, the cabin temperature consistently remains within the desired range of 18°C to 27°C . Additionally, the model allows for slight temperature variations ($1\text{-}2^{\circ}\text{C}$) during HVAC operation. Consequently, the model remains predominantly within the region where the two curves closely overlap. This characteristic makes the simplified model suitable for the intended purpose, as it significantly reduces computational costs, thereby enabling the real-time implementation of the developed optimization strategy.

6. Integration of Eco-Driving and Thermal Management Strategies for Improved Vehicle Efficiency

In this concluding chapter of the thesis, we explore the culmination of research endeavours centered around optimizing vehicle performance, reducing energy consumption, and minimizing battery degradation. The research journey has encompassed the development of two primary strategies that have been advanced in parallel. Firstly, an Eco-Driving strategy has been designed to optimize vehicle speed profiles by tracking and predicting the behaviour of a leading vehicle (CACC). This Eco-Driving strategy effectively harnesses Model Predictive Control (MPC) techniques to achieve its goals. The second pivotal strategy that has evolved in parallel, although not under the author's direct development, is the Integrated Energy and Thermal Management (IETM) strategy. This integrated strategy is a part of a more comprehensive global project, aimed at optimizing HVAC power commands. Its key objective is to regulate HVAC operations during peak traction power demand scenarios, thereby minimizing battery degradation and, indirectly, reducing energy consumption. This optimization strategy differs from the Eco-Driving structure based on MPC in that it is a punctual optimization strategy, designed to optimize instant by instant a dedicated cost function. It operates without the need for future predictions and ensures that traction power is never compromised. For more detailed information regarding its results and implementation, it is suggested to consult [35]. As the Connected Adaptive Cruise Control (CACC) strategy remains largely uninfluenced by accessory loads, such as the HVAC system, the combined benefits of integrating these two strategies are expected to be more pronounced than the individual advantages of each strategy operating in isolation. The subsequent sections elucidate the foundational framework for our analysis and delineate the series of tests conducted to comprehensively evaluate the synergistic enhancements resulting from this integration.

6.1 CACC and IETM combined Results

To ensure reliable and consistent results, a common baseline is essential to assess the effective benefits of each strategy. In this context, various simulations have been conducted with the HVAC system activated. For the baseline scenario, the air conditioning system is controlled by a Proportional-Integral (PI) controller designed to maintain the cabin temperature at a constant reference temperature. The driver follows the cycle precisely, and this configuration serves as the reference for comparison.

In these experiments, different reference temperatures, ranging from 18 °C to 27 °C, have been examined to gauge the impact on HVAC power demand. The tests were performed with an external temperature of 32 °C and solar radiation $\dot{q}_{sun} = 1000 \text{ W} / \text{m}^2$. Furthermore, the tests encompass both WLTC and the EPA cycle to assess how the cycle's aggressiveness affects the results. All the presented outcomes are projected over a distance of 160,000 km, involving multiple iterations of the driving cycle, enabling an effective quantification of battery degradation and its impact.

In contrast, State of Charge (SOC) results have been evaluated based on a single driving cycle to gauge the immediate effects of the strategies.

6.2.1 CACC results

In this section, will be presented the results of the Eco-driving strategy, taking into account the presence of the HVAC system. It is important to note that the improvements achieved will differ from those presented in the previous chapter due to the HVAC system being active.

1. SOC Benefits:

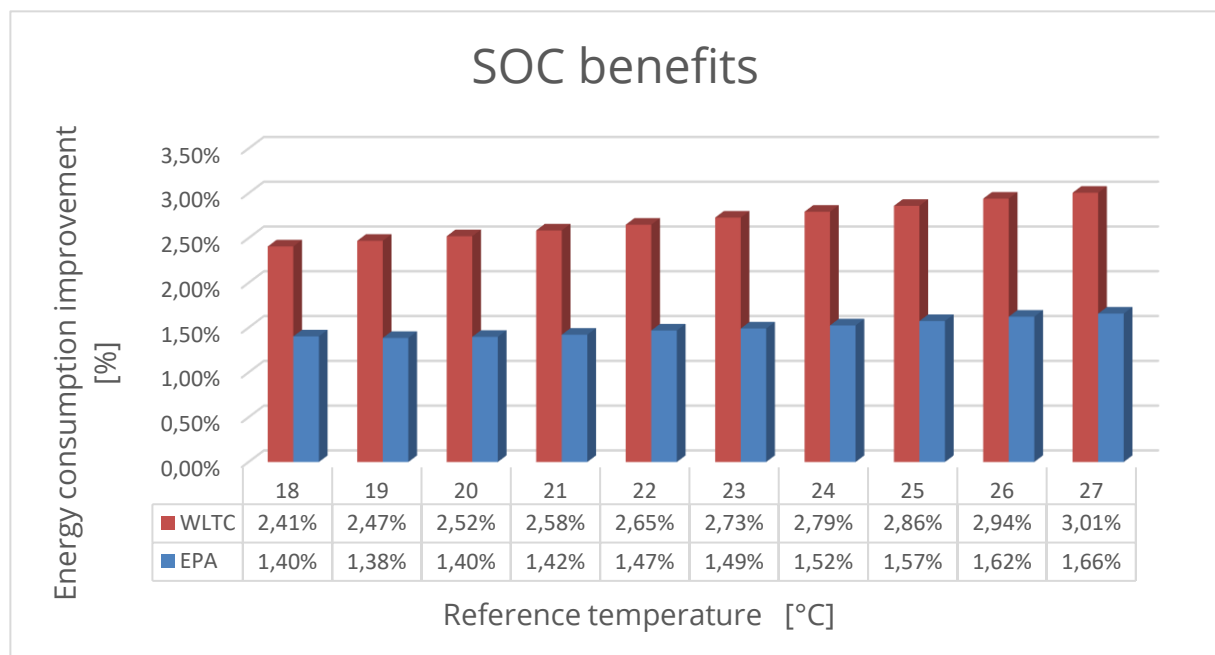


Figure 84: CACC - SOC benefits

As mentioned earlier, the values are slightly reduced in this case. This phenomenon can be attributed to the fact that the CACC strategy, which doesn't directly affect the HVAC system, offers a relatively constant improvement in ΔSOC regardless of the air conditioning settings. However, since the HVAC system contributes to a higher overall energy consumption, the percentage of improvement with the CACC strategy is somewhat smaller. For instance, when

the HVAC system works harder to maintain an internal cabin temperature of 18°C, the benefits of implementing the CACC strategy are less pronounced. Conversely, with higher reference temperatures, the benefits tend to be more substantial. Similar considerations apply to the EPA cycle, where the influence of the CACC strategy is even more modest due to the less aggressive nature of the cycle. It's worth noting that the Eco-driving strategy is entirely independent of auxiliary systems since it solely focuses on minimizing traction power. These plots are included to provide a common baseline for comparing the benefits of both strategies.

2. SOH Benefits

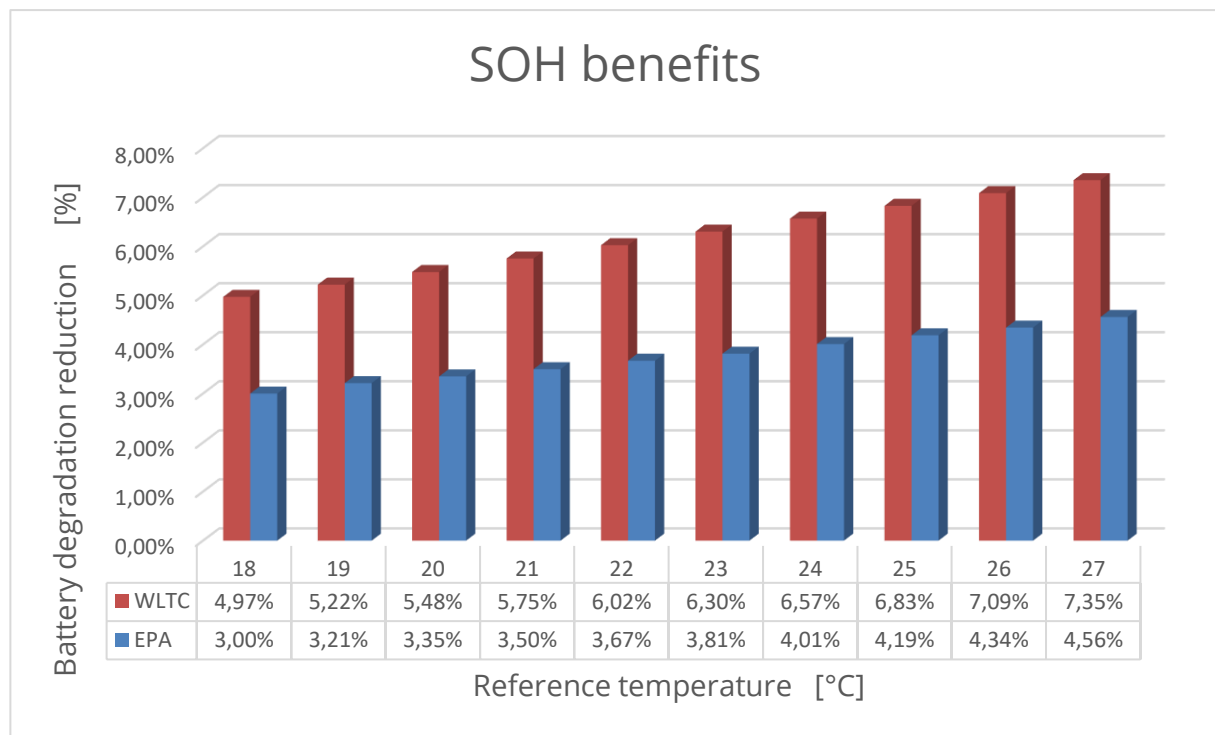


Figure 85: CACC - SOH benefits

Examining the histogram, we observe a consistent effect as described previously. The trends align with the earlier discussions, showing greater improvements in the WLTC-based cycle and a more significant benefit when the HVAC consumption is lower at higher reference temperatures. It is essential to note that even in the worst-case scenario with the most realistic and aggressive cycle, the improvement remains around 5%. This result is not negligible, especially considering that over a distance of 160,000 km, it translates to approximately 8,000 km in extended battery life.

6.2.2 Combined results

In this section the combined benefits of both strategy working together are presented. We can gain insight into the improvements achieved when these strategies collaborate. It's worth noting that these two strategies are not entirely independent. While the Eco-Driving approach remains unaffected by auxiliary systems, the IETM strategy is influenced by CACC. The IETM strategy aims to reduce HVAC power during peak traction power demand to mitigate battery degradation. Thus, having a different traction profile induced by the Eco-Driving strategy does impact the IETM results. Therefore, the combined results aren't a simple summation of the two contributions; they exhibit slight variations due to this interplay.

1. SOC Benefits

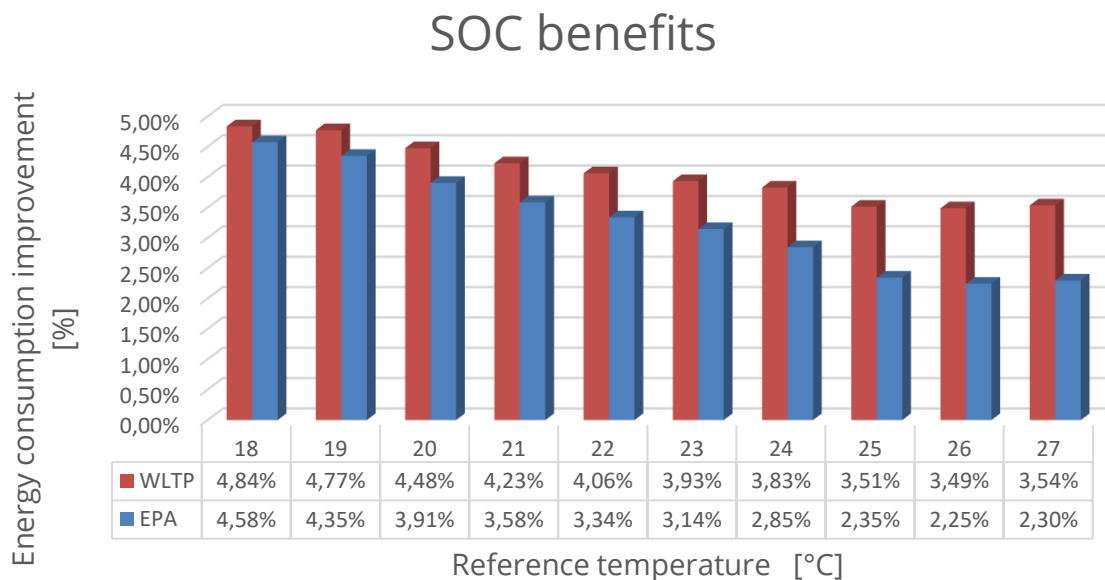


Figure 86: CACC+IETM - SOC benefits

Upon observing the combined results, we can discern that the percentage of improvement is higher for each cycle and reference temperature. However, an interesting trend emerges: the percentage of improvement decreases as the reference temperature increases, primarily influenced by the IETM strategy's effects (detailed in [35]). The IETM strategy is particularly effective at lower reference temperatures, where higher energy is used by the HVAC, resulting in larger improvements. When the temperature is higher, the improvement offered by the IETM strategy decreases, leading to a downward trend in the overall improvement.

Additionally, when considering the results related to the EPA cycle, it's noticeable that the improvements are quite close to those observed in the WLTC. This is largely attributed to the

IETM strategy, which exhibits higher benefits on the EPA cycle compared to the WLTC, particularly at lower temperatures. With a more aggressive cycle, the strategy temporarily sacrifices cabin comfort by releasing the HVAC power constraint to cope with the peak current demand for traction. However, if the cabin temperature deviates significantly from the reference, the system acts to re-converge it to the desired temperature. This effect results in increased energy consumption, especially at lower reference temperatures, where, in the absence of the HVAC, the temperature would quickly rise, necessitating more substantial power requests to return to the reference temperature. Consequently, this justifies the observed results: the CACC strategy contributes more significant improvements in the WLTC, while the IETM strategy shines on the EPA cycle. From an energy perspective, this leads to overall benefits that are comparable for both cycles.

2. SOH Benefits

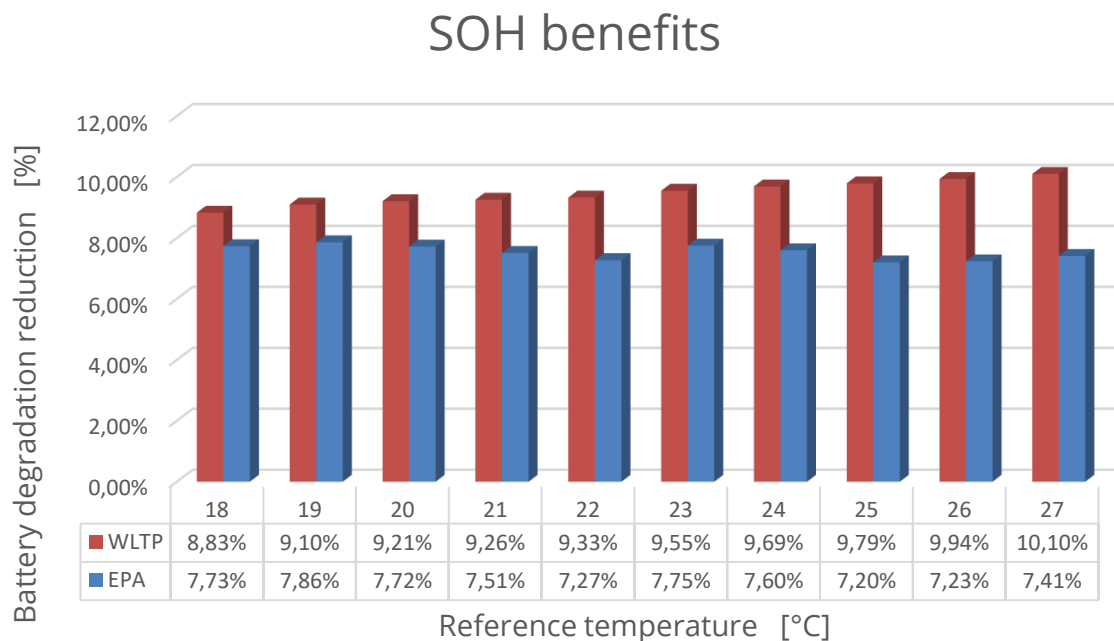


Figure 87: CACC+IETM – SOH benefits

Concerning battery SOH, the trend aligns with what was found for the CACC single strategy. In this context, the HVAC system provides higher benefits when the reference temperature is lower since it reduces auxiliary power requests (most significant at an 18°C reference temperature) during high current draws for traction. As a result, higher benefits are achieved at lower temperatures. Given that the battery degradation benefits are more pronounced for the CACC strategy, this trend carries through in this aspect as well.

7. Future work

The implemented architecture provides a solid baseline for the development of more sophisticated strategies. Several interesting avenues for future work emerge from this foundational research.

First and foremost, enhancing the strategy's awareness of the vehicle's surroundings presents a promising direction. This could involve integrating more complex information obtained from communication between vehicles. For instance, leveraging data from the vehicle's navigation system could provide critical insights into road conditions, such as slope, traffic congestion, and road geometry. These additional details could enable more precise optimization. Furthermore, such data could empower the system to receive comprehensive information about the leading vehicle, allowing it to predict future behaviour more accurately. This would be particularly valuable as it would eliminate the assumption of constant speed in the preceding vehicle, a notable limitation in the current strategy.

Expanding the control architecture to accommodate non constant control variables is another avenue of exploration. While this possibility has been explored in the project, the computational demands were prohibitively high for real-time implementation. The requirement for N^2 iterations, where N represents the number of acceleration options considered for a single constant control action, posed challenges. One potential solution to this issue could be to explore the application of reinforcement learning techniques. By leveraging reinforcement learning, it could be possible to identify optimal control actions leading to minimum costs in subsequent steps, starting from a specific state.

As last point, to validate the real-time feasibility of the implemented strategy, hardware-in-the-loop (HIL) testing should be considered as a future step. HIL testing would involve real-time hardware testing to verify the strategy's performance under real-world conditions. While this was not conducted during the thesis due to time limitations, it stands as a valuable opportunity for further verification and validation of the model.

8. Conclusion

In conclusion, this research has been dedicated to the development and implementation of a novel optimization strategy based on Model Predictive Control (MPC) for battery electric vehicles (BEVs). It's important to note that the secondary strategy, Integrated Energy and Thermal Management (IETM), which focuses on optimizing HVAC power commands to regulate cabin thermal conditions, was not the primary focus of this thesis and was not developed by the author.

Crucially, the combination of these two strategies offers the potential for greater benefits than either strategy in isolation. By merging the precision of the Eco-Driving approach with the HVAC optimization capabilities of the IETM strategy, a comprehensive solution emerges. This dual approach has the potential to significantly extend the range of BEVs, mitigate range anxiety, and substantially enhance battery longevity. This, in turn, contributes to the long-term sustainability and economic viability of these eco-friendly vehicles.

Additionally, this research underscores the importance of practicality in these strategies. By developing simplified models that retain the essential characteristics of the complex Simscape™ model, computational costs are dramatically reduced, making the strategies suitable for real-time implementation. The robustness of the model, capable of withstanding noise and delay, and achieving reasonable results for various driving cycles, is a testament to its practicality and real-world adaptability. Importantly, no hardware updates or modifications are necessary for implementing these strategies, as only software updates are required. This practicality is vital for the widespread adoption and application of these strategies in real-world scenarios.

In summary, this work contributes to the ever-evolving field of sustainable transportation. As electric vehicles continue to gain prominence in the automotive landscape, strategies like these could be fundamental. They have the potential to advance the adoption of BEVs by alleviating range anxiety, reducing energy consumption, and promoting the longevity of costly battery systems. This research lays the foundation for a more sustainable and environmentally conscious future of mobility, where BEVs are not just a viable choice but a compelling one, offering a cleaner and more sustainable mode of transportation for the generations to come.

References

- [1] International Council on Clean Transportation. (2020). A strategy to decarbonize the global transport sector by mid-century (Report).
- [2] NASA. (n.d.). What is the greenhouse effect? Climate Change: Vital Signs of the Planet. <https://climate.nasa.gov/faq/19/what-is-the-greenhouse-effect/>
- [3] International Energy Agency. (2016). World Energy Outlook 2016: Special Report on Energy and Air Pollution.
- [4] ACEEE International Symposium on Energy Efficiency Washington DC, June 26, 2018. 'Vehicle Fuel Economy Standards and Feebate System'
- [5] International Energy Agency. (2020). World Energy Outlook, 2020.
- [6] Accardo, A., Dotelli, G., Musa, M., & Spessa, E. (2021). Life Cycle Assessment of an NMC Battery for Application to Electric Light-Duty Commercial Vehicles and Comparison with a Sodium-Nickel Chloride Battery. *Applied Sciences*, MDPI.
- [7] Briec, E., Mazal, C., Meyer, G., Müller, B., & Stakeholders of the European Technology Platforms ERTRAC, EPoSS, and SmartGrids. (2012). *European Roadmap: Electrification of Road Transport* (2nd ed.). Technical Report. Capire and ICT4FEV.
- [8] Spessa, E. (2023). Energy Management in Hybrid and electric Vehicles, Politecnico di Torino
- [9] Regulation of the European Parliament and of the Council concerning batteries and waste batteries, amending Directive 2008/98/EC and Regulation (EU) 2019/1020 and repealing Directive 2006/66/EC, Brussels, 28 June 2023
- [10] International Council on Clean Transportation. (2023). Annual update on the global transition to electric vehicles: 2022
- [11] Ricardo Energy & Environment. (2016). Improving understanding of technology and costs for CO₂ reductions from cars and LCVs in the period to 2030 and development of cost curves. Report for DG Climate Action Ref. CLIMA.C.2/FRA/2012/0006. 25 February 2016.
- [12] Sinovoltaics. (2019, September 12). Energy Density and Specific Energy of Battery. Sinovoltaics Learning Center. <https://sinovoltaics.com/learning-center/storage/energy-density-and-specific-energy-of-battery/>
- [13] IEA. (2023). Public charging point per battery-electric LDV ratio in selected countries against battery electric LDV stock share, 2015-2022. IEA. <https://www.iea.org/data-and-statistics/charts/public-charging-point-per-battery-electric-ldv-ratio-in-selected-countries-against-battery-electric-ldv-stock-share-2015-2022>

- [14] Koroma, M. S., Costa, D., Philippot, M., Cardellini, G., Hosen, M. S., Coosemans, T., & Messagie, M. (2022). Life cycle assessment of battery electric vehicles: Implications of future electricity mix and different battery end-of-life management. Elsevier.
- [15] Anselma, P. G., Kollmeyer, P., Lempert, J., Zhao, Z., Belingardi, G., & Emadi, A. (2021, January 10). Battery state-of-health sensitive energy management of hybrid electric vehicles: Lifetime prediction and ageing experimental validation. Elsevier.
- [16] Ungurean, L., Cârstoiu, G., Micea, M. V., & Groza, V. (2017). Battery state of health estimation: A structured review of models, methods and commercial devices. *International Journal of Energy Research*, 41, 151–181. DOI: 10.1002/er.3598.
- [17] Chevrolet,(2016). Charging time specifications. [Product Information]. <https://media.chevrolet.com/media/us/en/chevrolet/vehicles/spark-ev/2016.html#:~:text=Plug%20in%20the%20cord%20into,to%20less%20than%20seven%20hours>.
- [18] Huang, S.-C., Tseng, K.-H., Liang, J.-W., Chang, C.-L., & Pecht, M. G. (2017). An Online SOC and SOH Estimation Model for Lithium-Ion Batteries. *Energies*, 10(4), 495. <https://doi.org/10.3390/en10040495>
- [19] SAE International. (2023). SAE Levels of Driving Automation™ Refined for Clarity and International Audience. Retrieved from <https://www.sae.org/blog/sae-j3016-update>
- [20] Ouster, Inc. (2023). Ouster Lidar Sensor Comparison. Retrieved from <https://ouster.com/products/compare-lidar-sensors/>
- [21] Robert Bosch GmbH. (2014). Chassis Systems Control: Fourth generation long-range radar sensor (LRR4). Chassis Systems Control, Robert-Bosch-Allee 1, 74232 Abstatt, Germany. Retrieved from www.bosch-automotivetechology.com
- [22] Qi, X., Barth, M. J., Wu, G., Boriboonsomsin, K., & Wang, P. (2018). Energy Impact of Connected Eco-driving on Electric Vehicles. In G. Meyer & S. Beiker (Eds.), *Road Vehicle Automation 4*, Lecture Notes in Mobility, DOI: 10.1007/978-3-319-60934-8_10. Springer International Publishing AG.
- [23] Albertengo, G. (2022-2023). Presentazione nel corso del corso di laurea in Communication & Network Systems, Politecnico di Torino, Dipartimento di Elettronica e Telecomunicazioni - DET.
- [24] Shen, M., Dollar, R. A., Molnar, T. G., He, C. R., Vahidi, A., & Orosz, G. (2022, October 10). Energy-efficient Reactive and Predictive Connected Cruise Control.
- [25] Wang, J., & Rajamani, R. (2004). Should Adaptive Cruise-Control Systems be Designed to Maintain a Constant Time Gap Between Vehicles? *IEEE Transactions on Vehicular Technology*, 53(5).
- [26] Verschelde, J. (2022, September 7). Golden Section Search Method [Slides]. Lecture 7 in Numerical Analysis (MCS 471). University of Illinois at Chicago.

- [27] Ma, H., Chu, L., Guo, J., Wang, J., & Guo, C. (2020). Cooperative Adaptive Cruise Control Strategy Optimization for Electric Vehicles Based on SA-PSO With Model Predictive Control. *IEEE Access*. DOI: 10.1109/ACCESS.2020.3043370
- [28] Ookla. (2023, August). Speedtest Global Index - United States - Mobile. Speedtest by Ookla. <https://www.speedtest.net/global-index#mobile>
- [29] Al-Wreikat, Y., Serrano, C., & Sodr , J. R. (2021). Effects of ambient temperature and trip characteristics on the energy consumption of an electric vehicle. *Elsevier*.
- [30] Vemuri, A. T., & Stauder, K. (2020, September). How to Design Heating and Cooling Systems for HEV/EVs. Texas Instruments.
- [31] Rashid, Rehan Mohsin, "Thermal Management of Vehicle Interior Temperature for Improvement of Fuel Economy" (2018). Electronic Theses and Dissertations. 7564. <https://scholar.uwindsor.ca/etd/7564>
- [32] Afrasiabian, E., Douglas, R., & Best, R. (2021). Dynamic Modelling and Performance Prediction of a Multi-unit Baseline Air Conditioning System for a Generic Bus under Part-Load Conditions. *SAE International Journal of Commercial Vehicles*, 14(2), [02-14-02-0015]. <https://doi.org/10.4271/02-14-02-0015>
- [33] He, H., Jia, H., Sun, C., & Sun, F. (2018). Stochastic Model Predictive Control of Air Conditioning System for Electric Vehicles: Sensitivity Study, Comparison, and Improvement. *IEEE Transactions on Industrial Informatics*
- [34] Schaut, S., & Sawodny, O. (2020). Thermal Management for the Cabin of a Battery Electric Vehicle Considering Passengers' Comfort. *IEEE Transactions on Control Systems Technology*, 28(4).
- [35] Mauro, M. (2023). Battery fading aware cabin thermal management strategy for extending battery life in battery electric vehicles. Politecnico di Torino.
- [36] Bertoni, L., Guanetti, J., Basso, M., Masoero, M., Cetinkunt, S., & Borrelli, F. (2017). An adaptive cruise control for connected energy-saving electric vehicles. *IFAC Proceedings Volumes*, 50(1), 16495-16500. DOI: 10.1016/j.ifacol.2017.08.425
- [37] Wang, J., Zheng, Y., Dong, J., Chen, C., Cai, M., Li, K., & Xu, Q. (2022). Implementation and Experimental Validation of Data-Driven Predictive Control for Dissipating Stop-and-Go Waves in Mixed Traffic. Published on November 23, 2022.
- [38] Lee, H., Kim, K., Kim, N., & Cha, S. W. (2022). Energy efficient speed planning of electric vehicles for car-following scenario using model-based reinforcement learning. Published on March 15, 2022.
- [39] Michel, P., Karbowski, D., and Rousseau, A., "Impact of Connectivity and Automation on Vehicle Energy Use," SAE Technical Paper 2016-01-0152, 2016, <https://doi.org/10.4271/2016-01-0152>.

- [40] Bassel Othman, Giovanni de Nunzio, Antonio Sciarretta, Domenico Di Domenico, Carlos Canudas de Wit. Connectivity and Automation as Enablers for Energy-Efficient Driving and Road Traffic Management. Lackner M., Sajjadi B., Chen WY. (eds). Handbook of Climate Change Mitigation and Adaptation, Springer, pp.XXVII, 2130, 2021, 978-1-4614-6431-0. [ff10.1007/978-1-4614-6431-0_128](https://doi.org/10.1007/978-1-4614-6431-0_128)-1ff. [ffhal-03161894f](https://doi.org/10.1007/978-1-4614-6431-0_128)
- [41] Tulga Ersal, Ilya Kolmanovsky, Neda Masoud, Necmiye Ozay, Jeffrey Scruggs, Ram Vasudevan & Gábor Orosz (2020) Connected and automated road vehicles: state of the art and future challenges, *Vehicle System Dynamics*, 58:5, 672-704, DOI: 10.1080/00423114.2020.1741652
- [42] Sinha, Neelu. "Emerging Technology Trends in Vehicle-to-Everything Connectivity." 2019 Wireless Telecommunications Symposium (WTS). IEEE, 2019. 1–12. Web.
- [43] A. Abraham, S. C. Nagavarapu, S. Prasad, P. Vyas and L. K. Mathew, "Recent Trends in Autonomous Vehicle Validation Ensuring Road Safety with Emphasis on Learning Algorithms," *2022 17th International Conference on Control, Automation, Robotics and Vision (ICARCV)*, Singapore, Singapore, 2022, pp. 397-404, doi: 10.1109/ICARCV57592.2022.10004304.
- [44] Junmin Wang and R. Rajamani, "Should adaptive cruise-control systems be designed to maintain a constant time gap between vehicles?," in *IEEE Transactions on Vehicular Technology*, vol. 53, no. 5, pp. 1480-1490, Sept. 2004, doi: 10.1109/TVT.2004.832386.
- [45] M. Hattori and H. Fujimoto, "Basic Idea of Quadrant Dynamic Programming for Adaptive Cruise Control to Create Energy Efficient Velocity Trajectory of Electric Vehicle," *2020 IEEE 16th International Workshop on Advanced Motion Control (AMC)*, Kristiansand, Norway, 2020, pp. 29-33, doi: 10.1109/AMC44022.2020.9244328.
- [46] Y. Gao, Z. Wang, C. Fang, C. Luo and S. You, "Optimal Connected Cruise Control Design with Stochastic Communication Delays," *2019 International Conference on Internet of Things (iThings) and IEEE Green Computing and Communications (GreenCom) and IEEE Cyber, Physical and Social Computing (CPSCom) and IEEE Smart Data (SmartData)*, Atlanta, GA, USA, 2019, pp. 756-760, doi: 10.1109/iThings/GreenCom/CPSCom/SmartData.2019.00140.
- [47] Pan, C., Zhang, C., Wang, J., & Liu, Q. (2023). Adaptive Cruise Control Strategy for Electric Vehicles Considering Battery Degradation Characteristics. *Applied Sciences*, 13(7), 4553. <https://doi.org/10.3390/app13074553>